Title
Drift Diffusion Modeling of Morphological Effects in Organic Photovoltaic Devices

Author
Finck, Benjamin Yuji

Publication Date
2016

Peer reviewed|Thesis/dissertation

University of California
Los Angeles

Drift Diffusion Modeling of Morphological Effects in Organic Photovoltaic Devices

A dissertation submitted in partial satisfaction
of the requirements for the degree
Doctor of Philosophy in Chemistry

by

Benjamin Yuji Finck

2016

Abstract of the Dissertation

Drift Diffusion Modeling of Morphological Effects in Organic Photovoltaic Devices

by

Benjamin Yuji Finck

Doctor of Philosophy in Chemistry

University of California, Los Angeles, 2016

Professor Benjamin Joel Schwartz, Chair

As humanity's energy consumption continues to increase for the coming decades, with our knowledge of traditional fossil fuels' deleterious effects on our planetary ecosystem, it is evident that development of clean, economical, and renewable energy sources is one of the great remaining problems faced by our species. Photovoltaic technologies, particularly those based on organic materials, have been suggested as potentially viable solutions to our energy demands. However, several deficiencies of organic photovoltaic devices, specifically their relatively low power conversion efficiency, has hampered their adoption for large-scale energy production. One of the main causes of these deficiencies is the imprecise control of the distribution of the active materials within these photovoltaic devices. This dissertation presents a series of semiconductor device modeling simulations, which were conducted to elucidate the various effects of the morphology of active components on organic photovoltaic devices' charge transport properties and photovoltaic performance. Our simulations illustrate how subtle variations in the active layer morphology can both hinder and benefit device performance in surprising ways. This indicates the need for novel processing techniques, which allow precise control of device morphology, in order for organic photovoltaic devices to be competitive with other contemporary renewable energy technologies.

The dissertation of Benjamin Yuji Finck is approved.

Anastassia N. Alexandrova

Russel E. Caflisch

Benjamin Joel Schwartz, Committee Chair

University of California, Los Angeles

2016

This work is dedicated to my beloved family: to my parents, Sanford and Stella Finck, and to my siblings, Seth, Rachel, and Aaron Finck. I would be nothing without your love and support.

Table of Contents

1 Introduction **1**

1.1 Organic Photovoltaics as a Renewable Energy Technology 1

1.2 Basic Construction and Operating Principles of Organic Photovoltaics 2

1.3 Evaluating Organic Photovoltaic Device Performance: J–V Characteristics . 4

1.4 Modeling Charge Transport in Organic Photovoltaics: Drift-Diffusion Modeling Overview 6

1.5 Case studies of morphological effects in OPV charge transport 8

2 Understanding the Origin of the S–curve in Conjugated Polymer/Fullerene Photovoltaics from Drift-Diffusion Simulations **13**

3 Drift-Diffusion Modeling of the Effects of Structural Disorder and Carrier Mobility on the Performance of Organic Photovoltaic Devices **20**

3.1 Introduction 20

3.2 Computational Methods 23

3.2.1 Drift Diffusion Model 23

3.2.2 Disordered Mobility profiles and Ensembles 26

3.3 Results and Discussion 30

3.3.1 The Effects of the Range of Disordered Mobilities on Ensemble-Averaged Device Behavior 31

3.3.2 The Effects of the Spatial Disorder Length Scale on OPV Device Performance 39

3.3.3 The Effects of Spatial Disorder on the Shape of J–V Curve 41

3.4 Conclusions 42

4 Do Organic Photovoltaics Really Need a Mixed Phase? Drift-Diffusion Studies of the Effect of Bulk Heterojunction Compositional Morpholog on Optimum Device Performance 44

4.1 Introduction 44

4.2 Computational Methods 48

4.2.1 Drift Diffusion Model 48

4.2.2 Mapping Morphologies to a D-D OPV Device Model 50

4.3 Results and Discussion 56

4.3.1 Cahn-Hilliard Generated Morphologies 56

4.3.2 Empirical (HAADF-STEM) Morphology 59

4.3.3 Charge Densities and Recombination Rates 61

4.3.4 Conducting Pathways 63

4.3.5 Effects of mixed-phase on Device Performance 66

4.4 Conclusions 70

5 Theory of Current Transients in Planar Semiconductor Devices: Insights and Applications to Organic Solar Cells 72

5.1 Introduction 72

5.2 Derivation of a General Current-Density Equation for 1-D Planar Semiconductor Diodes 74

5.2.1 Contributions to the Total Measured Current 74

5.2.2 Mobile-Carrier Currents 75

5.2.3 The Displacement Current 76

5.2.4 The Total Measured Current 77

5.2.5 The Surface Recombination Current, J_{surf} 80

5.2.6 Areal Charge Densities on the Contacts 81

5.2.7 Integrating the Total Measured Current 82

5.3 Analytical Applications of the Model: Implications for Materials Characterization 85

5.3.1 The Time-of-Flight Experiment 85

5.3.2 Determination of the Average Carrier Concentration with CELIV . . 86

5.4 Understanding the Formalism Via Time-Dependent Drift-Diffusion Modeling: CELIV Revisited 89

5.5 Conclusions 93

A Supplemental Material for: Drift-Diffusion Modeling of the Effects of Structural Disorder and Carrier Mobility on the Performance of Organic Photovoltaic Devices 94

A.1 Cahn-Hilliard Generated Morphologies 94

A.2 Mobility Profiles, Discretization, Mesh Size, and Accuracy 95

A.3 Ensemble Mobility Distributions 97

B Supplemental Material for: Do Organic Photovoltaics Really Need a Mixed Phase? Drift-Diffusion Studies of the Effect of Bulk Heterojunction Compositional Morpholog on Optimum Device Performance 100

B.1 Full J–V Characteristics of Simulated Devices 100

B.2 Spatially Resolved Simulation Results (C, n, and $J_{n,y}$ at Additional Morphological Length Scales 100

B.3 Effects Alternative Mixing Method 101

C Supplemental Material for: Theory of Current Transients in Planar Semiconductor Devices: Insights and Applications to Organic Solar Cells 106

C.1 Derivation of the Spatially Constant Total Current 106

C.2 Relating the Charge on the Contacts to the Voltage 107

C.3 Drift Diffusion Model 108
C.4 Numerical methods and Solution Details 109
C.4.1 Boundary Conditions 109
C.4.2 Generation and Recombination 110
C.4.3 Solution Scheme 110
C.4.4 Transient Simulations 111

D Methodology for Solving Semiconductor Equations 113

E Simulation Software Operation and the `DriftDiffusion` class 117

E.1 Device Instantiation and the `DriftDiffusion()` Constructor 118
E.2 Performing 2-D Simulations and Mapping Morphological Data with `ImportMorphology()` 119
E.3 The `DDSolve()` function 119
E.4 Simulation Functions 120
E.4.1 `JVCharacteristic(double Va_start, double Va_end, int printInterval=0)` 120
E.4.2 `PhotoCELIV(double A, double pulseStrength, int tdelay)` . . . 121
E.4.3 `TransientPhotocurrent(double pulseStrength, int durationLightPulse, int durationTransient)` 122
E.5 Methods for Device Parameter Manipulation 122
E.5.1 Applying a Voltage Bias with `SetVoltage(double Vapp)` and `RampVoltage(double dVa)` 123
E.5.2 Changing the Charge Carrier Mobilities with `SetElectronMobility()` and `SetHoleMobility()` 123

E.5.3 Specifying the Charge Carrier Mobilities of Acceptor and Donor materials with `SetMuNMaxMin()` and `SetMuPMaxMin()` 124

E.5.4 Changing the Generation Rate, G, with `SetGeneration()` and `SetGeff()` 124

E.5.5 Specifying Recombination Mechanism and Recombination Parameters 125

E.6 Saving Simulation Data with Print Statements 125

E.7 An Example Simulation Setup 126

References **129**

List of Figures

1.1 An example J–V characteristic illustrating the crucial figures of merit for OPV device performance. Note that in the absence of light, the solar cell behaves essentially as a diode. 5

2.1 Simulated J-V curves analyzed in this study. The electron and hole mobilities are initially equalized to 1×10^{-4} cm^2 V^{-1} s^{-1}. The electron mobility is subsequently reduced by several orders of magnitude in two manners: (a) by decreasing the electron mobility throughout the device and (b) by only decreasing the mobility only near the cathode through the use of a sigmoid profile. Fig. 2.1(a) illustrates the inability of mismatched carrier mobilities to induce an S–curve; Fig. 2.1(b) illustrates that a sigmoid-shaped electron mobility profile is capable of inducing an S–curve. The effects of the different features of the mobility profile are explored by increasing the size (c) and abruptness (d) of the mobility drop-off, as illustrated in the insets over an expanded spatial region of the 100-nm thick device active layer. Increasing the region of reduced mobility and the abruptness of the drop in mobility results in a more pronounced S–curve character. 17

2.2 Individual charge carrier currents for S–curve (solid symbols, device parameters given in Table 2.1 and normal OPV (open symbols, no mobility drop-off) devices. The normal device shows typical J–V diodic behavior for the individual carriers, but the device with the mobility drop-off has a severely distorted J–V character, particularly for the electron current (blue curves). 18

2.3 Spatially discretized electron current (J_n) and hole current (J_n) at various applied voltages for both an S–curve device (solid symbols, parameters given in Table 2.1) and a normal BHJ device (open symbols, no mobility drop-off). The currents are shown at applied voltages corresponding to (a) short circuit conditions, (b) near the inflection point of the J–V curve, and (c) beyond V_{OC}. In panel (b), there is severe distortion of the individual carrier currents for the S-curve device, which results in a reduced total current and an inversion of the current gradients, resulting in a buildup of charge. At higher biases, the severity of this inversion is reduced, and normal behavior is re-established. 19

3.1 (a) An example mobility profile of a device replica generated by randomly sampling a mobility ensemble characterized by the parameters $\mu_0 = -8.0$, $\sigma = 0.7$, $\delta = 3$ nm. (b) An example mobility profile of a device replica generated by sampling from a Cahn-Hilliard morphology, with $\mu_{\mathrm{CH}} = -8.0$, $\sigma_{\mathrm{CH}} = 1.0$, and average $\delta_{\mathrm{CH}} \approx 3.3$ nm (C-H $\epsilon = 1.6 \times 10^{-5}$). 27

3.2 (a) A collection of J–V characteristics for an ensemble of replicas randomly generated via the random mobility distribution method using the ensemble parameters $\mu_0 = -8.0$, $\sigma = 0.7$, and $\delta = 3$ nm. (b) A collection of J–V characteristics for an ensemble of replicas sampled from Cahn-Hilliard Morphologies with $\mu_{\mathrm{CH}} = -8.0$, $\sigma_{\mathrm{CH}} = 1.0$, and average $\delta_{\mathrm{CH}} \approx 3.3$ nm (c) The ensemble averaged J–V characteristics for both methods (red-dashed curve for random mobility profiles; blue dotted curve for C-H generated profiles). For comparison, the solid black curve shows J–V characteristic of a non-disordered, 'pristine' device with ($\mu_n = \mu_p = 10^{-4}$ cm^2 V^{-1} s^{-1} throughout the active layer). 32

3.3 Ensemble-averaged J–V characteristics for several series of replica devices. Each curve is the average of 1000 replicas. (a) Mobility profiles generated from the random distribution method with μ_0 = -8.0 and δ = 3 nm but different values of the degree of disorder parameter, σ, which ranges from 0.1 to 1.9 in steps of 0.2. (b) Mobility profiles generated from C-H morphologies with $\epsilon = 1.6 \times 10^{-5}$ and thus $\delta_{\mathrm{CH}} \approx 3.3$ nm but different values of σ_{CH} ranging from 0.1 to 3.0 as indicated. 34

3.4 Relevant figures of merit of ensemble-averaged J–V characteristics for the series of replicas presented in Fig. 3 as a fraction of a pristine device's taken as (a) the disorder parameter for the random mobility distribution method, σ, is increased from 0.1 to 2.0, and (b) the disorder parameter σ_{CH} for the Cahn-Hillard morphology method is varied from 0.1 to 3.0. 34

3.5 Histograms illustrating the distribution of: (a) the short-circuit current, (b) the fill factor, (c) the power conversion efficiency, and (d) the open circuit voltage for individual device replicas sampled from the randomly-generated spatial mobility distribution ensemble of Fig. 3.1a ($\mu_0 = -8.0$, $\sigma = 0.7$, $\delta =$ 3 nm); see Appendix A for the corresponding plots for spatially-disordered mobility replicas generated by the C-H method. 36

3.6 Skewness of device replicas' figures of merit as a function of the disorder parameter, σ (same randomly-generated mobility replicas whose individual properties and ensemble-averaged behavior are summarized in Figs. 3.2 through 3.5). 37

3.7 Relevant figures of merit for the ensemble averaged J–V characteristics presented in Fig. 3.3a as a fraction of the pristine device's but as the spatial feature size, δ, in the randomly generated profile ensemble is increased from 2 to 15 nm. 40

3.8 J–V curves comparing a randomly-generated structurally-disordered ensemble (blue triangles) with an ensemble of structurally pristine devices with only mobility disorder (red circles; see text for details). Note that although both ensembles' performance diminishes as a result of the inclusion of disorder, the inclusion of structural disorder leads to a much more severe drop in performance. 41

4.1 An example of a spatially dependent generation rate for a morphology generated by Cahn-Hilliard modeling. By comparison of this image with the morphology images presented in Fig. 4.2, it is clear that charges carriers are only generated in proximity to the interface between donor and acceptor phases. 57

4.2 Simulation results of OPV devices based on C-H morphologies with a controllably increasing amount of intermixed compositional regions from left (no intermixing) to right (most intermixing). All figures represent the device at short-circuit conditions under simulated AM1.5 illumination. Panels (a)-(c): overall compositional morphology; panels (d)-(f): spatially-dependent electron density; panels (g)-(i): spatially-dependent recombination rate; panels (j)-(l): electron current density profile. Each of these image plots shows a 100 nm × 100 nm subsection of the entire simulated device. The ITO/PEDOT:PSS anode and the calcium cathode are located at the top and bottom of each plot, respectively. The three columns correspond to devices with 0%, 30%, and 70% of the active area characterized as mixed-phase, respectively. . 60

4.3 Image plots of simulation data for an experimentally-determined (by HAADF-STEM) BHJ morphology.[186] Panels (a)-(d) present the compositional morphology, steady-state electron density, steady-state recombination rate and the y-component (vertical component) of the electron current density vector, respectively, all presented under short-circuit conditions (i.e., 0 V applied bias). The images show the data for a 100 nm × 200 nm subsection of the full morphology. 62

4.4 Average electron density of the five different Cahn-Hillard BHJ morphologies at varying degrees of mixing. Although most morphology length scales exhibit a drop and subsequent in electron density, the 4-nm device only exhibits a rise in electron density as its conduction pathways are constricted. 64

4.5 Change in power conversion efficiency of five Cahn-Hilliard generated BHJ morphologies with different intrinsic separation length scales studied as a function of the degree of mixing of the two pure phases. 67

4.6 Change in the short-circuit current of five Cahn-Hilliard generated BHJ morphologies with different intrinsic separation length scales studied as a function of the degree of mixing of the two pure phases. 68

4.7 Percent change in the fill-factor of five Cahn-Hilliard generated BHJ morphologies with different intrinsic separation length scales studied as a function of the degree of mixing of the two pure phases. 69

4.8 Percent change in the open-circuit voltages of five Cahn-Hilliard generated BHJ morphologies with different intrinsic separation length scales studied as a function of the degree of mixing of the two pure phases. 70

5.1 A schematic band diagram illustrating the device model used in this derivation in forward (positive) bias. The semiconductor (photoactive) layer is sandwiched between metal contacts at $x = 0$ and $x = d$. The i and s scripts on the J_n (electron current) and J_p (hole current) arrows stand for injection and sweep out, respectively. The average carrier densities are $\bar{n}$ for electrons and $\bar{p}$ for holes. The generation and recombination rates of electron-hole pairs, G and R, are distinct from the rates of freeing and trapping carriers from traps, $G_{e,h}^{D,A}$ and $R_{e,h}^{D,A}$. J_{surf} takes into account the 'surface' current that does not effectively make a transition though the semiconductor energy gap. Note that only the relative heights of the anode/cathode depictions are meant to be part of the implicit energy scale. 78

5.2 a.) Schematic representation of the CELIV model device under consideration. A uniform block of free charge with local density n and average density $n(1 - w/d)$ is swept out under a linearly changing reverse bias pulse (inset of b.)). Here w denotes the steady-state initial depletion width. b.) An Example CELIV current transient showing the typical portion of the curve that is integrated to yield the initial uniform free-carrier density (n). Non-intuitively, the shaded region is at most proportional to half of the initial average free-charge density and even further reduced if w is non-zero. 88

5.3 The various current contributions from Eq. (5.13) determined from numerical simulations and the negative of their sum, $-J_{\text{tot}}$ (upside down open triangles). Note that here the reverse bias extraction current is plotted as positive. The simulated CELIV ramp conditions are 0.1 V/μs starting at an initial forward bias of 0.6 V. The total current density from the simulation is also shown (solid blue line). The simulated total current density and the summed current density from Eq. (5.13) lie on top of each other, showing their precise quantitative agreement. We note that trapping was not included in the numerical model and thus was assumed to be zero. 91

A.1 An example of a morphology generated by solving the Cahn-Hilliard equation on a 100x500 nm grid. 95

A.2 Relevant figures of merit for the ensemble averaged J–V characteristics as a fraction of the pristine device's but as the average feature size, δ_{CH}, of the sampled Cahn-Hilliard morphologies is increased from approximately 3 to 15 nm. 96

A.3 Histograms showing the distribution of replicas from an ensemble of devices generated via Cahn-Hilliard sampling with $\mu_{CH} = -8.0$, $\sigma_{CH} = 2.0$, and $\delta_{CH} \approx 3.3$ nm 96

A.4 The effects of finer mesh point spacing on the accuracy of the ensemble average device figures of merit are illustrated. It is assumed that the smallest mesh spacing ($\Delta x = 0.05$ nm) is the most accurate. The discrepancy between the performance of coarser meshes ($\Delta x > 0.05$ nm) is plotted as a function of mesh size. This ensemble was characterized by $\mu_{\mathrm{RS}} = -8.0$, $\sigma_{\mathrm{RS}} = 0.7$, and $\delta_{\mathrm{RS}} = 3$ nm. 98

A.5 (a) Histogram depicting the distribution of mobilities from an ensemble of devices sampled from a mobility distribution characterized by $\mu_0 = -8.0$, $\sigma = 0.7$, and $\delta = 3$ nm. (b) Histogram depicting the distribution of mobilities from an ensemble of devices generated by taking 1D cross-sections of Cahn-Hilliard morphologies with average feature size $\delta \approx 3.3$ nm, with mobilities centered around $\mu_0 = -8.0$ and ranging by $\sigma = 2.0$ orders of magnitude about that mean. 99

B.1 Full J–V characteristics of the all of the initial, non-mixed morphologies studied in the main text. The first 5 curves refer to morphologies generated by Cahn-Hilliard modeling of binary fluid separation while the last curve is from an empirical morphology determined by high-angle annular dark-field scanning transmission electron microscopy (HAADF-STEM). 101

B.2 Simulation results of OPV devices based on C-H morphology (average feature size of $\sim$ 4 nm) with a controllably increasing amount of intermixed compositional regions from left (no intermixing) to right (most intermixing). All figures represent the device at short-circuit conditions under simulated AM1.5 illumination. Panels (a)-(c): overall compositional morphology; panels (d)-(f): spatially-dependent electron density; panels (g)-(i): electron current density profile. Each of these image plots shows a 100 nm $\times$ 100 nm subsection of the entire simulated device. The ITO/PEDOT:PSS anode and the calcium cathode are located at the top and bottom of each plot, respectively. 102

B.3 Simulation results of OPV devices based on C-H morphology (average feature size of $\sim$ 15 nm) with a controllably increasing amount of intermixed compositional regions from left (no intermixing) to right (most intermixing). All figures represent the device at short-circuit conditions under simulated AM1.5 illumination. Panels (a)-(c): overall compositional morphology; panels (d)-(f): spatially-dependent electron density; panels (g)-(i): electron current density profile. Each of these image plots shows a 100 nm $\times$ 100 nm subsection of the entire simulated device. The ITO/PEDOT:PSS anode and the calcium cathode are located at the top and bottom of each plot, respectively. 103

B.4 This figure illustrates the effect of a mixed-phase on the device performance of our 10-nm Cahn-Hilliard morphology when using an alternate method of mixing (i.e. mapping morphology to mobility and then smoothing the mobility profiles). 105

List of Tables

2.1 The boundary conditions and parameters used for the D-D simulations presented in the figures, except where otherwise noted. 15

3.1 The boundary conditions and parameters used for the D-D simulations presented in the figures, except where otherwise noted. 30

4.1 Boundary conditions and values of other parameters used for all the D-D simulations presented in this work, except where otherwise noted in the text. 51

4.2 Boundary conditions and parameters used for the C-H binary fluid simulations, except where otherwise noted in the text. All values serve as unitless parameters for the simulations. The average domain sizes of the morphologies generated with this parameters are given in the last row of this table. 57

4.3 The initial absolute figures of merit for all of the simulated devices without a mixed-composition phase present. 65

5.1 Parameters used in the drift-diffusion photo-CELIV simulation; the values chosen are designed to roughly simulate an organic photovoltaic device . . . 92

Acknowledgments

First and foremost I would like to express my gratitude to my family, beginning with my parents, Sanford and Stella Finck, for the many years of loving support that they have provided to me. Your guidance and succor, more than anyone else's, have enabled me to reach this point in my studies. I must also thank my three older siblings, Seth, Rachel, and Aaron. As the youngest of us, I have had the benefit of learning by your excellent examples. From Seth, I learned the value of loyalty and dedication to your friends over self-interest. From Rachel, I learned the importance of fastidiousness and effective communication. From Aaron, I learned that intelligence, no matter how great, is only of value when paired with labour. To all of my family, my greatest hope is that I can provide to others the support and inspiration that you have given me.

I could not have endured through the years devoted to this work without the aide of the friends I've made at UCLA. You were there during the good times and the bad times, and I'll cherish all of those moments because we got to share them. Thank you to Jordan Aguirre for being such an amazing person and researcher and for always abiding my prattle about trivialities. To my awesome roommate Nanette Jarenwattananon, who kept me grounded and in-check when my lunacy would go little to far. To my officemate Steve Hawks, whose tenacity and fervor for science inspired me always to work harder. Thanks to my fellow theorists and comrades-in-arms Argyris Kahros, Jennifer Casey, and Godwin Kanu who were always available to celebrate when things worked and to commiserate when they didn't. I thank my advisor, Benjamin J. Schwartz. From the first time I met him, I was in awe of his passion for science and the pursuit of knowledge. Ben taught me that a crucial part of being a good scientist was finding a balance between furthering your own knowledge as well as conveying that knowledge to others. I would also like to thank Brent Corbin and Arlene Russell. Their devotion to the education of others made a lasting impression on me and reminds me that knowledge is meant to be shared with any who wish to learn it.

I would like to acknowledge my sources of funding. External funding was provided through the Molecularly Engineered Energy Materials (MEEM) group, an Energy Frontier

Research Center funded by the U.S. Department of Energy, Office of Science, Office of Basic Energy Sciences under Award No. DE-SC0001342. I also received funding the National Science Foundation under Grants No. 1112569 and No. 1510353. I would also like to thank UCLA's chemistry department for providing me with the many paid teaching assistant positions that I have held.

Finally, I would like to acknowledge the memory of Sarah Ellen Graves. You were taken from the world too early but your presence is still felt by those who loved you. Your memory has kept me motivated when things felt most hopeless. More than anyone else, I hope that I've made you proud with the work contained in this dissertation.

Vita

2005	High School Diploma, Stanton College Preparatory School, Jacksonville, Florida
2009	Bachelors of Science (Chemistry), Emory University
2009–2016	Graduate Student Researcher, Department of Chemistry and Biochemistry, UCLA, Los Angeles, California
2009–2016	Teaching Assistant, Chemistry Department, UCLA, Los Angeles, California
2014–2016	Workshop Facilitator in the PEERS Program, UCLA, Los Angeles, California
2014	Masters of Science (Chemistry), UCLA, Los Angeles, California.

Publications

Finck, B. Y.; Schwartz, B. J. Understanding the Origin of the S-curve in Conjugated Polymer/Fullerene Photovoltaics from Drift-Diffusion Simulations. *Appl. Phys. Lett.* **2013**, *103*, 053306.

Hawks, S. A.; **Finck, B. Y.**; Schwartz, B. J. Theory of Current Transients in Planar Semiconductor Devices: Insights and Applications to Organic Solar Cells. *Phys. Rev. Appl.* **2015**, *3*, 044014.

Finck, B. Y.; Schwartz, B. J. Drift-Diffusion Modeling of the Effects of Structural Disorder

and Carrier Mobility on the Performance of Organic Photovoltaic Devices. *Phys. Rev. Appl.* **2015**, *4*, 034006.

CHAPTER 1

Introduction

1.1 Organic Photovoltaics as a Renewable Energy Technology

Sustainable and affordable energy production persists as one of the great technological problems remaining for humanity to solve. Traditional energy sources, primarily fossil fuels, are unsustainable, since there is essentially a finite amount of them remaining on the planet.[2] Even if the cost of collecting and processing fossil fuels could be diminished, the fact remains that eventually we will have to shift to predominantly renewable energy sources. Many have argued that solar power is the most promising renewable energy source[176] and several technologies, specifically photovoltaics and concentrated solar power, have been developed to harness that power. However, these technologies are still too costly to justify a wholesale shift away from traditional energy sources.[1] To expedite the shift towards renewable energy technology, a new class of photovoltaic devices based on organic materials has garnered significant research effort in the preceding decades.[136, 59, 194, 66] These devices are in contrast to traditional photovoltaics which are based on inorganic semiconductors.

Organic photovoltaics (hereafter referred to as OPVs) have several advantages over their inorganic counterparts. The first and foremost advantage is their significantly reduced cost in comparison to traditional inorganic photovoltaics. The majority of OPVs utilize light-absorbing semiconductor polymers which can be synthesized in vast quantities from readily available materials.[95, 105] Furthermore, the physical properties of the materials allow for the utilization of existing plastics fabrication technology, such as roll-to-roll processing[164], doctor-blading[115], etc. Along these lines, the materials in most OPVs are flexible, which should allow for easier transport and installation of such devices. The flexibility of OPVs

also allows for the production of devices with unusual form factors, extending their applicability to consumer electronics. Despite these advantages, OPVs have not seen mass adoption over other energy technologies because of their main deficiency: significantly lower power conversion efficiency compared to traditional photovoltaics. Organic photovoltaics typically exhibit power conversion efficiencies (PCE) of less than 10%[70, 190], although some more sophisticated device architectures have been developed with PCEs of ∼12%.[192] Improving the efficiency of these devices is paramount to their successful adoption as an energy technology and extensive research effort has been expended to this end. In addition to practical research, aimed solely at raising efficiencies, much research effort has been devoted to investigating the underlying causes of OPVs' low power conversion efficiencies.

1.2 Basic Construction and Operating Principles of Organic Photovoltaics

Before further discussion of the limitations of OPVs and the research methods applied to understand them, we turn to a brief description of the construction of a typical OPV device. The principle organic component in an OPV device is a light-absorbing semiconducting polymer. For decades, the most extensively used and studied OPV polymer has been poly-3-hexylthiophene (hereafter referred to as P3HT). Polymers typically employed in OPVs, including P3HT, usually consist of long chains of conjugated hydrocarbons. The delocalized π system allows these polymers to readily absorb photons in the visible region of the electromagnetic spectrum. Many of these polymers also have charge carrier mobilities that are exceptionally high for organic materials (up to 10^{-1} cm^{-2} V^{-1} s^{-1}[160]). The polymer is sandwiched between two metal electrodes, one of which is almost invariably transparent tin-doped indium oxide (ITO), since one of the electrodes must be transparent to allow light to access the active organic layer. The difference in the two electrodes' workfunctions results in a built-in electric field, which drives current flow. However, initial attempts to construct polymer solar cells with this device architecture were mostly unsuccessful, with power conversion efficiencies well below 1%.[191] The cause of these low efficiencies lies in the nature of

how these polymers absorb light. Upon absorption of visible photons, conjugated polymers do not immediately lose electrons as free charges, but rather undergo a π to π^* transition. This means that the newly excited electron remains Coulombically bound to the positive hole left behind on the polymer. This bound electron-hole pair (also known as an exciton) has net-neutral charge and thus the generation of excitons alone does not result in electrical current.

To obtain net current flow, the excitons must be split into separate charge carriers. Therefore, the majority of OPV devices consist of a binary blend of a light-absorbing, semiconducting polymer and an electron accepting material that facilitates charge separation.[190] The electron acceptor is typically a fullerene derivative, of which the most extensively studied and used is phenyl-C_{61}-butyric acid methyl ester (hereafter referred to as PCBM). The addition of an electron acceptor to the OPV active layer significantly increases exciton dissociation rates to the point that most OPV blends typically exhibit an internal quantum efficiency (ratio of free carriers generated to incident photons) of over 90%.[133] This approach, utilizing a binary blend of organic materials, became known as a bulk heterojunction (BHJ) and saw the power conversion efficiencies of typical P3HT:PCBM devices increase to 3-6%.[146] The two organic components (polymer and fullerene) are initially solution processed together and then layered between the two metallic electrodes.

Unfortunately, although the introduction of a second conducting material significantly improves overall device performance, it also has major ramifications for the charge transport properties of the organic layer. Upon fabrication, the two components (initially intimately mixed) spontaneously phase segregate into polymer-rich and fullerene-rich domain. Since exciton dissociation occurs only when polymer and fullerene are in close proximity, excessive phase segregation results in poor photon harvesting, and thus poor device performance. Conversely, if the polymer and fullerene are too evenly dispersed (low degree of phase segregation), device performance also suffers. Organic polymers and fullerene derivatives are normally charge carrier transport selective, meaning that holes flow readily through polymer, but not fullerene, and vice-versa for electrons. If the two components are too extensively mixed, carriers have more difficulty finding a continuous pathway to their respective extrac-

tion electrode. If the carriers are unable to find a continuous pathway, or if a pathway is too tortuous to result in efficient charge transport, then the carriers are likely to recombine, resulting in loss of usable electrical current and thus poor device efficiency. As such, while the introduction of an electron acceptor can improve device efficiency by improving exciton dissociation rates, it also results in a more complicated device architecture which may not be conducive to efficient charge transport. Therefore, optimum device performance is contingent upon the formation of a bicontinuous network of donor and acceptor material. The distribution of conducting materials (i.e., the device's morphology) is thus a major complication for OPV devices' overall performance and is the focus of this dissertation.

Extensive research effort has been dedicated to both controlling and understanding the role of morphology in OPV performance. The phase segregation dynamics of the organic components are highly sensitive to multiple factors, including the identity of the organic materials, fabrication technique (spin-coating vs. dip-coating vs. blade-coating, etc.), fabrication parameters (temperature, atmosphere, etc.), and thermal annealing of the active layer.[164, 115, 193] A significant amount of research effort has been focused solely on determining which combination of these parameters results in optimum device performance. Researchers have also attempted to indirectly control active layer morphology through solvent additives and solvent annealing.[71, 101] With these efforts, maximum OPV device performance has been pushed as high as 10% for single-junction solar cells.[70]

1.3 Evaluating Organic Photovoltaic Device Performance: *J*–*V* Characteristics

There are three figures of merit which determine a solar cell's capability to convert radiant solar power into electrical power. These figures of merit are determined by the device's current density vs. voltage (J–V) characteristic under illumination. A device's J–V characteristic is measured by recording the electrical current which flows through the device at different applied voltage biases. A typical J–V characteristic is presented in Fig. 1.1. The J–V characteristic appears approximately as a diode. There are several crucial points along

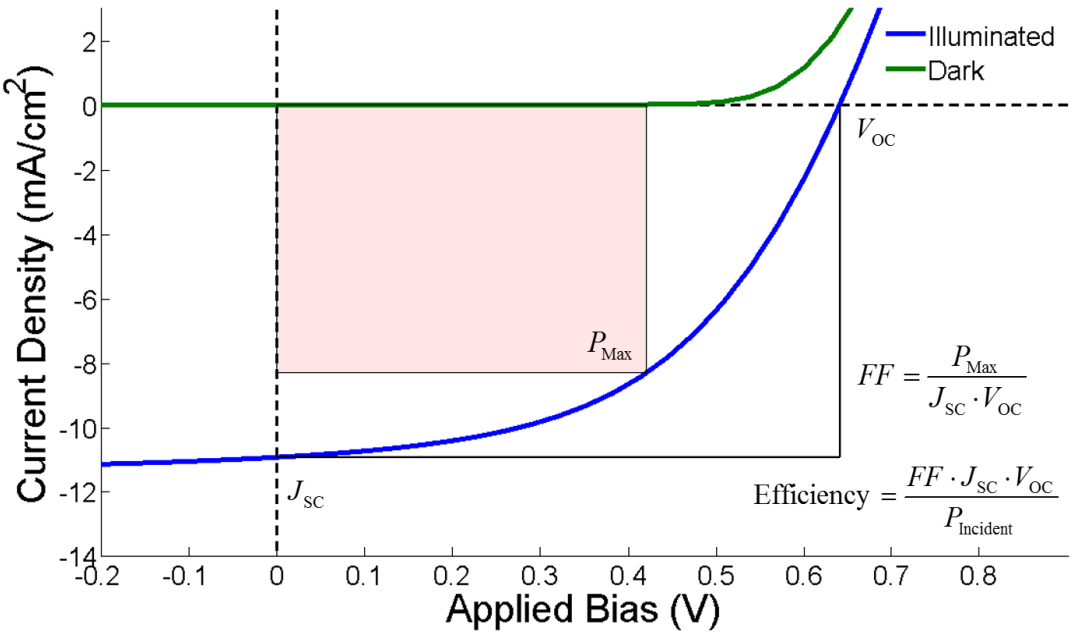

Figure 1.1: An example J–V characteristic illustrating the crucial figures of merit for OPV device performance. Note that in the absence of light, the solar cell behaves essentially as a diode.

this J–V curve that determine the power conversion efficiency as well as reflect the underlying charge transport properties of the solar cell. The first is the magnitude of the current density when no voltage bias is applied (i.e., the y-intercept of the J–V curve), which is referred to as the short-circuit current (J_{SC}). In organic solar cells, the short-circuit current is dependent on the fraction of incident photons that are absorbed as excitons and subsequently split into free charges (internal quantum efficiency), as well as the fraction of free charges that are successfully extracted from the device as electrical current (external quantum efficiency). However, operating a solar cell at short-circuit conditions does not result in electrical power; since there is no applied bias, no power can be dissipated by the device. In order to obtain useful electrical power, the device must be operated under a voltage bias. At low biases, increasing the applied voltage increases the power output of the device. However, at sufficiently high biases, the applied voltage counteracts the photocurrent until at a certain point, referred to as the open-circuit voltage (V_{OC}), the photocurrent drops to zero. Like the short-circuit condition, no electrical power can be generated at this point. The maximum power point must therefore occur at some applied bias less than V_{OC}, at a current

density less than the J_{SC}. The V_{OC} is determined by several factors, including the bandgap of the active materials, the degree and type of carrier recombination, and the identity of the device's metallic electrodes.

When examining a J–V characteristic, the ratio of the product of current density and voltage at the maximum power point to the product of J_{SC} and V_{OC} (the theoretical power) is known as the device's fill-factor (FF):

$$FF = \frac{J_{max} \times V_{max}}{J_{SC} \times V_{OC}} \tag{1.1}$$

Graphically speaking, the fill factor of a solar cell is a measure of how rectangular the device's J–V characteristic is. In organic solar cells, the fill-factor is considered to be a measure of how beneficial a device's morphology is to charge transport. These three figures of merit determine the device's efficiency, η, which is given by:

$$\eta = \frac{P_{max}}{P_{incident}} = \frac{J_{SC} \times V_{OC} \times FF}{P_{incident}} \tag{1.2}$$

where $P_{incident}$ is the incident radiant power, which is typically measured with the standard AM1.5 solar spectral irradiance. These three figures of merit (J_{SC}, V_{OC}, and FF) will be the discussed and analyzed in detail for special cases throughout this dissertation, since they not only determine the a solar cell's overall power conversion performance, but also provide information about the charge transport properties of organic solar cells, as we shall soon illustrate.

1.4 Modeling Charge Transport in Organic Photovoltaics: Drift-Diffusion Modeling Overview

In addition to the massive amount of empirical research into OPV device performance, a significant amount of theoretical work also has been applied. The scope of such theoretical investigations is wide, including *ab initio* studies of individual OPV molecules, Monte-Carlo

modeling of charge transport, equivalent circuit analysis, and more.[8, 183, 26, 153] One of the most popularly applied methods is drift-diffusion modeling of charge transport.[74] At its heart, a drift-diffusion simulation involves solving the charge carrier continuity equations:

$$\frac{\partial n}{\partial t} = G + R + \frac{1}{q}\nabla \cdot J_n \tag{1.3}$$

$$\frac{\partial p}{\partial t} = G + R - \frac{1}{q}\nabla \cdot J_p, \tag{1.4}$$

which account for all possible gain and loss mechanisms for the electron and hole densities, given by n and p, respectively. For organic solar cells (under illumination) the dominant generation mechanism, G, of free carriers is via exciton dissociation events following the absorption of photons. The R term in Eqs. (1.3) and (1.4) represents the loss rate of charges due to recombination events and is usually a function of electron and hole density. Recombination of free charges can occur either directly (between free electrons and free holes) or indirectly through a trap-mediated process. Although both recombination mechanisms are known to occur in OPV devices, there is still some debate over which mechanism is dominant; therefore, we will consider both at various points in this dissertation. The current density gradient term ($\nabla J_{n,p}$) in Eqs. (1.3) and (1.4) accounts for any local current imbalance which may lead to either an accumulation or depletion of charge density. This term can therefore function as either a gain or loss mechanism of carrier density, depending on the local environment.

According to the drift-diffusion model, the charge carrier current densities are given by:

$$J_n = -q\mu_n n\nabla V + \mu_n k_{\mathrm{B}} T \nabla n \tag{1.5}$$

$$J_p = -q\mu_p p\nabla V - \mu_p k_{\mathrm{B}} T \nabla p \tag{1.6}$$

where $\mu_{n,p}$ is the mobility of electrons and holes, V is the electrostatic potential, and k_{B} and T are Boltzmann's constant and the absolute temperature, respectively. The drift-diffusion model asserts that there are two types of charge carrier motion which contribute

to the current density: a drift term, whereby charges move in response to an electric field ($\vec{E} = -\nabla V$) and a diffusive term, whereby charges move in response to a carrier density gradient.

A final complicating factor for solving Eqs. (1.3) and 1.4 is that the carrier densities are inherently coupled to each other via Gauss's Law:

$$\nabla \cdot \vec{E} = \frac{\rho}{\epsilon_r \epsilon_0} = \frac{q}{\epsilon_r \epsilon_0}(p - n + C) \tag{1.7}$$

where ϵ_0 and ϵ_r are the vacuum and the relative permittivity and C is the density of immobile or trapped charges. When expressed in terms of the electrostatic potential, as it is typically treated computationally, this reduces to Poisson's equation:

$$\nabla^2 V = \frac{q}{\epsilon_r \epsilon_0}(n - p + C) \tag{1.8}$$

Equations 1.3, 1.4, and 1.8 represent a coupled set of nonlinear, partial differential equations in multiple dimensions with three dependent variables (n, p, and V). We choose to solve the above set of equations by decoupling and solving them in an iterative, self-consistent manner.[58] The individual equations are solved by discretizing them and solving for the dependent variables on a finite difference mesh, which represents the active layer of the device.[162] For further details on the implementations of this method, as well as a basic operations guide to our software, see the Appendix D. Similar approaches to solving the semiconductor equations have been extensively applied to model organic photovoltaics.[75, 94, 172, 141] With this methodology in hand, we now turn to applying it to study the effects of an organic photovoltaic's active layer morphology on its transport properties.

1.5 Case studies of morphological effects in OPV charge transport

In this dissertation, we present a series of drift-diffusion modeling studies focused on exploring the effects of OPV morphology on the charge transport properties of OPV devices and their subsequent device performance. One anomalous feature of organic solar cells is the

appearance of the so-called S–curve.[38] As mentioned in section 1.3, most OPVs exhibit a diodic J–V curve that is approximately rectangular. However, occasionally an OPV device will exhibit a inflection point near the device's V_{OC}, resulting in a S–shaped J–V curve. Although such devices may posses high J_{SC} and high V_{OC}, the inflection point in their J–V characteristic results in an unusually low FF, and thus low power conversion efficiency. Several hypotheses have been suggested as to the underlying cause of these spontaneously-occurring S–curves, such as imbalanced carrier mobilities[174] or energetic barriers for charge extraction at the contacts.[61, 53] Experimental evidence suggested that S–curve devices were characterized by a dearth of fullerene near the cathode (i.e., little fullerene at the top of the film, which is the point of electron extraction), as the result of vertical phase segregation.[38]

To better understand the origins of the S–curve, we decided to examine simulated OPV devices using the D-D model, particularly because early versions of our modeling software were limited to considerations of charge transport in only one dimension, making this an opportune system to simulate. To test the hypothesis that vertical phase segregation of conducting material away from an extraction contact could produce S–curve devices, we simulated a series of devices that were characterized by high mobility for carriers throughout the majority of the device, but with a precipitous drop in electron mobility in proximity to the cathode. Simulated devices with this characteristic mobility profile did indeed result in S–shaped J–V curves. We also simulated devices with imbalanced charge carrier mobilities, exponentially decaying mobility profiles, and excessively high Schottky barriers. Although all of these methods resulted in poorly performing devices (lowered J_{SC} and V_{OC}), none of them exhibited S–shaped J–V characteristics. The results of this study and the conclusions drawn from them were published in the journal of *Applied Physics Letters* in 2013.[51] The results of this modeling study not only verified our collaborators' original hypothesis, but clearly illustrated how an OPV's compositional morphology can have a striking impact on its resulting performance.

In the next chapter of this dissertation, we present a modeling study that further examines the effects of OPV devices' compositional morphology on their resulting power conversion performance. In particular, this study aimed to elucidate the exact effects of the structural

disorder of the BHJ morphology on an OPV's charge transport properties. At the time of this study's publication, our drift-diffusion modeling software was still limited to 1-dimensional devices. To overcome this limitation, we developed an approach to model the tortuous charge transport pathways of the BHJ morphology based upon an ensemble-averaging technique, which we published in the journal of *Physical Review Applied* in 2015.[52] In this approach, a collection of charge carrier mobility profiles were generated by randomly sampling mobility values from a normally distributed probability distribution. With this approach, each of the device "replicas" generated from random sampling have a unique mobility profile and may possess regions of excessively high or low carrier mobilities. Each device replica can be viewed as a single charge transport pathway through the active layer of the device; some are conducive to charge transport while others are highly unfavorable to charge transport and represent the tortuous pathways present in BHJ devices. By averaging over many of these replicas, we were able to draw conclusions about the general effects of structural disorder on OPV charge transport. Our simulations showed that the introduction of structural disorder to an OPV's active layer results in a significant drop in performance, depending on the degree of disorder. The largest detriments to performance were seen in the J_{SC} and *FF*, while the V_{OC} remained relatively impervious to the debilitating effects of structural disorder. Examination of the replicas' carrier densities revealed that the inclusion of structural disorder results in the accumulation of charges as carrier more slowly traverse tortuous pathways. The accumulation of charges within a device results in greater losses of free carriers to recombination, causing the observed drops in J_{SC} and *FF*. This illustrates the critical role that an OPV's morphology plays in its charge transport characteristics

Although the our 1-D ensemble approach allowed us to probe the general effects of morphological disorder, it was still a relatively crude approximation of the convoluted and tortuous morphologies present in an actual BHJ. Furthermore, 1-D modeling is unable to examine more subtle, yet important structural details of OPV devices and their effects on charge transport and device performance. For instance, although donor and acceptor materials normally phase segregate into distinct domains in BHJ morphologies, there exists a third, mixed-composition phase at the interface between the pure component domains. It is unclear what

effect this mixed-phase has on the charge transport properties of OPV devices, although some have argued that the presence of a mixed phase is crucial to device performance.[73, 21] Our 1-D ensemble approach was completely incapable of examining such effects to any acceptable degree of accuracy. Therefore, we extended our drift-diffusion modeling software to account for 2-dimensional charge transport. We utilized morphological data obtained by high angle annular dark field (HAADF) scanning tunneling electron microscopy (STEM) to investigate the effects of an mixed-phased, interfacial region on device performance.[186] In addition to empirical morphologies, we also simulated a series of computer generated morphologies created by modeling the phase separation dynamics of binary fluid mixtures (Cahn-Hilliard integration). These Cahn-Hilliard morphologies were implemented to study the effects of the mixed-phase over a wide range of configurations representing different ratios of pure to mixed-composition domain size. Our simulations showed that the inclusion of a mixed-phase may both improve and hinder device performance. At low degrees of mixing, the mixed-phase region lessened the tortuosity of the conduction pathways, reducing charge accumulation and generally aiding charge transport. The act of mixing can also create new conduction pathways from regions that were previously disjointed. However, at higher degrees of mixing, the mixed-phase actually narrowed the highest conductivity pathways, resulting in poorer charge transport overall and diminished power conversion efficiency in particular. The maximum power conversion efficiency occurred at different degrees of mixing, depending on the average domain size of the morphology and various other morphological details. The optimum fraction of mixing was determined to range between 15–25%, though one particular simulated device benefited from as much as 50% mixing. This demonstrates that a subtle balancing act occurs when attempting to engineer the optimum morphology for a given donor/acceptor pairing: either insufficient or excessive mixing of the two components can significantly hinder an OPV device's resulting power conversion performance. At the time of this dissertation's writing, we are in the process of submitting a manuscript presenting these results for publication.

Our drift-diffusion modeling studies were not only limited to investigations of the effects of morphology on OPV performance. It was also used to simulate a variety of time-

dependent device measurements, specifically the photo-CELIV and transient photocurrent techniques.[121, 109] A collaborator of this researcher, Dr. Stephen Hawks, had developed an analytic formalism for reinterpreting these techniques. His formalism involved identifying and separating the different charge transport processes (direct loss of carrier density, recombination through traps, displacement currents, surface recombination currents, etc.) which occur within thin-film organic solar cells and how these processes each contribute to the total measured current. To assess the veracity of this model, we simulated similar transient techniques. Data extracted from those simulations (carrier densities, electrostatic potential, recombination rates, etc.) were analyzed and used to reconstruct the different current contributions described by Dr. Hawks's formalism. Our simulated data was found to be completely self-consistent with Dr. Hawks' formalism and we published the results of this study in the journal of *Physical Review Applied* in 2015.[68] This served to verify both the analytic model and the numerical simulation and further extend the applicability of our drift-diffusion modeling capabilities to a wider range of experimental techniques.

In summary, the main focus of this dissertation has been to determine how one of an organic solar cell's main idiosyncrasies, the internal morphology of its active components at the $\sim$10 nm length scale, affects its charge transport properties and resulting power conversion efficiency, by means of semiconductor device modeling via the drift-diffusion model of charge transport. We have shown how phenomena particular to OPVs (the random occurrence of S–shaped J–V characteristics, their high sensitivity to variations in processing conditions, difficulties in scaling up to larger active areas, etc.) may be attributed to an individual OPV device's nanoscale morphology. Although one of the initial hopes for OPV technology would be that it would serve as a panacea to the world's energy problems, the truth is that the bulk-heterojunction architecture is inherently susceptible to morphological defects. This underscores the need for new processing techniques, such as sequential processing of BHJ films[4], that may allow for precise and reproducible tuning of film morphology if polymer-based solar cells are to become competitive with other renewable energy technologies.

CHAPTER 2

Understanding the Origin of the S–curve in Conjugated Polymer/Fullerene Photovoltaics from Drift-Diffusion Simulations

Organic solar cells have emerged as a potentially viable source of renewable energy, with power conversion efficiencies (PCEs) reported to be as high as 10%. Unfortunately, it is difficult to maintain such high efficiencies when scaling organic photovoltaics (OPVs) from laboratory scales to mass production because the nanometer-scale morphology of the bulk heterojunction (BHJ) active layer depends sensitively on the kinetics of how the films are processed. This sensitivity to processing kinetics is so extreme that it is often difficult to reproducibly obtain PCEs for a given set of materials from day to day. As an example of this lack of reproducibility, organic solar cells sometimes exhibit an S–shaped current-voltage curve, resulting in low PCE because of a significantly reduced fill factor (FF), even if the short circuit current (J_{SC}) and open circuit voltage (V_{OC}) remain high. Thus, understanding the cause of S–shaped JV curves would help to allow for the rational design of OPV devices, thus improving their reproducibility and potential industrial feasibility.

Several groups have proposed hypotheses to explain the appearance of S–shaped J–V curves in OPVs. Early work suggested that the problem involved diminished electron extraction due to defects at the cathode interface.[61, 53] Others have argued that an imbalance of the individual charge carrier mobilities would induce S–shaped J–V curves, and this has been demonstrated for planar junctions (bilayer solar cells).[174] This explanation does not appear to extend to typical BHJ devices, however, since organic donor/acceptor blends often have uneven hole and electron mobilities, which would mean that S–shaped J–V curves

would be more common if charge mobility imbalance alone was the primary culprit. We previously have argued that S–shaped J–V curves in OPVs result from vertical phase separation of the two organic components,[38] for example, when the fullerenes that carry the electron current sink towards the bottom contact and away from the cathode. Our evidence included surface topographic measurements that indicated that the interface between the active layer and the cathode in S–curve devices was deficient in fullerene, that S–curve devices had a double peak in the current extracted in photo-CELIV experiments, and that the S–curve could be subsequently removed if additional fullerene was deposited on the top surface before application of the cathode contact.[38]

In this letter, we utilize drift-diffusion modeling to investigate the cause of S–shaped J–V curves in BHJ organic solar cells. We take advantage of the approach of Häeusermann et al. to simulate OPVs, approximating the BHJ as a 1-D device treated as an effectively uniform medium.[62] We used the Gummel method[58] to decouple the charge carrier continuity and Poisson equations which make up the drift-diffusion model and assumed thermionic injection at the contacts as boundary conditions for the electron and hole densities.[150] In order to account for thin-film interference effects, we used the Petterson transfer matrix method[135] to calculate the spatially dependent absorption profile that determines the initial generation of charge carriers for the continuity equations. For this calculation, we assumed that the active layer had the optical characteristics of poly-3-hexylthiophene (P3HT) and that every exciton immediately splits into an electron and a hole (an assumption justified by the fact that the exciton diffusion length in P3HT is thought to be small compared to the spatial variation of the carrier generation profile).[60] Finally, we also assumed a bimolecular Langevin mechanism[93] to account for the recombination of electrons and holes. All the pertinent parameters for our simulations are collected in Table 2.1.

We began by testing the supposition that imbalanced charge extraction rates as a result of a carrier mobility mismatch might be responsible for the appearance of S–shaped J–V curves in BHJ devices. We simulated the J–V characteristics of a series of BHJs with increasingly mismatched carrier mobilities. Our initial calculation assumed matched electron and hole mobilities with a numerical value of 1×10^{-4} cm^2/Vs. We then decreased the electron mobility

Parameter	Symbol	Value
Hole mobility	μ_p	1×10^{-4} cm V^{-1} s^{-1}
Electron mobility before drop-off	μ_{n0}	1×10^{-4} cm V^{-1} s^{-1}
Electron mobility after drop-off	y	1×10^{-6} cm V^{-1} s^{-1}
Abruptness of drop-off	σ	1.0
Distance of drop-off from cathode contact	X	20 nm
Thickness	d	100 nm
Relative permittivity	ϵ	3.5
Injection barrier for electrons and holes	$\varphi_n,\ \varphi_p$	0.3 eV
Recombination efficiency	η	0.5
Built in voltage	V_{BI}	0.6 V
Density of chargeable sites	N_{C}	1×10^{26} m^3
Temperature	T	298 K

Table 2.1: The boundary conditions and parameters used for the D-D simulations presented in the figures, except where otherwise noted.

by over 5 orders of magnitude, producing the J–V characteristics shown in Fig. 2.1(a). Our calculations plainly show that although mismatched carrier mobilities can significantly reduce the PCE and *FF* of BHJ solar cells, mismatched carrier mobilities alone are not responsible for the characteristic S–shaped J–V curve, in line with our arguments above. We next investigated the hypothesis that difficulty with extraction of one of the carriers at a contact is responsible for the appearance of S–shaped J–V curves. To simulate the effects of poor electron extraction near the cathode, we modeled the spatial mobility profile of the electrons using a sigmoid function

$$\mu(x) = \frac{\mu_{n0}}{1 + \exp(\sigma(x - X))} + y \tag{2.1}$$

Such a function results in a smooth drop-off in electron mobility in one region of the active layer. In this sigmoid function, σ and X control the sharpness and position of the mobility drop-off, respectively, while y represents for the non-zero mobility of electrons in P3HT as they are extracted from the cathode; for y, vertical phase separation characterized by fullerenes drifting away from the cathode, an interfacial extraction barrier, blocking contact, or surface recombination all could cause this mobility to be up to several orders of magnitude less than μ_{n0}, the electron mobility in the region before the drop-off. We chose to leave the

hole mobility constant in this region and throughout the device.

There are three parameters in the mobility profile of Eq. (1) that could potentially influence the character of the resulting simulated J–V curve: the position within the device where the mobility drop-off begins (X), the mobility of the carrier beyond the drop-off point (y), and the steepness of the drop-off (σ). We explore the effects of varying each of these parameters on the device J–V curves in Figs. 2.1(b)–2.1(d); the insets show the mobility profiles used for each J–V curve. Since Fig. 2.1(a) can be compared directly to Fig. 2.1(b) in terms of the effectively reduced carrier mobility at the cathode contact, our simulations clearly show that it is not reduced carrier mobility alone but rather the presence of a mobility drop-off (even a relatively small one) that is responsible for producing S–shaped J–V curves in, otherwise, normal BHJ devices. Of particular note is that the S–curve appears when the mobility in the drop-off region is 2 orders of magnitude less for electrons than for holes.

To understand why a mobility drop-off leads to S–shaped J–V curves, we examined the individual (but spatially averaged throughout the device) carrier current densities as a function of the applied voltage, as shown in Fig. 2.2. Even though the hole current exhibits typical diodic behavior (albeit with slightly reduced efficiency), Fig. 2.2 illustrates that the presence of the mobility drop-off for the electrons leads to an electron current with a significant S–shaped character and reduced V_{OC}. Since the total current density is a sum of the individual carrier current densities, the result is a device J–V curve with pronounced S–shaped character. This is in contrast to a normal BHJ device (also plotted in Fig. 2.2), in which both carrier currents exhibit typical diodic behavior.

The cause of the reduction in the spatially averaged current can be further understood by examining the spatial dependence of the current densities at key points along the J–V curve for devices with and without the electron mobility drop-off, as shown in Figure 2.3. At short-circuit conditions, Fig. 2.3(a) shows that the total current is limited by the electron current near the cathode contact. Photogenerated electrons drift towards the cathode until they reach the low mobility region, where they slow to a constant and relatively slow speed. The hole current is also limited in this region, but this does not have an appreciable effect on the total current since the hole density (and thus hole current) is typically low here under short

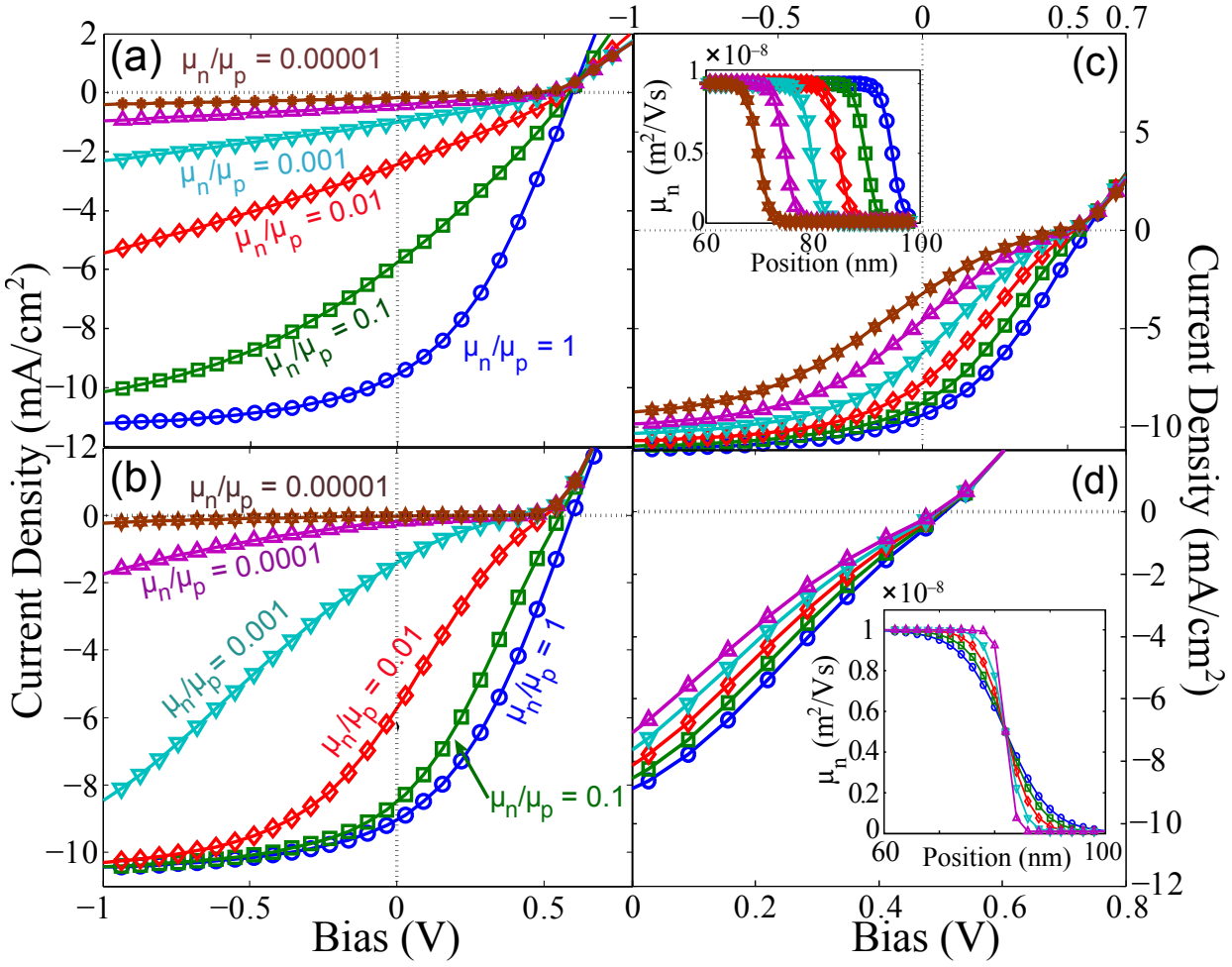

Figure 2.1: Simulated J-V curves analyzed in this study. The electron and hole mobilities are initially equalized to 1×10^{-4} cm^2 V^{-1} s^{-1}. The electron mobility is subsequently reduced by several orders of magnitude in two manners: (a) by decreasing the electron mobility throughout the device and (b) by only decreasing the mobility only near the cathode through the use of a sigmoid profile. Fig. 2.1(a) illustrates the inability of mismatched carrier mobilities to induce an S–curve; Fig. 2.1(b) illustrates that a sigmoid-shaped electron mobility profile is capable of inducing an S–curve. The effects of the different features of the mobility profile are explored by increasing the size (c) and abruptness (d) of the mobility drop-off, as illustrated in the insets over an expanded spatial region of the 100-nm thick device active layer. Increasing the region of reduced mobility and the abruptness of the drop in mobility results in a more pronounced S–curve character.

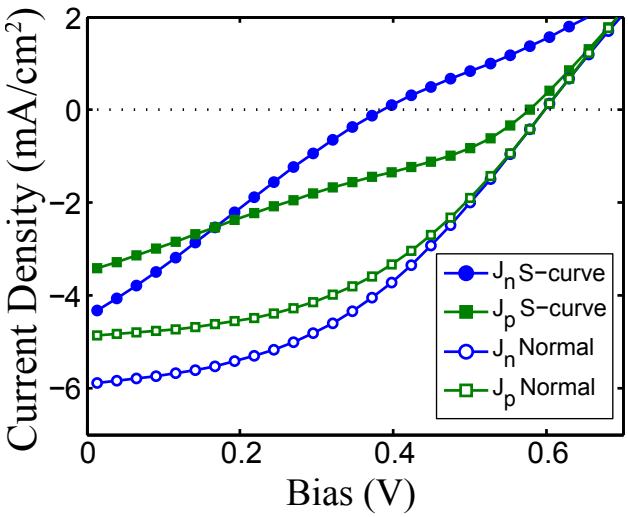

Figure 2.2: Individual charge carrier currents for S–curve (solid symbols, device parameters given in Table 2.1 and normal OPV (open symbols, no mobility drop-off) devices. The normal device shows typical J–V diodic behavior for the individual carriers, but the device with the mobility drop-off has a severely distorted J–V character, particularly for the electron current (blue curves).

circuit conditions. As the voltage is increased, Fig. 2.3(b) shows that the electron and hole currents gain a positive and negative slope, respectively. According to the current gradient term in the continuity equation, this reverse in slope results in a buildup of space charge near the cathode, explaining why the electron current becomes limited at this voltage. At higher applied biases (V_{OC} and beyond), this gradient inversion is diminished, and the J–V characteristic behaves as a normal OPV device as the charge carriers begin moving towards their reverse contacts. In this case, electron transport is no longer hampered by the mobility drop-off as the electrons are extracted through the anode instead of the cathode. Similarly, hole extraction is not restricted at the cathode since hole mobility is kept at sufficiently high in the pure P3HT there, in accordance with the phenomenon of vertical phase segregation. Taken together, this explains why the electron current has such a strong S–shape: the electron current becomes limited at intermediate voltages where there is significant space-charge build-up but then approaches normal values once V_{OC} is exceeded.

In summary, we have shown that a simple mobility profile characterized by drop in conductivity near one of the contacts is sufficient to induce an S–shaped J–V curve in a simulated organic photovoltaic device. Such a mobility profile, in which there is an imbalance

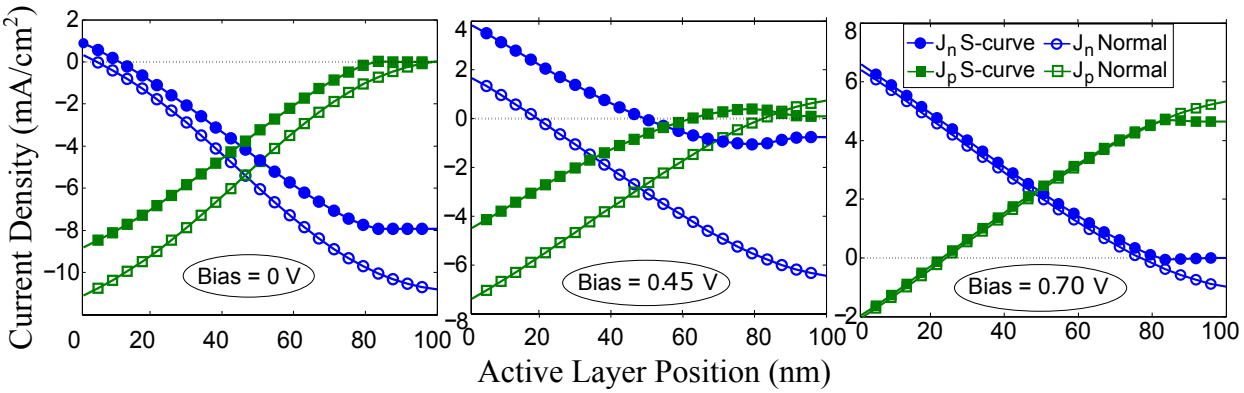

Figure 2.3: Spatially discretized electron current (J_n) and hole current (J_n) at various applied voltages for both an S–curve device (solid symbols, parameters given in Table 2.1) and a normal BHJ device (open symbols, no mobility drop-off). The currents are shown at applied voltages corresponding to (a) short circuit conditions, (b) near the inflection point of the J–V curve, and (c) beyond V_{OC}. In panel (b), there is severe distortion of the individual carrier currents for the S-curve device, which results in a reduced total current and an inversion of the current gradients, resulting in a buildup of charge. At higher biases, the severity of this inversion is reduced, and normal behavior is re-established.

in carrier mobility at only one of the contacts, would certainly arise as a result of vertical phase segregation, a blocking contact or other interfacial effects. The results are consistent with our earlier suggestion that subtleties in processing conditions that produce vertical phase segregation are a likely culprit for the appearance of S–curves in BHJ devices.[62] Thus, to avoid irreproducibility in device performance from changes in processing conditions, it would make sense to employ techniques that are less susceptible to kinetics, such as sequential deposition of the donor and acceptor materials.[9]

CHAPTER 3

Drift-Diffusion Modeling of the Effects of Structural Disorder and Carrier Mobility on the Performance of Organic Photovoltaic Devices

3.1 Introduction

Organic photovoltaic (OPV) technology has seen marked improvement in recent years, with device power conversion efficiencies (PCEs) surpassing 11% [194]. The most efficient devices are constructed from blends of a semiconducting polymer, which acts as the light absorber and hole transporter, and a fullerene derivative, which serves to separate the excitons created on the polymer and to transport the electrons. Such polymer/fullerene mixtures, known as bulk heterojunctions (BHJs), must be both intimately blended to assure good charge separation, yet phase separated enough to ensure that there are physically continuous conducting pathways for both the electrons and holes to reach their respective electrodes [189]. The BHJ morphology, however, is difficult to control, and as a result, the relationship between the morphology of the disordered donor/acceptor blends in OPVs and the underlying mechanisms of charge generation, recombination, and transport in such disordered systems is not well understood [107].

In addition to all of the experiments that have been performed to elucidate structure/property relationships in OPVs, there also has been a significant amount of theoretical work, particularly in the field of device modeling [74, 173, 171]. The most commonly employed approach is the drift-diffusion (D-D) model, which has been utilized to simulate a wide variety of OPV device physics experiments, such as J–V characteristics, photo-CELIV,

transient photocurrent measurements, etc. [11, 127, 75]. One feature that is often neglected in D-D simulations, but is of particular importance for OPV devices, is the role of disorder of the organic active layer. Most D-D simulations treat the BHJ blend as a uniform, continuous medium that is characterized by a single mobility for each carrier [74, 173, 180, 172, 174, 134]. Disorder has been accounted for primarily from the perspective of energetic disorder in BHJ blends, which arises from the fact that the polymers in OPV active layers twist and bend along their conjugated backbone and the fact that both the polymer and fullerenes in BHJ blends reside in distinct chemical environments [178, 16]. Several groups have modeled this energetic disorder by including a Gaussian-shaped density of energy states in their D-D simulations, which affects both carrier mobility and recombination [178, 16]. In addition to a Gaussian-distribution, groups also have considered an exponential distribution of trap states [87, 30, 76] These groups find that the simulated performance of devices with energetic disorder is reduced as a result of diminished short-circuit current, fill-factor, and open-circuit voltage.

Despite the progress made towards understanding the role of energetic disorder in BHJ devices, few drift-diffusion simulations have addressed the structural disorder that is also present in BHJ devices or how this disorder impacts carrier transport. By structural disorder, we mean the random spatial distribution of polymers and fullerenes that is found in a BHJ, resulting in tortuous pathways for carrier transport. The existence of structural disorder clearly affects the net carrier mobility. For example, many experiments, including photogenerated charge extraction by linearly increasing voltage (photo-CELIV), transient photocurrent (TPC), and space charge limited current (SCLC) measurements, have shown that on device length scales, the carriers in polymer:fullerene OPVs have relatively low mobilities, on the order of 10^{-4} cm^2 V^{-1} s^{-1} [136, 109, 182]. In contrast, time resolved microwave conductivity (TRMC) measurements indicate that over short length scales, the photogenerated charge carriers in these systems have relatively high mobilities ($\sim$$10^{-2}$ cm^2 V^{-1} s^{-1}), comparable to what is seen in FET-based mobility measurements [3, 160, 110]. Clearly, when carriers move on length scales that sample the spatial disorder inherent in BHJ OPV devices, the result is a lowering of the effective carrier mobility by roughly two

orders of magnitude. These differences in mobility at varying length scales can be understood from the fact that intrachain transport is characterized by significantly higher mobility than interchain hopping, yet interchain hopping is the dominant transport mechanism for disordered semiconducting polymers [97, 128]. All of this suggests that due to structural disorder, the conducting pathways in a BHJ have a distribution of regions with high and low carrier mobility, as opposed to a single continuous mobility.

Structural measurements based on X-ray diffraction and various microscopies have indicated that both the polymers and fullerenes in a BHJ phase segregate into crystallites with sizes on the order of several nanometers, with amorphous and potentially intermixed regions surrounding the crystallites [193, 177, 117, 38, 187]. This means that structural disorder is inherent to polymer:fullerene OPVs. The goal of this work is to use D-D modeling specifically to understand the effects of this structural disorder on the performance of BHJ photovoltaic devices. We note that previous studies that have included a functional dependence of mobility on factors such as the electric field, carrier density, or the energetic density of states, have still been limited to smooth, non-spatially varying mobility profiles and thus have not accounted for the spatial distribution of conductivities present in a BHJ architecture [178, 90, 91]. This means that previous studies have not considered how the grain boundaries between conducting materials or between crystalline and amorphous regions affect mobility and obstruct charge transport. It is clear that to accurately model a BHJ device, one should consider structural disorder in addition to energetic disorder.

In this work, we present a new approach to account for structural disorder in 1-D drift-diffusion modeling of OPV devices. Our work at this stage intentionally neglects the effects of energetic disorder, which would be expected to accompany structurally disordered morphologies, in order to isolate the effects of structural disorder alone on OPV device physics. We present two methods for generating spatially-disordered mobility profiles: one method where each profile is generated by random sampling from a probability distribution of possible carrier mobilities, and a second method where profiles are generated from the disordered morphologies generated by Cahn-Hilliard (C-H) modeling [50, 17]. Both sampling methods result in mobility profiles that contain regions of exceptionally high and/or low mobilities for

the carriers. A high mobility region represents transport along a single chain or through a region of the material with high crystallinity and thus high carrier conductivity. Conversely, a low mobility region represents transport of a carrier through the 'wrong' conducting material or through a grain boundary or defect, or represents the occurrence of dead-ends and other features of the meandering conduction pathways present in BHJ architectures [153]. Our method then treats devices as ensembles of these 1-D disordered carrier pathways.

We demonstrate that as the parameters for both methods (the characteristics of the mobility distribution and the parameters used to transform the 1-D C-H morphologies into structurally-disordered mobility profiles) are varied, there are profound effects on the resulting performance of the ensemble-average modeled disordered devices. We also show that no matter how the disordered mobility profiles are generated, the resultant effects on device performance are similar, indicating that our findings are robust to the details of how structural disorder is included in drift-diffusion simulations. Our simulations show that, similar to studies of energetic disorder, structural disorder leads to an overall degradation of device performance, particularly in regards to the short-circuit current (J_{SC}) and fill factor (FF). However, unlike studies on energetic disorder, we do not find a significant degradation of the open circuit voltage (V_{OC}), and we discuss in detail the reasons why structural disorder has these particular effects on device performance. We also see that the length scale of disorder is important, with the most severe effects on device performance accompanying disorder on length scales of $\sim$10 nm, exactly the size expected in real BHJ OPV devices.

3.2 Computational Methods

3.2.1 Drift Diffusion Model

For this work, we perform all of our device simulations using the D-D model, in which the electron and hole current densities are treated as:

$$J_n = -qn\mu_n\nabla V + kT\mu_n\nabla n \tag{3.1}$$

$$J_p = -qp\mu_p \nabla V - kT\mu_p \nabla p \tag{3.2}$$

where q is the fundamental charge, V is the electrostatic potential, n and p refer to the electron and hole densities, and μ_n and μ_p refer to the mobility of electrons and holes, respectively [90]. In order to simulate a device, one needs to solve the continuity equations for both carriers:

$$\frac{\partial n}{\partial t} = \frac{1}{q}\nabla \cdot J_n - R + G \tag{3.3}$$

$$\frac{\partial p}{\partial t} = -\frac{1}{q}\nabla \cdot J_p - R + G \tag{3.4}$$

where R is the net recombination rate of electrons and holes, which we treat with Langevin recombination of the form $R(x) = \frac{q}{\epsilon_r \epsilon_0}(\mu_n + \mu_p)np$, where ϵ_r is the dielectric constant of the medium and ϵ_0 is the vacuum permittivity. The G term in Eq. (3.3) is the generation profile within the active layer of the device. Since free carriers are assumed to be generated primarily as a result of photon absorption, we calculate this generation profile via a transfer matrix formalism to account for thin-film interference and the absorption/refraction of light by the various layers of an OPV device [135]. To solve the above carrier continuity equations, they need to be coupled through the Poisson equation:

$$\nabla^2 V = \frac{q}{\epsilon_r \epsilon_0}(n - p) \tag{3.5}$$

The set of Eqs. (3.1)-(3.5) forms the basis of the drift-diffusion model.

We used the Gummel method to decouple the above set of partial differential equations and solve the D-D model in an iterative manner [58, 147, 152, 162]. Our simulations provide a 1-D model for a typical OPV architecture, where the organic active layer is sandwiched between two metal contacts. The drift-diffusion model equations were solved numerically for this active layer by discretizing the equations on a finite difference mesh. Because our

structural disorder model examined the effects of feature sizes of only a few nanometers, we tested grid spacings as low as 0.1 nm, but found that as long as the mesh size was less than 1/4 of the disorder length scale, the results were numerically robust. Thus, in most of what is shown below, a 1-nm mesh spacing was used. As boundary conditions for the carrier density equations, we assume thermionic injection at the metal-organic semiconductor interfaces [150]. As boundary conditions for the Poisson equation, we assume that the voltage drop across the device is equal the built-in voltage. We chose the other devices parameters to be comparable to those previously used in the literature, and all the parameters we used in our calculations are collected in Table 3.1. Additional computational details regarding our D-D simulations are given in Appendix A.

We note that similar approaches for OPV device modeling based on the D-D model have been previously implemented by many groups with great success [74, 173, 178, 90]. The primary difference between the previous studies and ours is the explicit inclusion of spatially-dependent carrier mobilities (μ_n and μ_p). The vast majority of previous 1-D drift-diffusion studies have simply assumed a constant mobility value for electrons and holes, without taking into account the meandering conduction pathways (i.e., structural disorder) that carriers are known to traverse in a BHJ architecture. Spatial disorder of the mobility profiles has its greatest effect through the current gradient terms of Eqs. (3.3) and (3.4), as both the drift and diffusion current contributions are proportional to the carrier mobilities. The recombination rate also will be affected due to its functional dependence on the structurally disordered mobility profiles. Generation of free carriers also should be dependent on morphology, since carriers should be predominantly generated near the interface of the donor and acceptor materials. However, we have chosen to neglect the spatial dependence of free carrier generation on the mobility profile for these simulations and instead assume an effective medium approach via the transfer matrix formalism. We believe this is a reasonable approximation since the diffusion length of excitons in OPV materials ($\sim$10 nm) [115] is generally larger than the feature sizes considered in our disordered mobility profiles.

3.2.2 Disordered Mobility profiles and Ensembles

3.2.2.1 Random Sampling from a Mobility Distribution

As one way to approximate structural disorder in one dimension, we utilize an ensemble of spatially variable mobility profiles. To create such an ensemble, we first generate mobility profiles by randomly sampling mobility values from a distribution of possible mobilities. We will discuss the details of this distribution shortly. Starting from one end of the device and progressing to the opposite end, we assign a new, randomly sampled mobility value every δ nm to each of our carrier mobility (μ_n and μ_p) profiles. Our motivation for choosing spatially-dependent mobility profiles in this way is based on the fact that a charge carrier moving through a disordered BHJ architecture can be expected to encounter many potential obstacles, such as grain boundaries, different conducting components, amorphous regions, and structural dead-ends where the charge carrier is no longer capable of conducting through a continuous pathway towards its extraction contact without reversing direction. Experimental measurements have shown that carrier conduction through the 'wrong' conducting material (i.e., holes through the fullerene or electrons through the polymer) has an effective mobility that is several orders of magnitude lower than carrier mobility through the 'correct' conducting material [89, 6]. Thus, while traversing even the most conductive possible pathway(s) through an OPV device, a carrier may experience a range of mobilities that vary by several orders of magnitude.

It is worth noting that simple distributions, such as a Gaussian distribution, cannot generate mobilities that sample such a large range of mobility values. Instead, we chose the exponent of the mobility distribution to follow a Gaussian distribution in order to generate random mobility profiles than span several orders of magnitude. In this way, we create mobility profiles such that:

$$\mu_{n,p}(x) = 10^{(\mu_0 + \sigma \cdot Y(x))} \tag{3.6}$$

where $Y(x)$ is a normally-distributed random variable that determines the mobility at spatial

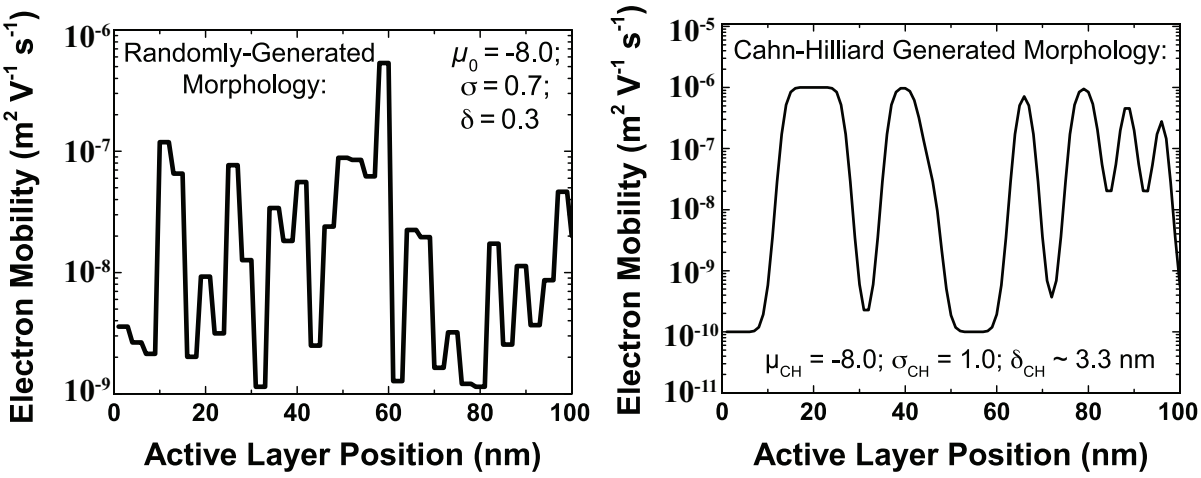

(a) (b)

Figure 3.1: (a) An example mobility profile of a device replica generated by randomly sampling a mobility ensemble characterized by the parameters $\mu_0 = -8.0$, $\sigma = 0.7$, $\delta = 3$ nm. (b) An example mobility profile of a device replica generated by sampling from a Cahn-Hilliard morphology, with $\mu_{\mathrm{CH}} = -8.0$, $\sigma_{\mathrm{CH}} = 1.0$, and average $\delta_{\mathrm{CH}} \approx 3.3$ nm (C-H $\epsilon = 1.6 \times 10^{-5}$).

position x. Thus, Eq. (3.6) provides a mobility distribution whose logarithm has a mean and median of μ_0 and a standard deviation of σ. In this way, we can tune the set of parameters (μ_0, σ, and δ) to define an ensemble from which to generate OPV device replicas, each with a different spatial mobility profile. We present an example mobility profile of one of these replicas in Fig. 3.1. This mobility profile was generated by sampling an ensemble with the parameters ($\mu_0 = -8.0$, $\sigma = 0.7$, $\delta = 3$ nm). Since many such effectively 1-D conducting pathways exist in real OPVs, by averaging over many of these replicas, we can then draw conclusions about the effects of structural disorder on device performance.

Perhaps the single biggest drawback of this approach is that it is still limited to 1-D carrier transport. Thus, our method cannot account for the fact that carriers in real devices are not required to translate through low-mobility regions in 1-D, but may instead move in three dimensions to find a more continuous pathway of relatively high mobility. We note, however, that that charge transport through off-normal dimensions effectively elongates the charge extraction pathway, which results in higher probability that charges will be lost to recombination before extraction. Moreover, the presence of dead ends in 3-D conduction

pathways would result in the buildup of charge carriers, which have no option except to recombine, be transported through the 'wrong' material, or diffuse against their drift vector in order to be extracted. As such, the increased transit time necessary for a charge carrier to find and traverse an OPV device through a continuous pathway can be accounted for as an effective lowering of mobility in the direction of the bulk current flow. Thus, each simulation we perform with a single spatially-dependent 1-D mobility profile can be thought of a single, tortuous pathway through a 3-D device. It is for this reason that we simulate multiple pathways sampled from the same ensemble and only make claims based on the ensemble-averaged behavior.

3.2.2.2 1-D Mobility Profiles Built from Cahn-Hilliard Morphologies

Since the mobility profiles generated by our random distribution may or may not be representative of what a carrier encounters in a working device, we also investigated a second way of generating spatially-disordered mobility profiles. Our second method is based on the Cahn-Hillard (C-H) model, which is used to describe the spontaneous phase separation of binary fluids [17]. We note that the C-H formalism has been used in the past to model the spatial structure of the components in bulk heterojunction solar cells [108, 140, 185]. Our choice to also generate mobility profiles via the C-H formalism allows us to further test the effects of spatial disorder on device performance, by seeing if the way mobility profiles are generated has any significant effect on the results. Thus, we also utilized an ensemble of mobility profiles generated from cross-sections of morphologies determined by solving the Cahn-Hilliard equation [17]:

$$\frac{\partial C}{\partial t} = D\nabla^2(C^3 - C - \epsilon\nabla^2 C). \tag{3.7}$$

In this equation, C is the spatial composition of the binary mixture, which varies from one pure component to another such that $C(x, y) \in [-1, 1]$. We utilize 1-D slices through these morphologies to as a means to generate 1-D mobility profiles with randomized regions of enhanced and diminished mobility. Details of our C-H calculations are given in Appendix A.

The values of the phases generated from the solution to Eq. (3.7) vary in value from -1 to 1, allowing us to generate the i^{th} replica mobility profile as:

$$\mu_i(x) = 10^{\mu_{\text{CH}} + C(x,i)\cdot\sigma_{\text{CH}}} \tag{3.8}$$

In this expression, σ_{CH} and μ_{CH} are analogous to those used in Eq. (3.6). In Eq. (3.6), σ is the standard deviation of the mobility distribution from which mobility profiles were generated, and thus sets the range of possible mobility values that could be found in the ensemble of replica devices. In Eq. (3.8), σ_{CH} is a multiplicative factor that also sets the range of possible mobility values. The quantity μ_{CH} also serves a corresponding role as μ_0 in Eq. (3.6) as the mid-point around which a distribution of mobility values may be found.

The mobility profiles generated via Eq. (3.8) differ from those generated by Eq. (3.6) in two important ways. First, the mobility profiles obtained from Cahn-Hilliard morphologies exhibit a relatively smooth variation in mobility, as opposed to the abrupt changes in our randomly-sampled mobility profiles (see Fig. 3.1). Second, the C-H mobility profiles generated by Eq. (3.8) do not possess a single, constant feature size, δ, in contrast to those generated by Eq. (3.6) that have δ as an explicit an adjustable parameter. The average size of the compositional domains of Cahn-Hilliard morphologies is determined by the interfacial energy term, ϵ, in Eq. (3.7). In C-H calculations, a lower interfacial energy results in a larger interfacial surface area and thus smaller average domain sizes. Therefore, by altering ϵ, we may generate mobility profiles with a varying average domain size, in much the same way that δ is utilized in our random mobility sampling method.

Once the value of ϵ is chosen, we determine the average domain size of our Cahn-Hilliard generated morphologies, δ_{CH} by calculating their radial pair distance distribution function :

$$P(r) = \frac{2}{N(N-1)} \sum_{j>k}^{N} \sum_{k}^{N-1} \delta(r - r_{jk}) \tag{3.9}$$

The average domain size, δ_{CH} is then determined as the distance at which $P(r) = 0.5$ [108]. Thus, the C-H formalism provides a second, independent way to generate an ensemble of

Parameter	Symbol	Value
Active Layer Thickness	d	100 nm
Relative Permittivity	ϵ_r	3.5
Schottky Injection Barriers	ϕ_n, ϕ_p	0.3 eV
Langevin Reduction Factor	γ	0.1
Built-in Voltage	V_{BI}	0.6 V
Effective Density of States	$N_{\mathrm{C}}, N_{\mathrm{V}}$	1×10^{20} cm^{-3}
Temperature	T	298 K
Band Gap	E_g	1.2 eV

Table 3.1: The boundary conditions and parameters used for the D-D simulations presented in the figures, except where otherwise noted.

tunable mobility profiles that can be used to understand the effects of structural order in D-D simulations.

3.3 Results and Discussion

We begin by using both of our methods to generate ensembles of spatially-varying mobility profiles to understand the effects of spatial disorder in drift-diffusion simulations. The initial ensemble of mobility profiles we examined from our random distribution method is characterized by parameters $\mu_0 = -8.0$, $\sigma = 0.7$, and $\delta = 3$ nm. An example of one such spatially-variable mobility profile is presented in Fig. 3.1(a). For our initial Cahn-Hilliard mobility profiles, we sampled a C-H morphology that had an average feature size of $\delta_{\mathrm{CH}} \approx 3.3$ nm, corresponding to an ϵ value of 1.6×10^{-5}. We then used those cross-sections to generate C-H mobility profiles that varied around a central mobility value of 10^{-4} cm^2 V^{-1} s^{-1} and range with composition by two orders of magnitude ($\mu_{\mathrm{CH}} = -8.0$, $\sigma_{\mathrm{CH}} = 2.0$). For further details on our Cahn-Hilliard simulations, see Appendix A.

Once the two ensembles were generated, we then solved the D-D equations for each mobility profile using the boundary conditions collected in Table 3.1 to generate the J–V characteristics of 1000 device replicas for each method. We present a sample of 100 of these replica devices' J–V characteristics for each method in Figs. 3.2(a) and 3.2(b) for the randomly-generated and Cahn-Hilliard calculated profiles, respectively. Each device replica (i.e., each distinct spatially-variable mobility profile) exhibits a different short circuit

current (J_{SC}), open circuit voltage (V_{OC}), and fill factor (FF). Many of the replicas have J–V characteristics that do not appear diodic and thus lead to reduced OPV efficiency in the ensemble average. In particular, the spatial disorder in some of these replica devices produces the so-called 'S-curve', in which there is an inflection point in the fourth J–V quadrant that leads to a particularly poor fill factor and thus poor power conversion efficiency [53].

To understand precisely how spatial disorder affects OPV devices, we examine the average J–V curve for both methods' ensembles in Fig. 3.2(c). For comparison, Fig. 3.2(c) also includes the calculated J–V curve of a 'pristine' device (solid black curve). The pristine device is characterized by a uniform mobility profile whose mobility value is chosen to equal the mean of the distribution from which the device replicas were generated (i.e., $\mu_n = \mu_p = 10^{-4}$ cm^2 V^{-1} s^{-1}). Clearly, even though the average mobilities of both the ensemble devices and the pristine device are the same, the inclusion of spatial mobility disorder leads to a decrease in device performance. In particular, both the fill factor and short circuit current of the spatially-disordered devices suffer in comparison to their pristine counterpart. The open circuit voltage of the ensemble-averaged spatially-disordered devices, however, shows no decrease compared to the pristine device, an observation that we rationalize below.

3.3.1 The Effects of the Range of Disordered Mobilities on Ensemble-Averaged Device Behavior

Now that we have seen the detrimental effects of spatial disorder on device performance, we can examine the how altering the type and degree of disorder affects affects the device physics. The σ and σ_{CH} parameters define the range of possible mobilities and thus the degree of disorder in a given replica. We illustrate the effect of changing the degree of disorder parameter on device performance in Figs. 3.3(a) and (b), which show ensemble-averaged J–V curves with different values of σ and σ_{CH}, respectively. All of these ensembles were chosen to have the same average mobility and spatial feature size, but each has a different range of potential mobility values. For both sampling methods examined, increasing the degree of spatial disorder by increasing the range of possible mobilities monotonically decreases the

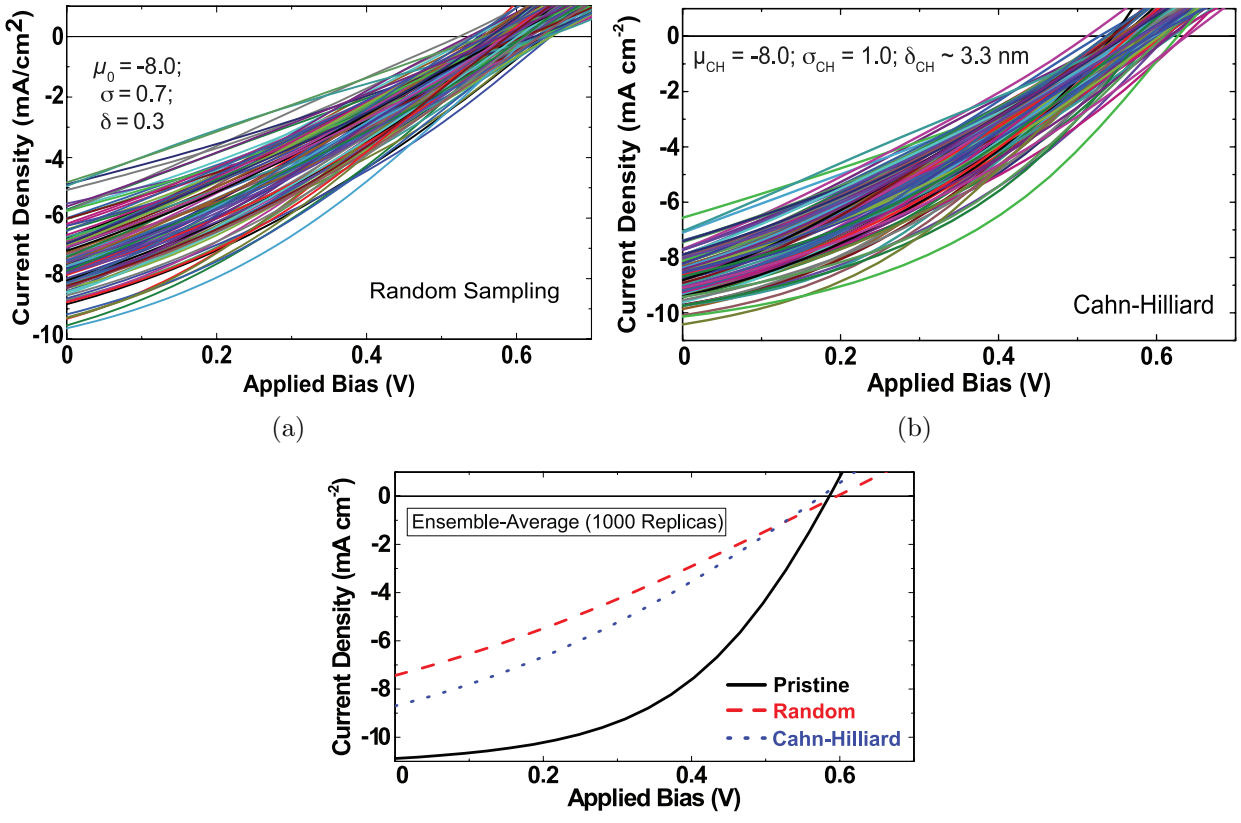

Figure 3.2: (a) A collection of J–V characteristics for an ensemble of replicas randomly generated via the random mobility distribution method using the ensemble parameters $\mu_0 = -8.0$, $\sigma = 0.7$, and $\delta = 3$ nm. (b) A collection of J–V characteristics for an ensemble of replicas sampled from Cahn-Hilliard Morphologies with $\mu_{\mathrm{CH}} = -8.0$, $\sigma_{\mathrm{CH}} = 1.0$, and average $\delta_{\mathrm{CH}} \approx 3.3$ nm (c) The ensemble averaged J–V characteristics for both methods (red-dashed curve for random mobility profiles; blue dotted curve for C-H generated profiles). For comparison, the solid black curve shows J–V characteristic of a non-disordered, 'pristine' device with ($\mu_n = \mu_p = 10^{-4}$ cm^2 V^{-1} s^{-1} throughout the active layer).

ensemble-averaged device performance.

To more thoroughly examine how changes in the degree of disorder affect device performance, Figs. 3.4(a) and (b) illustrate trends in the pertinent figures of merit for device performance as a function of σ and σ_{CH}, respectively. In these plots, the device figures of merit are displayed as the fraction of their value relative to the pristine (i.e., uniform mobility profile) device with the same average mobility. Both the J_{SC} and the *FF* drop as the degree of disorder parameter is increased, resulting in a concomitant drop in power conversion efficiency. Although V_{OC} does eventually begin to decrease for high values of σ and σ_{CH}, this decrease is very small compared to the drops in J_{SC} and *FF*. In fact, by the time σ is large enough to see a significant effect of disorder on V_{OC}, the values of J_{SC} and *FF* are so incredibly low that the device is already effectively non-functional. Thus, V_{OC} can be considered essentially impervious to disorder for the degrees of disorder that are representative of typical performance OPV devices.

Of particular interest is the similarity of performance trends between mobility ensembles generated by random sampling (Fig. 3.4(a)) and those generated by sampling Cahn-Hilliard morphologies (Fig. 3.4(b)). The distributions of possible mobilities for both of these sampling methods are decidedly different. In the former case, the ensembles' mobilities are normally distributed around a mean value, μ_0 of 10^{-4} cm^2 V^{-1} s^{-1}, with values that range from $\sim 10^{-2}$ to $\sim 10^{-6}$ cm^2 V^{-1} s^{-1}. In the latter case, the ensembles' mobilities are roughly bimodally distributed, with the majority of mobilities distributed near 10^{-2} and 10^{-6} cm^2 V^{-1} s^{-1} (see Appendix A for histograms of these distributions). This is a direct result of the fact that Cahn-Hilliard morphologies vary from the extremes of one pure component to the other. The fact that these two very different mobility distributions lead to essentially the same result suggests that the exact shape of the mobility distribution being sampled is less important to device performance than the *range* of possible mobility values and the way such values are spatially distributed, as we discuss further below.

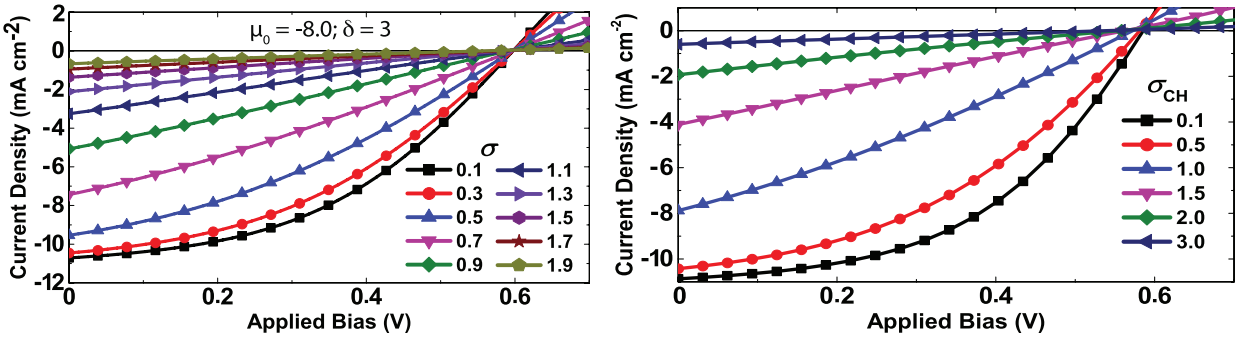

(a) (b)

Figure 3.3: Ensemble-averaged J–V characteristics for several series of replica devices. Each curve is the average of 1000 replicas. (a) Mobility profiles generated from the random distribution method with μ_0 = -8.0 and δ = 3 nm but different values of the degree of disorder parameter, σ, which ranges from 0.1 to 1.9 in steps of 0.2. (b) Mobility profiles generated from C-H morphologies with $\epsilon = 1.6 \times 10^{-5}$ and thus $\delta_{\mathrm{CH}} \approx 3.3$ nm but different values of σ_{CH} ranging from 0.1 to 3.0 as indicated.

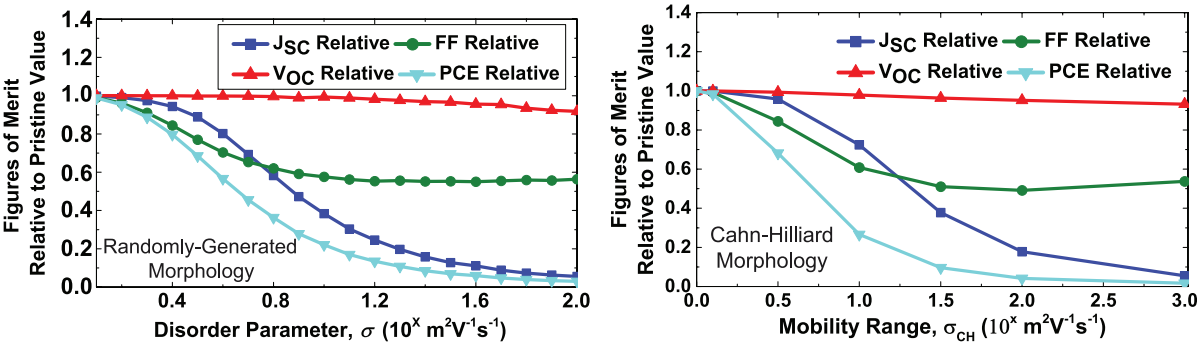

(a) (b)

Figure 3.4: Relevant figures of merit of ensemble-averaged J–V characteristics for the series of replicas presented in Fig. 3 as a fraction of a pristine device's taken as (a) the disorder parameter for the random mobility distribution method, σ, is increased from 0.1 to 2.0, and (b) the disorder parameter σ_{CH} for the Cahn-Hillard morphology method is varied from 0.1 to 3.0.

3.3.1.1 The Effects of Spatial Mobility Disorder on J_{SC} and *FF*

The large decrease in device performance with increasing disorder arises from the lower limits of the possible device figures of merit in the case of extreme disorder. The lower limit for J_{SC} is clearly zero, and we see the device current approaching this as σ or σ_{CH} increases. This results from the fact that for high values of the disorder parameter, a significant fraction of the replicas have occasional domains of exceptionally low mobility ($\sim 10^{-7}$ to 10^{-8} cm^2 V^{-1} s^{-1}). These domains are so limiting to charge transport that charges cannot be extracted before they inevitably recombine, resulting in essentially zero net photocurrent. The lower limit for the *FF* with increasing disorder appears to be roughly 0.25. At this point, the average *J*–*V* characteristic of the devices ceases to be diodic and instead resembles a resistor with a nearly linear *J*–*V* relationship. This is because for high values of the disorder parameter, the presence of low mobility domains dominates the overall charge transport, resulting in devices with low conductivity and thus high resistivity.

To better elucidate the way spatial disorder impacts the performance of an ensemble of devices, in Fig. 3.5 we present histograms of the figures of merits of an ensemble of devices whose mobility profiles were generated via the random sampling method (we present the corresponding histograms for the C-H method in Appendix A). Because the random sampling and Cahn-Hillard methods produce qualitatively similar results and lead to the same conclusions, in the sections that follow we show only the data for the random sampling method in the main text without loss of generality. Figure 3.5 shows that both the J_{SC} and the *FF* exhibit skewed distributions that cause their means to be lower than their medians. This skewness is perhaps not surprising given that there is an effective upper bound to both the J_{SC} and the *FF*. The fill factor has traditionally been seen as measure of how beneficial the morphology of the device is to charge transport, and clearly the pristine morphology exhibits the highest possible *FF* for the chosen set of D-D parameters. Thus, inserting regions of low mobility within a pristine material lowers the fill factor. Conversely, it is hard to imagine that inserting occasional regions of relatively high mobility could drastically improve charge transport if there were low mobility domains elsewhere in the transport

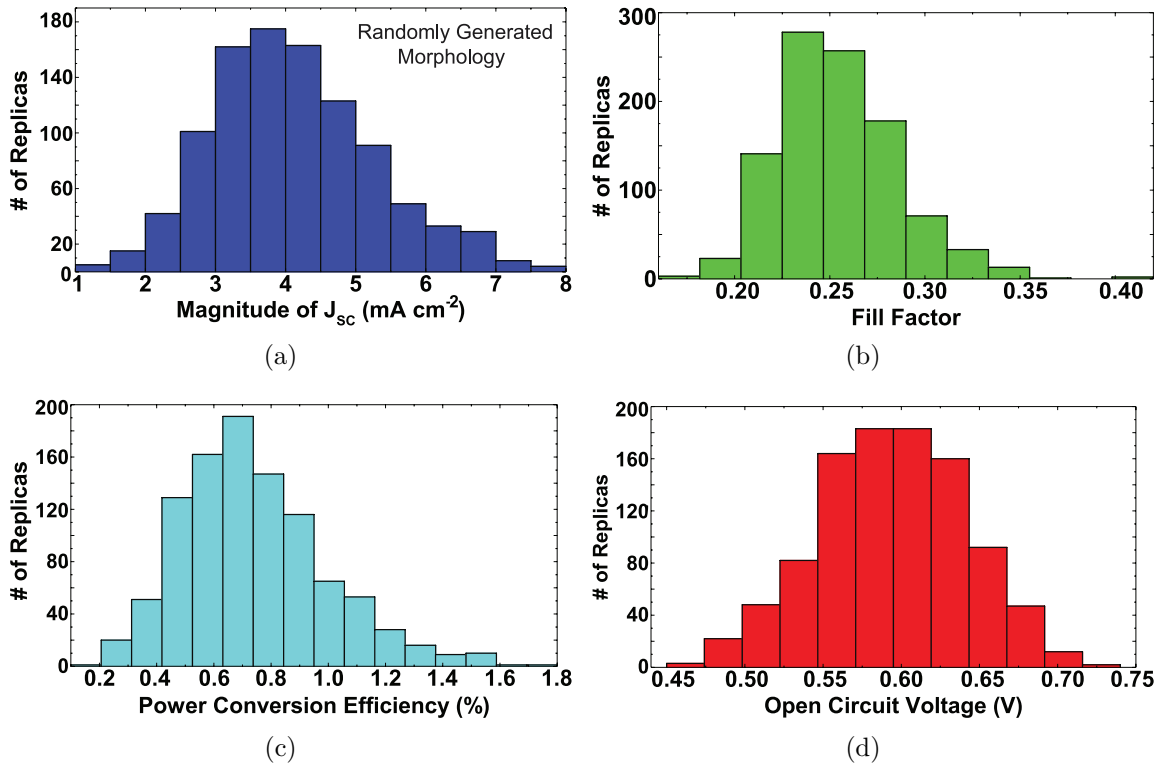

Figure 3.5: Histograms illustrating the distribution of: (a) the short-circuit current, (b) the fill factor, (c) the power conversion efficiency, and (d) the open circuit voltage for individual device replicas sampled from the randomly-generated spatial mobility distribution ensemble of Fig. 3.1a ($\mu_0 = -8.0$, $\sigma = 0.7$, $\delta = 3$ nm); see Appendix A for the corresponding plots for spatially-disordered mobility replicas generated by the C-H method.

pathway. These same arguments also hold for the J_{SC}, explaining why the J_{SC} and FF have an effective upper bound (corresponding to a pristine device with uniform carrier mobility), which results in a skewed distribution that biases the average towards lower values.

Figure 3.6 summarizes the behavior of the skewness of the J_{SC} (dark blue curve), FF (green curve) and power conversion efficiency (PCE, light blue curve) distributions for different randomly-generated mobility ensembles with changing disorder parameter (σ). The skewness of a population can be estimated from a sample of the population by:

$$\gamma = \frac{m_3}{s^3} = \frac{\frac{1}{n}\sum_{i=1}^{n}(x_i - \bar{x})^3}{\left[\frac{1}{n-1}\sum_{i=1}^{n}(x - \bar{x})^2\right]^{3/2}} \tag{3.10}$$

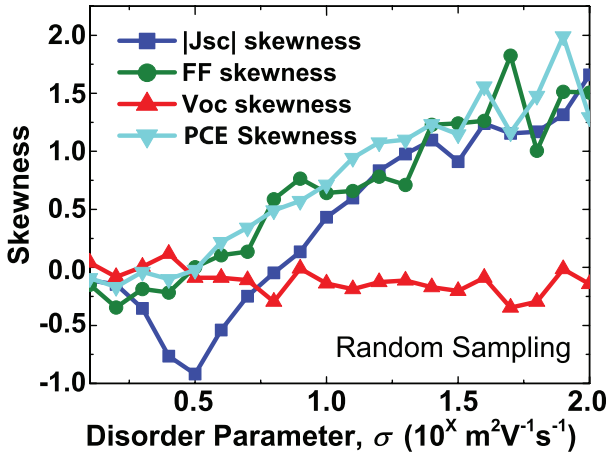

Figure 3.6: Skewness of device replicas' figures of merit as a function of the disorder parameter, σ (same randomly-generated mobility replicas whose individual properties and ensemble-averaged behavior are summarized in Figs. 3.2 through 3.5).

where m_3 is the sample third central moment and s is the sample standard deviation of the population of values. We emphasize that this standard deviation corresponds to the sample of the values of the device figures of merit (J_{SC}, FF, and V_{OC}) and not the standard deviation of the mobility distribution from which the sample of replica devices is generated. For lower values of the disorder parameter σ, both the J_{SC} and FF distributions are negatively skewed; that is, they have a tail towards lower values and their mean is less than their median. At higher values of σ, the direction of this tail reverses and the distributions become positively skewed. This reversal in skewness results from a change in the replicas' performance from being upper-bound dominated to lower-bound dominated. For both the short-circuit current and fill factor, the lower bound corresponds to zero current flowing or the 0.25 effectively linear FF in the device as a result of the presence of low mobility regions in the average mobility profile.

3.3.1.2 The Effects of Spatial Mobility Disorder on V_{OC}

Figures 3.5 and 3.6 also examine the skewness of the distribution of open circuit voltages for the randomly-generated spatially-disordered mobility replicas (red curve, bars), which is expected to depend primarily on the nature of carrier recombination [159]. For all values of σ that we explored, the V_{OC} distribution has a skewness of nearly zero and thus follows a

nearly normal distribution. The normal distribution of V_{OC} results from the fact that we are utilizing a Langevin recombination mechanism of the form:

$$R(x) = \frac{q}{\epsilon_r \epsilon_0}[\mu_n(x) + \mu_p(x)] \cdot n(x) \cdot p(x) \tag{3.11}$$

which depends directly on the mobility. Despite the explicitly linear dependence in Eq. (3.11), we note that recombination is actually nonlinearly dependent on mobility since the electron and hole densities are implicitly functions of their respective carrier mobilities. Thus, decreasing the mobility for either carrier in a particular spatial region leads to a locally diminished recombination rate, and therefore a lower recombination term in Eq. (3.3). This same low mobility, however, also leads to a buildup of charge in that spatial region, which leads to a locally increased recombination rate.

This subtle balance between carrier build-up and carrier recombination can result in replicas with either enhanced recombination or lowered recombination, which by the central limit theorem we expect to be normally distributed. This results in an ensemble with approximately the same average amount of recombination per device as a non-disordered device. Since V_{OC} occurs at the voltage for which the recombination rate equals the generation rate (and since the generation rate is constant for all replicas), it follows that ensemble-averaged V_{OC} should be roughly the same as that of a non-disordered device. As a result, the average V_{OC} is relatively impervious to increasing spatial mobility disorder. This finding is in stark contrast to what happens in the case of energetic disorder, where previous studies have found that V_{OC} decreases with increasing energetic disorder [16]. The D-D simulations we present here consider only structural disorder, so we can conclude that V_{OC} is not affected by structural disorder, and should be thought of as susceptible only to the energetic disorder that inherently accompanies structural disorder and the way this energetic disorder affects the recombination kinetics. A side effect of our choice of a Langevin recombination mechanism is that there may be excessive recombination. The assumption of a Langevin recombination mechanism has been shown to over estimate the recombination rate of OPV devices [137, 91, 96]. As such, drift-diffusion studies which employ such a mechanism typically in-

clude a recombination reduction factor, which can range from 10^{-1} to 10^{-3}[42, 22]. Our simulations employ a relatively mild reduction factor of 10^{-1}, which might result in excess recombination and diminished fill factors. It is possible that utilizing a stronger recombination reduction factor would allow a simulated device to possess greater structural disorder (that is, a larger value of σ) before manifesting a comparable degree of performance degradation as what we have simulated in this work. Still, the general conclusion of structural disorder's deleterious effects on device performance should be unchanged, and may simply manifest to a lesser degree.

3.3.2 The Effects of the Spatial Disorder Length Scale on OPV Device Performance

We next turn our investigation to how the length scale of spatial disorder affects device performance. X-ray diffraction and various microscopy measurements have indicated that the polymers and fullerenes in a BHJ phase segregate into domains with sizes on the order of several nanometers, with amorphous and potentially intermixed regions surrounding the domains [193, 177, 117, 38, 187]. To investigate the effects of the phase-separation (and thus the spatial disorder) length scale on device performance, we varied the size of the mobility regions in our ensembles from 2 nm to 20 nm. We do not consider disorder length scales below 2 nm since smaller length scales would correspond to the diameter of single fullerene molecules, thus representing a lower bound to the morphological granularity in a real device [139].

Figure 3.7 illustrates the effect of changing the simulated domain feature size δ for the randomly-generated mobility profiles on the ensemble-averaged figures of merit; as above, these are presented as a fraction of the figure of merit for a pristine device with no structural disorder. (We note that tuning the size scale of the spatial disorder is less direct with the C-H method, as the average length scale δ_{CH} depends in a non-linear way on the ϵ parameter in Eq. (3.7); see Appendix Afor details). As we saw above for the degree of disorder, V_{OC} is relatively unaffected by the introduction of structural features, and has nearly the same

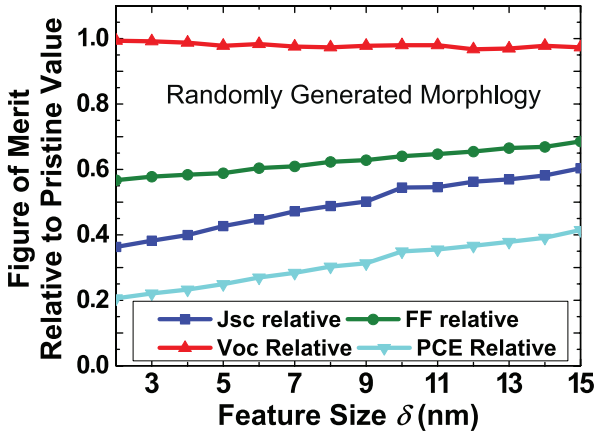

Figure 3.7: Relevant figures of merit for the ensemble averaged J–V characteristics presented in Fig. 3.3a as a fraction of the pristine device's but as the spatial feature size, δ, in the randomly generated profile ensemble is increased from 2 to 15 nm.

average value for all spatially-disordered length scales relative to a non-disordered, pristine device. In contrast, both the J_{SC} and the FF are negatively impacted by the inclusion of discrete mobility regions, and they are more impacted the smaller the features become. Clearly, the fact that real OPV devices are designed to have BHJs with structure on ∼10 nm length scales reinforces the idea that structural disorder is too important to be overlooked in D-D modeling of OPV devices.

To further examine the effects of structural disorder on device performance, we also simulated an ensemble of devices characterized by $\mu_0 = -8.0$, $\sigma = 0.7$, and $\delta = d = 100$ nm, the entire device thickness. An ensemble characterized by these parameters results in individual mobility profiles that have a single, uniform value for their mobility. Thus each device replica will have a have a randomly assigned mobility but no spatial disorder. This ensemble thus decouples the effects of simple mobility disorder (σ) from structural mobility disorder (δ), which is present only in ensembles with structural features that are smaller than the thickness of the device. Figure 3.8 compares the averaged results for this ensemble (red circles, curve) to that of a well-disordered ensemble with $\mu_0 = -8.0$, $\sigma = 0.7$, $\delta = 3$ nm (blue triangles/curve). The data shows that the inclusion of spatially-varying random mobilities diminishes the average performance of the device to a much greater extent than a simple ensemble of random, uniform mobilities. This suggests that the negative impacts

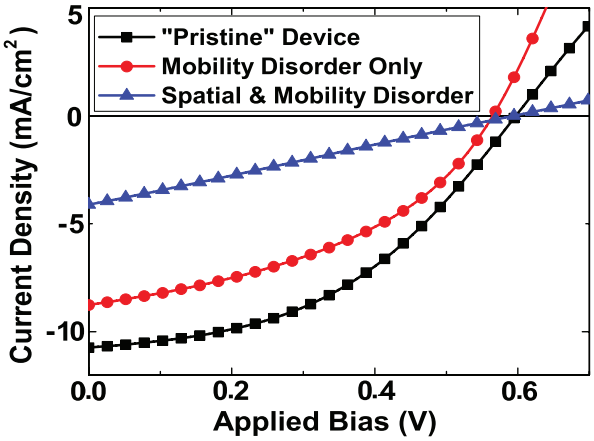

Figure 3.8: J–V curves comparing a randomly-generated structurally-disordered ensemble (blue triangles) with an ensemble of structurally pristine devices with only mobility disorder (red circles; see text for details). Note that although both ensembles' performance diminishes as a result of the inclusion of disorder, the inclusion of structural disorder leads to a much more severe drop in performance.

of structural disorder are not the result of low mobility replicas alone. Rather, it is the fact that spatial disorder includes regions of both high and low mobility that has a significant detrimental effect on device performance. Thus, the reason device performance becomes so diminished at larger values of σ is because the mobility difference between the high and low mobility regions becomes more drastic; in other words, the impact that spatial disorder has on device performance becomes larger.

3.3.3 The Effects of Spatial Disorder on the Shape of J–V Curve

As pointed out above, the introduction of spatial disorder can lead to an S-shaped J–V curve with a very poor *FF*. Using the same D-D modeling approach employed here, we have illustrated in a previous paper how such S-shaped J–V characteristics can be produced by devices that have diminished carrier mobility near an extraction contact [51]. Our previous paper assumed a pristine mobility profile except for a precipitous drop in mobility for electrons near the cathode contact. In the current study, in which mobility profiles are either randomly generated or taken from Cahn-Hilliard calculations, it is easily possible for a replica to have a mobility profile similar to that of our previous work, with low mobility domains near one or both of the extraction contacts.

When we analyzed our individual randomly-generated and C-H mobility profiles, we found that those with a calculated S-shaped J–V curve were indeed almost all characterized by a region of low mobility near one of the extraction contacts. Of particular note, not all of these replicas had the low mobility region contiguous with the extraction contact; instead, in several instances of replicas with S-shaped J–V curves, the low mobility regions were up to 20 nm away from the contact. Of course, Fig. 3.2 shows that the number of replicas that result in S-shaped J–V curves were not sufficient to cause the ensemble-averaged performance to deviate terribly far from typical diodic behavior. However, it is reasonable to assume that if a significant number of replicas were characterized by diminished mobility near an extraction contact, the resulting ensemble averaged J–V characteristic would exhibit an overall S-curve. Thus, the apparently random occurrence of S-curves in experimental devices is dependent on an ensemble morphology that results in poor mobility for a carrier near its extraction contact: S-curves occur when there is a particular problem maintaining mobility near the extraction contact (e.g. via undesirable vertical phase separation), or when the inherent structural disorder in an OPV device happens to leave low mobility regions near the contacts along the majority of the effectively 1-D conduction pathways traversed by the carriers in a particular BHJ geometry.

3.4 Conclusions

In this work, we have used drift-diffusion modeling to examine the effects of structural disorder on the performance of BHJ organic photovoltaic devices. We argued that it is possible to study the effects of 3-D spatial disorder in an OPV device via an ensemble average of 1-D drift-diffusion models. This is because photogenerated carriers in real 3-D devices must traverse a relatively small number of effectively 1-D tortuous, high-conductivity paths to reach the device electrodes. As these carriers encounter grain boundaries, dead-ends or cul-de-sacs along their journey, they effectively lose mobility in the direction of the bulk current. Our approach to accounting for the effects of this disorder involves modeling many replica pathways with mobility profiles either randomly generated from an ensemble mobility

distribution or generated via Cahn-Hilliard modeling. Using this approach, we investigated how the range of mobilities sampled and the size of typical mobility features affected the overall (ensemble-average) device performance.

Based on looking at averages and distributions of 1-D device models with different disorder parameters, we have shown that the short-circuit current and fill factor are negatively affected by the inclusion of structural disorder, but the open circuit voltage is nearly impervious to disorder's debilitating effects. This non-dependence of the open circuit voltage on structural disorder stands in strong contrast to energetic disorder, which has been shown to have a profound detrimental effect on V_{OC} [16]. The strong dependence of the J_{SC} and the FF on structural disorder results from the fact that these figures of merit have effective lower and upper limits for particular mobility profiles, thus forcing an asymmetry in the ensemble that is averaged to simulate the device performance. We also have found that the inclusion of structural disorder is imperative if the OPV architecture in question has feature sizes of a few nm, which is indeed the case for nearly every experimental BHJ device. Finally, we found that no matter how the individual spatially-varying mobility profiles were generated, the results we obtained were the same, indicating that all off the effects discussed above are universal features of spatial disorder and are not dependent on the microscopic details.

As previously discussed, our method for approximating structural disorder is still limited by 1-D charge transport. We are thus missing some of the correlated distribution of charge conducting materials present in a true 3-D BHJ architecture. We hope to further refine our modeling of structural disorder by eventually extending our simulations to higher-dimensionality mobility profiles that include carriers' ability conduct perpendicularly to bulk current flow. We also plan to couple spatial disorder with energetic disorder to better understand the interplay of these two different types of disorder on BHJ device performance. Until such subsequent drift-diffusion studies are carried out, we believe that this 1-D study and analysis provide strong evidence that structural disorder is of paramount consideration for the modeling and development of OPV devices.

CHAPTER 4

Do Organic Photovoltaics Really Need a Mixed Phase? Drift-Diffusion Studies of the Effect of Bulk Heterojunction Compositional Morpholog on Optimum Device Performance

4.1 Introduction

In recent years, photovoltaic devices based on organic materials, referred to as OPVs, have made major gains in their efficiency. Single-junction OPVs have surpassed 10% power conversion efficiency (PCE)[27] and multi-junction, tandem devices have achieved up to 12%.[192] The majority of organic photovoltaic devices are based on a binary blend of a semiconducting polymer and a fullerene derivative. The polymer serves as the light absorber, producing excitons. To split the excitons into free carriers and generate electrical current, such polymers are paired with an electron acceptor, typically a fullerene derivative. These two materials are usually blended together and processed into a ∼100 nm thick film that is layered between two electrodes. The charge carriers then migrate to their respective electrodes by traveling through pathways constructed from their preferred conducting molecules (electrons through the fullerene and holes through the polymer). Efficient charge transport is contingent upon the two conducting materials forming a bicontinuous network so that the charges may move through the device unimpeded. This mix of donor and acceptor materials within the active layer of the OPV device to facilitate both exciton separation and subsequent charge transport is known as a bulk heterojunction (BHJ).[100, 187, 19]

The way in which excitons are split and carriers are transported in a BHJ makes the

performance of OPV devices highly sensitive to the kinetics of how the active organic layer is processed.[184, 187, 149] Because charge carriers travel selectively through the electron donor and acceptor molecules, it is evident that the structural details of an OPV device's internal morphology have an immediate effect on charge transport and thus a device's photovoltaic performance. Further complicating the matter is that the binary component blend used in BHJs results in an active layer with three distinct compositional phases: pure polymer domains, pure fullerene domains, and an amorphous, mixed-composition, interfacial domain that must lie between the pure component domains. There is debate within the OPV community about how the relative sizes of these three domains and the way they are distributed affect OPV device performance. In particular, some have argued that the mixed-composition regime is crucial to OPV device operation, since charge generation occurs most prevalently near the interface between donor and acceptor molecules.[73, 21, 72] Insufficient fullerene intercalation into amorphous polymer domains can result in morphological electron traps, emphasizing the need for a sufficiently intermixed region in the BHJ.[12] Conversely, excessive mixing between fullerene and polymer can result in higher rates of charge recombination, which can lower device performance.[175] Moreover, excitons generated in BHJ devices typically have diffusion lengths of $\sim$10 nm, which is comparable to the average domain size of many polymer/fullerene BHJ devices.[20, 73] Thus, it is not immediately clear to what degree the presence of a mixed-composition domain is beneficial or detrimental to optimum OPV operation.

There are two main reasons why it is difficult to determine if a mixed, amorphous phase is necessary for OPV operation, and if so, how much is needed and how it should be distributed relative to the pure component phases. First, there is no easy experimental method for controlling the relative amounts or spatial distribution of different phases in an OPV active layer because the morphology is determined primarily by the kinetics of how the film is processed.[149, 100] This kinetic sensitivity means that none of the experimental "knobs" that can be tuned (e.g., the use of solvent additives during spin-coating[188], post-treatment via solvent[101] or thermal annealing[83], etc.) can be used to controllably change the relative amounts of phase separation and/or mixed-phase region in an active layer made from a given

set of materials. Second, morphological characterization of the different organic components in an OPVs via electron microscopy is problematic, primarily due to the low contrast between typical OPV materials. Only a few papers have attempted to actually quantify the relative amounts of each single-component phase and the mixed-phase,[186, 28, 129] and then only for a few selected configurations of a very limited set of materials.

All of these complications have hampered experimental efforts to probe the effects of OPV morphology and the presence or absence of a mixed-phase on device performance. Thus, in this paper, we utilize semiconductor device modeling to address this question, focusing our efforts on the well-known drift-diffusion (D-D) model.[173, 74, 116] Several groups have used the D-D approach to study the effects of morphology and morphological disorder on OPV performance.[16, 87, 141] There are actually two types of disorder that, although interrelated, can affect OPV device performance in different ways: energetic disorder, which results from twists and kinks within the polymer chains that produce different energetics for different sites in the active layer film, and structural disorder, which results from the tortuosity of the bicontinuous network that can lead to "dead-ends" and other features that are non-optimal for carrier transport. Many studies have examined the effects of energetic disorder on OPV performance, usually assuming a Gaussian distribution of energetic states and/or an exponential tail of trap states in 1-D drift-diffusion simulations.[16, 87] Other groups have focused on the effects of structural disorder by performing 2-D drift-diffusion simulations to simulate the effects of phase separation and component distribution on device performance[140, 122]; we also have presented a 1-D method for examining structural disorder based on D-D simulations of ensembles of 1-D devices with position-dependent mobility profiles.[52]

In this study, we present a set of 2-D drift-diffusion simulations specifically designed to probe the effects of the presence of a controllably varied mixed-composition, interfacial phase on device performance. We begin by utilizing morphologies generated by Cahn-Hilliard (C-H) modeling of binary fluid phase separation, as has been employed successfully in previous 2-D D-D modeling studies of OPVs.[140, 141] The C-H morphologies allow us to tune the component domain sizes with a single parameter, and we then introduce an interfacial

mixed region between the pure component regions by smoothing the binary morphology in a continuous, controllable fashion. To verify that the conclusions drawn from these artificial morphologies also apply to real BHJ morphologies, we also utilize a single empirical morphology obtained via high-angle annular dark-field scanning transmission electron microscopy (HAADF-STEM). The phase-domains for this morphology (pure donor, pure acceptor, and mixed-phase) have been previously characterized.[185] We then map charge carrier mobilities to both the C-H and HAADF-STEM generated morphologies, allowing us to probe the effects of having differing amounts of mixed-composition, interfacial domains present in BHJ OPV devices at various average morphological feature sizes. We find that the presence of interfacial mixed regions can be either beneficial or deleterious to OPV device performance depending on the average feature size and the amount of mixed-phase introduced. Analysis of our simulation data indicates that introducing a mixed-phase can first improve device performance by reducing the number of morphological traps (i.e., dead-ends or "cul-de-sacs") and reducing the tortuosity of conduction pathways. In some cases, the introduction of a mixed-phase can even create new conduction pathways by connecting previously disjointed conduction domains. However, excessive mixing actually reduces device performance by degrading conduction pathways, resulting poorer charge transport and the loss of carriers to recombination. The point at which mixing becomes deleterious, rather than beneficial, to charge transport differs depending on the average feature size of the simulated morphology and other morphological variations. This all results in non-monotonic trends for device performance as a function of mixing and domain size. In an experimental setting, different donor/acceptor blends exhibit distinct domain size distributions and degrees of mixing. The non-monotonic effects of the mixed-phase on device performance may thus explain why it is so laboriously difficult to optimize new donor/acceptor pairings and why OPV devices are so sensitive to processing conditions and performance degradation over time.

4.2 Computational Methods

4.2.1 Drift Diffusion Model

For this work, we perform our device simulations using the drift-diffusion model of electrical current, in which the electron and hole current densities (J_n, J_p) are assumed to take the functional form:[162]

$$J_n = -qn\mu_n \nabla V + kT\mu_n \nabla n \tag{4.1}$$

$$J_p = -qp\mu_p \nabla V - kT\mu_p \nabla p \tag{4.2}$$

where q is the fundamental charge, n and p refer to the electron and hole densities, V is the electrostatic potential, and μ_n and μ_p refer to the mobility of electrons and holes, respectively. [90] In order to simulate a working device, one must solve the density continuity equations for both carriers:

$$\frac{\partial n}{\partial t} = \frac{1}{q}\nabla \cdot J_n - R + G \tag{4.3}$$

$$\frac{\partial p}{\partial t} = -\frac{1}{q}\nabla \cdot J_p - R + G \tag{4.4}$$

where R is the recombination rate and G is the generation rate of electrons and holes. Because the literature consensus is that recombination events in OPV devices are trap-assisted processes, we follow the approach of previous groups and use the Shockley-Read-Hall functional form to represent recombination with an exponential distribution of trap states.[87, 16] To appropriately account for the thin-film interference effects that occur in normal OPV device layer structures, we use a transfer matrix formalism[135] to calculate the absorption profile and also allow for the carrier generation profile to be morphology dependent, as discussed below in Section 4.2.2.3.

Once generated, the carrier densities must also satisfy the Poisson equation:

$$\nabla^2 V = \frac{q}{\epsilon_r \epsilon_0}(n - p) \tag{4.5}$$

where V is the electrostatic potential. This additional requirement means that all of the above equations are inherently coupled. The set of Eqs. (4.1)-(4.5) forms the basis of the D-D model.

We used the Gummel method to decouple the above set of partial differential equations and solved them in an iterative manner.[58] Equations (4.3)-(4.5) are appropriately discretized and solved on 2-D finite difference mesh.[147, 152, 162] Boundary conditions at the semiconductor-metal contacts were treated as Dirichlet type, meaning the values of the carrier densities and potential were predetermined. For the boundary conditions for the carrier densities at the electrodes, we assumed thermionic injection of free carriers from the metals into the organic semiconducting materials of the active layer.[150] For the Poisson equation's boundary conditions, we assumed that the potential drop across the device was equal to the device's built-in voltage, V_{BI}. The lateral boundary conditions were treated as Neumann type, meaning the gradients of n, p and V were predetermined. We set the gradients of these variables to zero at the sides of the device, since there should not be excessive lateral drift or diffusion current for reasonably wide active areas like those explored here. Collectively, the boundary conditions for our D-D simulations were:

$$n(x,0) = N_{\mathrm{C}} \exp(-\frac{\Phi_{\mathrm{B,ano}}}{kT}) \tag{4.6}$$

$$n(x,d) = N_{\mathrm{C}} \exp(-\frac{\Phi_{\mathrm{B,cat}}}{kT}) \tag{4.7}$$

$$p(x,0) = N_{\mathrm{V}} \exp(-\frac{E_{\mathrm{g}} - \Phi_{\mathrm{B,ano}}}{kT}) \tag{4.8}$$

$$p(x,d) = N_{\mathrm{V}} \exp(-\frac{E_{\mathrm{g}} - \Phi_{\mathrm{B,cat}}}{kT}) \tag{4.9}$$

$$V(x,0) = 0 \tag{4.10}$$

$$V(x,d) = V_{\mathrm{BI}} \tag{4.11}$$

$$\frac{\partial n(0,y)}{\partial x} = \frac{\partial n(w,y)}{\partial x} = 0 \tag{4.12}$$

$$\frac{\partial p(0,y)}{\partial x} = \frac{\partial p(w,y)}{\partial x} = 0 \tag{4.13}$$

$$\frac{\partial V(0,y)}{\partial x} = \frac{\partial V(w,y)}{\partial x} = 0 \tag{4.14}$$

where $\Phi_{\mathrm{B,ano/cat}}$ are the Schottky barriers at the anode/cathode, $N_{C/V}$ are the density of chargeable sites/vacancies for electrons/holes, E_{g} is the effective bandgap represented by the offset between the polymer's HOMO and the fullerene's LUMO, and d and w refer to the depth and width of simulated device. The dimensions of most of our simulated devices were chosen as 100 nm deep by 300 nm wide, an active area large enough to capture the majority of morphological effects while still being computationally tractable. We chose additional simulation parameters that are comparable to those previously used in the literature.[75, 87] All the parameters pertinent to our calculations are collected in Table 4.1.

4.2.2 Mapping Morphologies to a D-D OPV Device Model

4.2.2.1 Cahn-Hilliard Generated Morphologies

There has been relatively limited direct nm-scale compositional mapping of OPV active layers due to the limited contrast between typical donor and acceptor components.[186, 28, 129] As such, the number of experimental morphologies available to map and simulate is noncomprehensive. To examine as many permutations of pure component and mixed-composition

Parameter	Symbol	Value
Active Layer Depth	d	100 nm
Active Layer Width	w	300 nm
Relative Permittivity	ϵ_r	3.5
Schottky Injection Barriers	ϕ_n, ϕ_p	0.4 eV, 0.1 eV
Electron Mobility in Acceptor	$\mu_{n,A}$	10^{-7} m^2 V^{-1} s^{-1}
Electron Mobility in Donor	$\mu_{n,D}$	10^{-12} m^2 V^{-1} s^{-1}
Hole Mobility in Acceptor	$\mu_{p,A}$	10^{-12} m^2 V^{-1} s^{-1}
Hole Mobility in Donor	$\mu_{p,D}$	10^{-8} m^2 V^{-1} s^{-1}
Built-in Voltage	V_{BI}	0.7 V
Density of Trap States	$N_{\mathrm{C}}, N_{\mathrm{V}}$	1×10^{20} cm^{-3}
Urbach Energy	E_{UC},E_{UV}	40 meV
Capture Rate Coefficient	$\beta_{n,p}^{+,-,0}$	1×10^{13} cm^{-3} s^{-1}
Temperature	T	298 K
Band Gap	E_g	1.2 eV

Table 4.1: Boundary conditions and values of other parameters used for all the D-D simulations presented in this work, except where otherwise noted in the text.

domain size as possible, we chose to start with a series of computer generated, binary component morphologies (i.e., containing only pure phases and no mixed-phase) of varying average domain size and then introduced a mixed-phase, interfacial domain of a controllably varying width. We followed the approach of several previous groups and generated an initial series of model morphologies based on the spontaneous phase separation of a binary fluid mixture. This involves solving the Cahn-Hilliard equation:

$$\frac{\partial C}{\partial t} = D\nabla^2(C^3 - C - \epsilon\nabla^2 C) \tag{4.15}$$

where C is the spatial composition of the fluid mixture that ranges from one pure component to the other ($C(x, y) \in [0, 1]$). In this equation, D is the diffusivity and ϵ is the interfacial interaction energy between the two components. Since our primary interest in Cahn-Hilliard morphologies is the semi-random distribution of phases at differing length scales, we set $D = 1$ and instead only varied the relative interaction energy. Since the interaction energy determines the average domain size of the resulting morphologies, this single parameter allowed us to simulate bulk heterojunction morphologies with a controllably varying feature size. We employed David Eyre's linearly stabilized Cahn-Hilliard integration scheme[50, 17]

to solve the Cahn-Hilliard equation on a 2-D grid, an approach that has previously been applied to generate polymer-fullerene BHJ morphologies.[140, 141]

Although other Cahn-Hilliard-based studies have investigated morphology characteristics such as average feature size[92], annealing time (represented by Cahn-Hilliard integration time)[141], and tortuosity on OPV device performance,[24] for this study, we are primarily interested in the effects of the amorphous, mixed-composition interfacial regions and how such regions may be important for BHJs to function. Thus, we chose to start with a few, base morphologies that have feature sizes of approximately 4, 8, 10, 12, and 15 nm (we determine the average feature size via examination of pair-pair distribution functions for each morphology).[108] To this end, we simulated all our morphologies using identical starting parameters, listed in Table 4.2, except for the interaction energy, ϵ that determines the average domain size.

It is worth noting that the morphologies generated by Cahn-Hilliard simulation necessarily have an interfacial width that is related to the domain size. However, in real BHJ's, the mechanics of local phase separation are more complicated, since most BHJ phase separation is driven by polymer crystallization and/or agglomeration of the fullerene, which may not be well represented by the simple separation of immiscible fluids. Thus, the interfacial regions generated in Cahn-Hilliard morphologies may not correspond well with the mixed regions found in real BHJs with a comparable average feature size. To account for this and to gain more control over our simulated mixed interfacial regions, we started by completely binarizing our Cahn-Hilliard morphologies them (i.e., rounding C to either 0 or 1 at every point in space), thus generating morphologies with only pure-component domains. We then re-introduced mixed regions by "blending" the pure domains at the interface by successively applying Gaussian smoothing operations. This results in a morphology that varies from 0 to 1 with a smooth interface (of varying and controlled width) between the pure domains. In this way, we can explore the OPV performance of active layers that have amorphous interfacial regions of varying dimension for BHJs with different active-layer feature sizes. An example of a binarized Cahn-Hilliard morphology and the effects of our Gaussian smoothing procedure on this morphology are shown below in Figure 4.2(a)-(c).

We note that this method of Gaussian smoothing to "mix" the pure phases only introduces a mixed-phase at the interface between pure regions. The amount of mixed region introduced by a smoothing operation is thus dependent on the fraction of the device that can be characterized as an interface. Because the initial C-H morphologies that we explored have different feature sizes, they also have different amounts of interface in their initial compositions, so that applying a single Gaussian smoothing operation to the different morphologies does not introduce the same amount of mixed-phase. In order to easily compare different feature-sized morphologies, we instead choose to use the standard deviation, σ, of the morphologies' compositions as a way to quantify the degree of mixing. In the completely unmixed morphologies, all mesh points have a composition value of 0 or 1, since we only have pure regions. Since the mole fraction ratio of donor to acceptor is 0.5, the standard deviation in composition of the initial morphology is 0.5. In contrast, if we had constructed a perfectly blended, homogeneous morphology, all mesh points should have the same compositional value of 0.5, leading to a standard deviation of exactly 0. The standard deviation values between these two limits thus provide a measure of the fraction of the morphology that has been mixed, as quoted in the caption to Fig. 4.2. Explicitly, the fraction of the device that is mixed, f_{mixed} is related to the standard deviation of the devices composition, σ, by:

$$f_{\text{mixed}} = 1 - 2 \times \sigma \tag{4.16}$$

4.2.2.2 Empirical (HAADF-STEM) Morphology

As previously discussed, it is unclear how representative our Cahn-Hilliard generated morphologies are of actual BHJ morphologies. The Cahn-Hilliard formalism is an idealized model of binary fluid phase separation. However, the phase separation kinetics of typical OPV donor/acceptor blends is significantly more complicated.[184, 187, 149, 100] Therefore, in addition to the bevy of artificial morphologies simulated, we also simulated an empirical morphology which has already been characterized in terms of its compositional domain distribution.[186] This morphology, presented below in Fig. 4.3(a), was obtained by high-angle annular dark-field scanning transmission electron microscopy (HAADF-STEM) and

represents the compositional density profile of donor and acceptor materials, specifically P3HT and the endohedral metallofullerene 1-[3-(2-ethyl)hexoxy carbonyl]propyl-1-phenyl-Lu3N@C80 (Lu3N@C80-PCBEH). In their analysis, the authors of Ref. [186] were able to specifically characterize the experimentally observed compositional domains as pure donor, pure acceptor, or mixed. For our simulations, we represented the local composition $C(x, y)$ with 1 corresponding to pure donor, 0 to pure acceptor, and 0.5 to the mixed region. For this particular 2-D slice of this particular experimental morphology, the mixed component domain accounted for $\sim$16% of the device's active area, using our above method for measuring the degree of mixing. We then utilized this compositional data to map out the charge carrier generation profile, which we set to occur only in the mixed-component region and which we based on the calculated light absorption profile determined by solving a transfer matrix formalism to account for thin-film interference effects, as described further in Sec. 4.2.2.4. We also used the local composition to determine the local charge carrier mobilities, as discussed in more detail in Sec. 4.2.2.3

4.2.2.3 Mapping Morphology to Simulated Device Parameters

With our set of morphologies in hand, our next step was to incorporate these morphologies into our drift-diffusion simulator. The device parameters that should be most directly affected by the compositional morphology are the mobilities and generation rate of charge carriers. The two organic components typically used in BHJ solar cells are often charge carrier selective in regards to their mobility. For example, the archetypal OPV polymer poly-3-hexylthiophene (P3HT) possesses a mobility of approximately 10^{-4} cm^2 V^{-1} s^{-1} for holes, but P3HT's electron mobility is many orders of magnitude lower, approximately 10^{-8} cm^2 V^{-1} s^{-1}.[114] Conversely, the archetypal OPV fullerene derivative, PCBM, possesses high electron mobility ($\sim 10^{-3}$ cm^2 V^{-1} s^{-1}), but a much lower hole mobility ($\sim 10^{-8}$ cm^2 V^{-1} s^{-1}).[98]

Given this, in our simulations we chose to map the carrier mobilities from the composition by:

$$-\ln(\mu_n) = \mu_{n,A} + (\mu_{n,D} - \mu_{n,A}) \cdot C_A(x, y) \tag{4.17}$$

where μ_n is the electron mobility at spatial position (x, y), $\mu_{n,A/D}$ is the mobility of electrons moving among a network of pure acceptor/donor molecules, and $C_A(x, y)$ is the compositional profile of the active layer. We add the additional subscript to the compositional morphology term generated from Eq. (4.15) to make explicit that we define $C_A(x, y) = 1$ as corresponding to pure electron acceptor material (i.e., the fullerene derivative). We define the spatially-varying hole mobility in a similar fashion. With this functional form, the carrier mobility can vary several orders of magnitude at different spatial positions, as determined by the local composition. We chose this functional form specifically so that the mixed, interfacial region possesses a moderate degree of carrier mobility, which is at an order of magnitude somewhere in between that of the two pure components. We justify this choice based on the logic that a mixed region should have an appreciable charge carrier mobility due to the presence of the appropriate conducting molecule in that region. However, since these regions also tend to be amorphous and contain the other, non-conducting component, it follows that the mixed region should not be as highly conductive as the pure phase.

It should be noted that there are technically two different approaches for mapping mobilities onto the mixed-phase domains in the interfacial regions: either by first smoothing the compositional morphology and then mapping the charge carrier mobilities (our chosen method), or an alternate method where the mobility mapping is performed first and then the mobility profiles are subsequently smoothed. With the first method, which we chose to implement, the carrier mobilities in the mixed region tend to be over an order of magnitude smaller than those in the pure phases with large fluctuations depending on the exact composition. In contrast, the alternative mapping-before-smoothing approach produces mobilities in the mixed-phase that are all roughly about one-half that in the pure phases with relatively little compositional fluctuations. As the experimental values of carrier mobilities in the mixed-phase are unknown, for the major part of this study, we chose the smoothing-before-mapping approach since this produces mixed-phase mobilities that make the most

physical sense to us. We have, however, explored both approaches for mobility mapping, and examples illustrating how the different approaches yield different device performance trends are given in Appendix B.

4.2.2.4 Transfer Matrix Approach for Calculating Carrier Generation Profiles

To determine the carrier generation profile to be used in our simulations, we began with a transfer matrix calculation using an effective medium approximation to calculate the wavelength-dependent absorption profile through the device. Charge carriers, however, are generated by the absorption of light only if the resultant excitons on the absorbing donor are subsequently split at a donor/acceptor interface. In other words, charge carriers should be generated predominantly in proximity of the interface between the two components of both our experimental and Cahn-Hilliard morphologies. It is well established that excitons have a diffusion length of approximately 5-10 nm in most OPV material blends.[115] Thus, we expect carrier generation to be maximized at the interfaces between the binary phases and to decay in magnitude as we move outward from that interface, so that no carriers are generated at distances $\geq$10 nm from the interface. To account for this in our simulations, we convolve an exponentially decaying profile with a 10-nm decay constant centered on the interfacial boundaries with our transfer matrix profile, resulting in spatially-dependent carrier generation that properly accounts for both morphological and exciton diffusion effects. An example of such a generation profile for a C-H morphology with an average feature size of $\sim$10 nm is presented in Fig. 4.1

4.3 Results and Discussion

4.3.1 Cahn-Hilliard Generated Morphologies

We begin our analysis of the effects of the mixed-composition phase on OPV charge transport by simulating the J–V characteristic of the Cahn-Hilliard generated morphologies by solving Eqs. (4.3)–(4.5) as a function of applied voltage bias (the full J–V characteristics

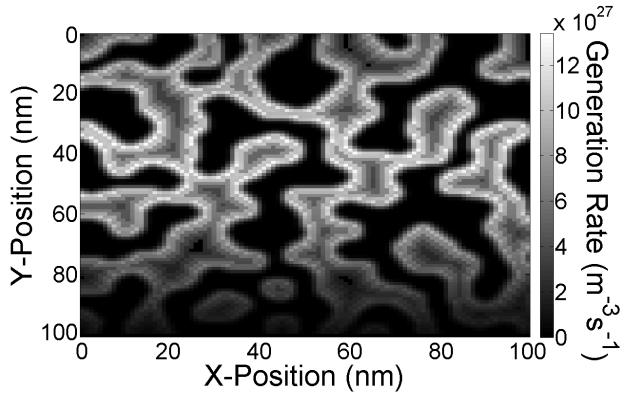

Figure 4.1: An example of a spatially dependent generation rate for a morphology generated by Cahn-Hilliard modeling. By comparison of this image with the morphology images presented in Fig. 4.2, it is clear that charges carriers are only generated in proximity to the interface between donor and acceptor phases.

Parameter	Symbol	Value
Diffusivity	D	1
Simulation Time	$t_{\max}$	1000
Time Step	$\triangle t$	0.5
Interaction Energy	ϵ	0.0018, 0.0023,
		0.0024, 0.0025, 0.0030
Average Domain Size		4 nm, 8 nm
of Generated Morphologies		10 nm, 12 nm, 15 nm

Table 4.2: Boundary conditions and parameters used for the C-H binary fluid simulations, except where otherwise noted in the text. All values serve as unitless parameters for the simulations. The average domain sizes of the morphologies generated with this parameters are given in the last row of this table.

are presented in Appendix B). We present an example of one such morphology in Fig. 4.2. Specifically, the presented images refer to a C-H morphology with an average domain size of ∼10 nm. We present snapshots of the morphology at varying degrees of mixing: first when only pure component domains are present (0% mixing, panel (a)) as well as two levels of Gaussian smoothing that result in 30% (panel (b)) and 70% (panel (c)) mixing of the active layer. The colormap for these images is such that white corresponds to pure acceptor material (i.e., fullerene) and black corresponds to pure donor material (i.e., polymer). The orientation is such that the top of the image corresponds to the transparent anode and the bottom corresponds to the metallic cathode. After this initial morphology has been mapped to mobility and generation profiles, we solved Eqs. (4.3)–(4.5) and simulated the J–V characteristic measurement for each morphology. The steady-state solutions for the electron density, the recombination rate of carriers, and the y-component electron current density (n, R, and $J_{n,y}$) at 0 V applied bias (built-in field only) are also presented in the second, third, and fourth rows of Fig. 4.2, respectively.

Immediately apparent from carrier density plot in Fig. 4.2(d) is how indirect conduction pathways and morphological traps result in significant charge accumulation at various points within the device. We note that the largest regions of charge accumulation are characterized by both high carrier generation (i.e., near the interface between pure domains) and the lack of a direct, continuous conductive pathway between the generation site and the electron extraction cathode (the cathode is located at the bottom of the figure in our representation). Perhaps not surprisingly, these regions of accumulated charge are also localized regions with an increased rate of charge carrier recombination, as presented in Fig. 4.2(g). To further examine the effects of the tortuous BHJ morphology on charge transport, we present the spatially-dependent electron current density, J_n, in Fig. 4.2(j). For the sake of clarity, we only present the y-component (i.e., vertical component) of the electron current density vector(i.e., $J_{n,y}$), as current in the horizontal directions do not contribute appreciably to the overall measured device current. The colormap in this panel is chosen so that white corresponds to electrons flowing down towards the cathode, while black corresponds to electrons flowing upwards towards the anode. Although the device's built-in electric field causes much of

the electron density to drift towards the cathode, the accumulation of charges in the various morphological traps results in significant diffusion current that flows against the built-in field. Thus there is a significant amount of leakage current (loss of charge carriers by recombining with charges at the "wrong" electrode[138]) as electrons leave the device at the anode. The impact of these morphological effects on the C-H morphologies' device performance will discussed in detail in Sec. 4.3.5.

4.3.2 Empirical (HAADF-STEM) Morphology

To validate that our simulations of Cahn-Hilliard generated morphologies are qualitatively representative of an actual BHJ morphology, we also simulated the J–V characteristic of a morphology determined by HAADF-STEM microscopy. We present the same set of observables that were examined for the C-H morphologies (C_A, n, R, and $J_{n,y}$) in Fig. 4.3. The same phenomena observed in the C-H morphologies are evident in the HAADF-STEM morphology. The tortuous charge transport pathways of the morphology result in charge accumulation at various points inside the device, particularly when charges are generated without a direct pathway towards their preferred extraction electrode (again, for electrons, this corresponds the bottom of the device). The accumulation of charge results in increased rates of recombination at localized regions of the device's morphology. We note that there is also significant leakage current of electrons at the anode, as the accumulation of charges and tortuous pathways causes electrons to diffuse to and be extracted at the "wrong" metal contact. All of these phenomena result in a rather poorly performing device with a power conversion efficiency of 0.616%, a result of possessing a J–V characteristic with a J_{SC} of 3.38 mA cm^{-2}, a V_{OC} of 0.642 V, and a FF of 0.409 (See Appendix B for the full J–V characteristic). Unfortunately, there is no experimentally determined J–V characteristic for this morphology, since the film this morphology corresponds to was specifically fabricated to obtain tomographic data, which involved either the removal of or the complete lack of a top metal contact. In other words, while this empirical morphology was meant to represent real BHJ device films, it was *not* a functional OPV device. However, OPV devices fabricated from these same materials typically exhibit much higher device performances than what we

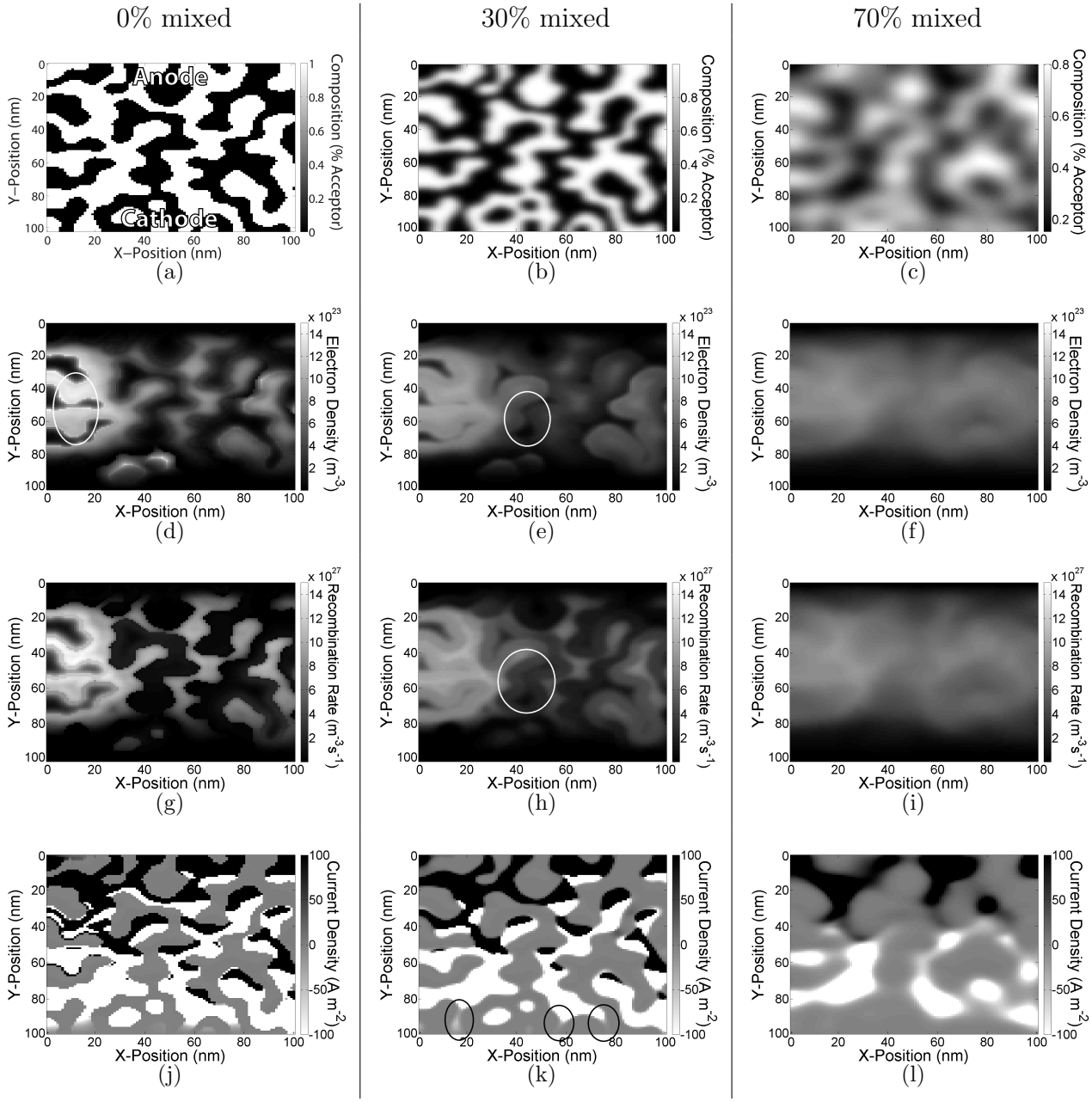

Figure 4.2: Simulation results of OPV devices based on C-H morphologies with a controllably increasing amount of intermixed compositional regions from left (no intermixing) to right (most intermixing). All figures represent the device at short-circuit conditions under simulated AM1.5 illumination. Panels (a)-(c): overall compositional morphology; panels (d)-(f): spatially-dependent electron density; panels (g)-(i): spatially-dependent recombination rate; panels (j)-(l): electron current density profile. Each of these image plots shows a 100 nm $\times$ 100 nm subsection of the entire simulated device. The ITO/PEDOT:PSS anode and the calcium cathode are located at the top and bottom of each plot, respectively. The three columns correspond to devices with 0%, 30%, and 70% of the active area characterized as mixed-phase, respectively.

observe in our simulations.[103] This low performance is likely the result of an unusually coarse (large domain sizes) subsection of the full morphology as well as the fact that we are only considering charge transport in 2-D. In a real 3-D device, there would be additional transport pathways in the z-dimension (which we do not consider) and the morphology would be less restrictive to charge transport. However, the qualitative agreement of the key simulated observables (n, R, and $J_{n,y}$) between the C-H morphologies and the HAADF-STEM morphology suggests that the results and conclusions drawn from our computer generated morphologies are approximately representative of real OPV devices.

4.3.3 Charge Densities and Recombination Rates

With this basic description of the effects of a mixed-composition, interfacial phase on a device's performance in hand, we now examine the effects of introducing increasing amounts of interfacial mixed-phase in more detail. Figure 4.2 shows the spatially-dependent electron density and recombination rate at varying degrees of mixing for our ∼10-nm C-H morphology with the simulated device held at short-circuit conditions under simulated AM1.5G illumination. Panel (d) shows that this morphology, without an interfacial phase present, exhibits relatively large localized regions of charge density. This is because, in the absence of an interfacial region, electrons accumulate at the edges of the acceptor domains as they have difficulty traversing the abrupt boundaries to the more poorly conducting donor domains. The highest accumulations of charge density occur in regions where there are structural dead-ends in the morphology, circled in Fig. 4.2(d). In these regions, electrons are forced to either slowly drift through the pure polymer phase, diffuse against the built-in electric field to find a less resistive pathway, or be lost to recombination. Note that a even when an abrupt interface exists, a certain fraction of the charges can still diffuse into lower-conductivity regions. The excess accumulation of charge at such regions, however, results in higher local recombination rates (panel (g)), so that structural disorder leads to an overall loss of carriers, as has been discussed by others.[32]

In the center panels of Fig. 4.2, we see that when this same morphology is smoothed to

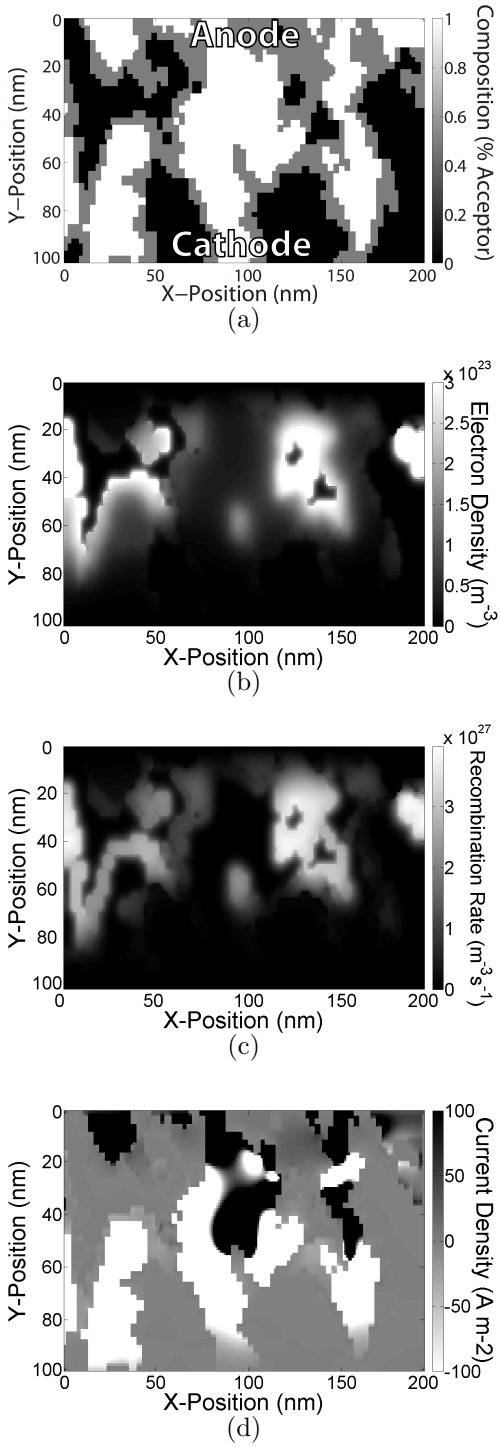

Figure 4.3: Image plots of simulation data for an experimentally-determined (by HAADF-STEM) BHJ morphology.[186] Panels (a)-(d) present the compositional morphology, steady-state electron density, steady-state recombination rate and the y-component (vertical component) of the electron current density vector, respectively, all presented under short-circuit conditions (i.e., 0 V applied bias). The images show the data for a 100 nm $\times$ 200 nm subsection of the full morphology.

become 30% mixed, there is an overall drop in the steady-state charge density. In particular, the charge density is reduced in the dead-end regions that previously had exhibited higher amounts of recombination. Panel (h) shows that the introduction of the mixed-phase also reduces the peak recombination rates. Note that although the average carrier density and recombination rate decrease when the mixed-phase is introduced, there are some regions of the device that actually exhibit an increase in carrier density and local recombination rate (indicated by circled regions of Figs. 4.2(e) and(h)). This trend persists at higher degrees of mixing, as illustrated by the right hand panels in Fig. 4.2. Panels (f) and (i) show that there is an overall increase in charge density and recombination throughout the device as the degree of mixing is increased to 70%. At this point, the amorphous, mixed region dominates charge transport through the active layer. Most of the fine structural details of the observables which was originally present at lower degrees of mixing are lost as the morphology becomes more like that of a homogeneous medium. At this extreme, although charge accumulation is lessened in some areas, most regions of the active layer see increased charge density. The redistribution of charges from 'dead-ends' into the amorphous mixed regions results in both a greater average electron density and higher amounts of recombination throughout the device, both of which contribute to an overall drop in device performance, as will be discussed in Sec. 4.3.5. The trends for the average electron density for all of our C-H morphologies as a function of mixing are presented in Fig. 4.4. We see similar trends for most of the average domain sizes as were noted for the ∼10-nm morphology in Fig. 4.2, where charge density decreases upon initial mixing, but increases at higher levels mixing. Of particular note is that the charge density of the 4-nm device *only* increases with mixing. It appears that at this feature size, there are already many conducting pathways and almost no morphological traps. As such, the introduction mixing does nothing to ease chokepoints and dead-ends and the debilitating effects of the mixed-phase manifest immediately.

4.3.4 Conducting Pathways

So far, it appears that the introduction of a mixed-phase region most directly affects charge transport by either reducing the severity of dead-ends that trap carriers or by constricting

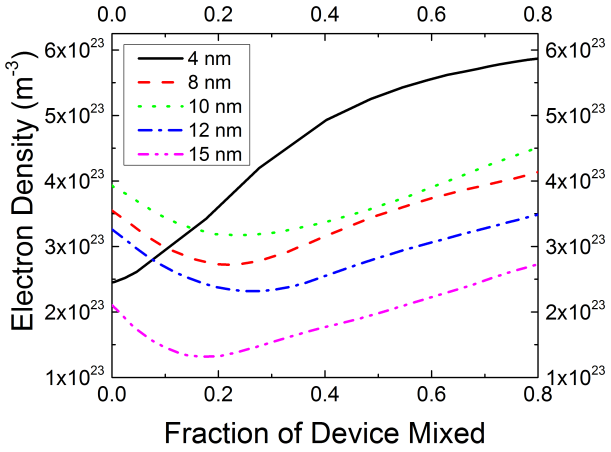

Figure 4.4: Average electron density of the five different Cahn-Hillard BHJ morphologies at varying degrees of mixing. Although most morphology length scales exhibit a drop and subsequent in electron density, the 4-nm device only exhibits a rise in electron density as its conduction pathways are constricted.

preexisting pure-phase conducting pathways. This can be more clearly seen by examining the electron current density profiles of active layers with varying degrees of mixing, which is shown in the last row of Fig. 4.2(j)-(l). For the sake of clarity, we present only the y-component of the electron current density vector, $J_{n,y}$. The colormap scale is such that white corresponds to electrons flowing down towards the cathode while black corresponds to electrons flowing up towards the anode. Note that the tortuous morphology prevents many electrons from being extracted from the device and there is significant leakage current in proximity of the anode, which reduces the resulting photocurrent.[138] In the non-mixed morphology, there are more occurrences of leakage current throughout the device, particularly at dead-ends and far upstream of high conductivity pathways. At these points, charge carriers are unable to drift towards the cathode and instead must reverse direction to either find a new conduction pathway or leak out of the device at the anode. These points of current "reversal" appear to be exacerbated by the abrupt interface between conducting phases. Upon the introduction of an interfacial mixed-phase region, there is an immediate drop in leakage current and current reversal near structural dead-ends: clearly, charges are able to flow through the device with less obstruction from the morphology with the addition of a mixed-phase. This should manifest in the device's increased fill-factor and J_{SC}, which

Average Domain Size	PCE (%)	J_{SC} (mA cm^{-2})	FF	V_{OC} (V)
4 nm	2.87	-9.43	0.510	0.690
8 nm	1.71	-4.71	0.562	0.677
10 nm	0.783	-4.00	0.425	0.639
12 nm	1.25	-3.56	0.550	0.685
15 nm	1.42	-3.21	0.600	0.722
Experimental Morphology	0.616	-3.38	0.409	0.642

Table 4.3: The initial absolute figures of merit for all of the simulated devices without a mixed-composition phase present.

we will illustrate in Sec. 4.3.5. However, at higher levels of mixing, the high conductivity pathways are narrowed, particularly in proximity to the cathode, as indicated on Fig. 4.2(k). Transport through the mixed-phase then becomes the limiting factor for device performance as carriers slowly traverse through the less conductive amorphous region and constricted pure-phase conduction channels.

It appears that this balance and interplay between the amelioration of dead-ends and the narrowing of high-current channels is more pronounced for simulated morphologies with larger average feature sizes. In the case of morphologies with a 4-nm average feature size, the bicontinuous network is so fractal compared to the dimensions of the device that there is already a preponderance of conducting pathways. With features sizes this small, the device can be viewed as being intimately mixed from the beginning as far as charge transport is concerned, despite the absence of an explicitly-mixed region. Although the introduction of a mixed-phase may reduce some of the of dead-ends in the device, the many conducting pathways of this device are also significantly constricted (See Appendix B). This constriction occurs at a lower degree of mixing than for the coarser morphologies, partly because the pure-phase conduction pathways of the 4-nm morphology are already narrow to begin with. Thus, morphologies with domain sizes of ∼4-nm are so susceptible to conduction channel narrowing that introduction of an interfacial mixed-phase leads to no improvement whatsoever in performance.

4.3.5 Effects of mixed-phase on Device Performance

We now understand in general terms how the presence of a mixed-phase may both improve and hinder charge transport through a BHJ active layer by either easing morphological traps or narrowing conducting channels. With this understanding, we turn in this Section to exploring precisely how the introduction of a mixed-phase affects photovoltaic device performance. In Fig. 4.5, we illustrate the effect of introducing different amounts of interfacial mixing on the power conversion efficiencies (PCE) of simulated devices with different average domain sizes. The figure plots the percent variation of the devices' PCE's from their value in the absence of any mixed-phase, so that the effects of mixing can be compared for BHJs with the pure phases separated on different length scales. The absolute values of the simulated devices' power conversion efficiencies and other figures of merit are given in Table 4.3. Most of the morphologies exhibit an initial improvement in power conversion efficiency upon the introduction of mixed-composition interfacial regions. However, this improvement in PCE does not persist at higher degrees of mixing, and it is clear that the performance of overly-mixed devices suffers, dropping below the devices' original PCE. For most of the morphology length scales we tested, the peak in device performance occurs when the mixed-phase accounts for approximately 15–20% of the devices' total active area. However, the 10-nm length scale morphology, which benefits the most from mixing, reaches its peak performance at approximately 45% mixed-phase with nearly double the unmixed power conversion efficiency. And as discussed above, when the average feature size is very small, as with the 4-nm feature size morphology, the addition of any interfacial mixed-phase hinders the performance of the device, with the overall efficiency dropping by $\sim$50% as the finely mixed BHJ's transport properties become increasingly dominated by the mixed-phase.

4.3.5.1 Short-Circuit Current (J_{SC})

To better understand how the interplay between the degree of mixing and the overall device morphology affect device performance, in Fig. 4.6, we plot the change in J_{SC} of our simulated devices as a function of the degree of mixing. As with the trend in PCE, most of the

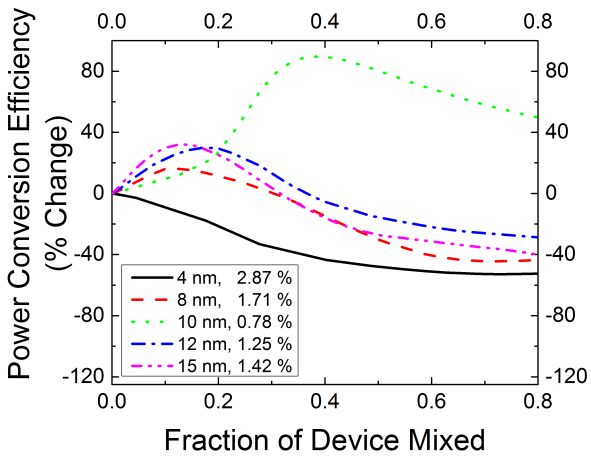

Figure 4.5: Change in power conversion efficiency of five Cahn-Hilliard generated BHJ morphologies with different intrinsic separation length scales studied as a function of the degree of mixing of the two pure phases.

devices' J_{SC}'s improve upon the introduction of a mixed-phase. Unlike the trend for PCE, however, most of the simulated devices' J_{SC}'s reach a plateau after their initial increase, rather than decreasing at higher degrees of mixing. The point at which this plateau occurs is slightly different for each device morphology length scale, but most of the devices appear to reach their J_{SC} plateau at ~15–35% mixed-phase. One exception is the device with 4-nm average feature size, which show only a very small increase in J_{SC} with increased mixing before dropping below its original value. This is because the finely structured BHJ possesses relatively few morphological traps, so the introduction of a mixed-phase provides little to no benefit to charge transport, and actual diminishes charge transport as the highly conducting pure phases are narrowed. For the coarser morphologies (greater than 8-nm average domain size), there are enough morphological traps such that mixing improves the J_{SC}, but at higher degrees of mixing, this improvement is counteracted by the narrowing of the pure-phase conducting channels, accounting for the plateau in J_{SC} of these devices upon further mixing.

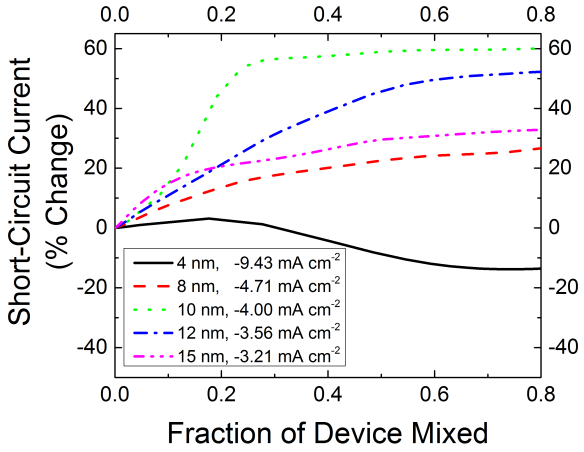

Figure 4.6: Change in the short-circuit current of five Cahn-Hilliard generated BHJ morphologies with different intrinsic separation length scales studied as a function of the degree of mixing of the two pure phases.

4.3.5.2 Fill-Factor (*FF*)

Figure 4.7 shows that the fill factors (*FF*s) of our simulated devices each exhibit rather distinctive trends, depending on their morphological length scale, upon the introduction of different amounts of interfacial mixed-composition phase. Most of the BHJ length scales (8, 12, and 15 nm) follow a similar trend as seen for the overall device performance: an initial improvement followed by a significant drop at high levels of mixing. As previously noted, for the 4-nm C-H morphology, which has very few initial morphological traps, the introduction of a mixed-phase only serves to constrict the devices' conducting pathways, which manifests as a lower fill factor. The BHJ with the 10-nm morphology, however, exhibits the most unusual and non-monotonic trend. The active layer with the 10-nm average size scale initially follows the same trend as the 4-nm device, in that its fill-factor drops. However, with increased mixing, the 10-nm BHJ morphology's fill-factor experiences a sharp rise, peaks, and then drops off again.

This unusual trend can be understood by examining the structural changes that occur in BHJs with this length scale morphology as its pure phases are mixed (Fig. 4.2(a)-(c)). The BHJ initially possess several long, relatively straight conduction channels for electrons (white, connected segments). There are also several isolated regions of acceptor material

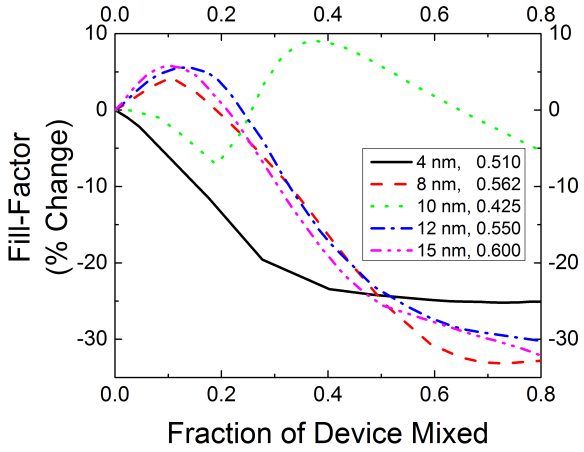

Figure 4.7: Percent change in the fill-factor of five Cahn-Hilliard generated BHJ morphologies with different intrinsic separation length scales studied as a function of the degree of mixing of the two pure phases.

(left portion of figures) that are disconnected and do not allow for proper electron transport. A small degree of mixing hinders the current, and thus the FF, because the most prominent effect of mixing for this morphology is the narrowing of the conducting pathways. However, as the size of the mixed-phase is increased, previously separated conducting segments become connected, creating new conduction pathways that restore carrier balance and improve the FF, before the eventual blurring of the conductive pathways ultimately decreases device performance. All of this illustrates how random variations in an OPV's active layer morphology can have a major and unexpected impact on device performance, and why there has been so much discussion in the literature about precisely how much mixed-phase is optimum.

4.3.5.3 Open-Circuit Voltage (V_{OC})

The last figure of merit of note for OPV devices is the open-circuit voltage. The V_{OC} is the applied voltage bias necessary to counteract the flow of charge from the built-in electric field. This means that near V_{OC}, drift currents are minimized, so any variation in V_{OC} resulting from the introduction of interfacial mixed-phase should be manifest primarily via diffusion current effects in the D-D model. The diffusion current, however, is limited by the mobility of charge carriers, and the mobility of the carriers in OPVs is quite low regardless

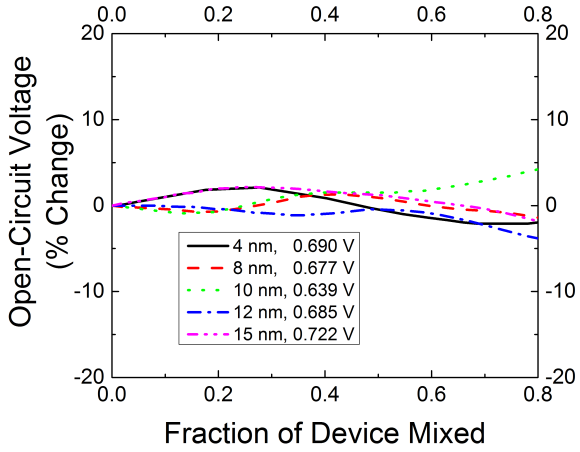

Figure 4.8: Percent change in the open-circuit voltages of five Cahn-Hilliard generated BHJ morphologies with different intrinsic separation length scales studied as a function of the degree of mixing of the two pure phases.

of the degree of mixing. As such, we would expect that the introduction of a mixed-phase should have only a small effect on an BHJ device's V_{OC}. Our simulations support this reasoning, as illustrated in Fig. 4.8. For all morphology length scales, the introduction of a mixed, interfacial region has minimal effect on the simulated devices' V_{OC}. There are some minor fluctuations, particularly for morphologies with the smallest and largest feature sizes. However, these fluctuations are less than $\sim$5%, and are much smaller than the more drastic changes exhibited by the other figures of merit. The relative non-dependence of an OPV device's V_{OC} on active layer morphological features, such as the presence of a mixed-phase, is in line with our previous investigations of the effect of structural disorder on device performance.[52]

4.4 Conclusions

With this study we have illustrated that the mixed-composition phase can have both beneficial and detrimental effects on the overall performance of the device. On the one hand, the mixed-phase can, to an extent, reduce the tortuosity of a morphology that is obstructive to charge transport by reducing dead-ends and creating new conduction pathways, leading to improved performance. However, at higher degrees of mixing, overall performance suffers as

conduction pathways are constricted and charges are forced to conduct through the relatively nonconductive mixed-phase. The point at which the mixed-phase switches from helping to hindering device performance is furthermore dependent on the average feature size and the connectivity of the device's morphology. When there are relatively few morphological traps, as was the case for the 4-nm and 10-nm device, the introduction of a mixed-phase offers little benefit, since there are no traps to ameliorate. However, as was seen with the 10-nm device, the introduction of mixed-phase can also allow for the creation of new conduction pathways between regions previously separated by non-conducting material. This shows that a mixed-phase may have significant effects depending on the exact details of a device's morphology. Of particular note is that the greatest improvement in overall device efficiency was exhibited by the 10-nm device. This is also the typical morphological length scale of most BHJ-type solar cells. This suggests that the presence of an mixed-phase plays a significant role in the charge transport properties of many high performing BHJ devices and may be necessary for optimum device performance of most BHJ-type organic solar cells. Overall, the impact of a mixed-composition interfacial phase on an OPV device's performance is highly non-monotonic. Since different donor/acceptor blends exhibit different phase separation kinetics and degrees of mixing in a uncontrollable way, it is highly likely that the performance impact of the mixed-phase is one of the root causes for the difficulty involved with optimizing new OPV donor/acceptor blends for device performance. This suggests that new fabrication techniques, such as sequential processing of donor/acceptor materials[4], are required to manipulate and control the degree of mixing in BHJ devices in a reproducible manner.

CHAPTER 5

Theory of Current Transients in Planar Semiconductor Devices: Insights and Applications to Organic Solar Cells

5.1 Introduction

Planar semiconductor diodes form the backbone of important technologies such as solid-state lighting and photovoltaic energy conversion. The relatively simple physics associated with these one-dimensional devices also makes them ideal for studying the properties of emerging functional materials [169, 40, 44, 124, 161, 104, 113, 99]. For instance, in the fields of dye-sensitized solar cells and organic photovoltaics (OPVs) [40, 18, 19], substantial insights on recombination and charge transport have been gained by examining photocurrent, photovoltage, and charge-extraction transients of planar diode devices [157, 155, 111, 67, 64, 35, 34, 43, 47, 46, 131, 132, 130, 66, 109]. In terms of specific analysis, examination of the temporal decay of photocurrent transients has been used to measure the charge-transport properties of organic semiconductors [33, 168, 136], while the integral of these transients has been taken to quantify initial amounts of photogenerated charge [5, 10, 166]. Additionally, charge-extraction transients have been routinely used to probe semiconductor recombination kinetics, average doping densities, and carrier mobilities [156, 84, 69, 45, 137, 65].

Despite these and countless other studies, the physics of current transients in planar optoelectronic devices is often overlooked or presumed to be obvious. Because such measurements are ultimately a major determinant of benchmark material properties, it is especially impor-

tant that their physics be thoroughly understood both conceptually and analytically. Thus, in this paper, we present a thorough analytical analysis of current transients in planar diode-like semiconductor devices. Although our reference point comes from the field of OPVs, the equations we present are general and apply to any planar semiconductor device, so long as the transients are not dominated by external RC effects.

Our approach is based on a consideration of the average charge densities within the semiconductor layer. Although some information is lost by averaging, this is not particularly restrictive because, experimentally, one often only has access to spatially-averaged values of the carrier concentrations. After deriving an expression for the total measured current, we then present equations describing the subtle but highly important charge on the electrodes as well as the time integral of a current-density transient for the purpose of assessing the initial amount of free charge in the active layer. We find that non-intuitive displacement current effects have led to misinterpretations of charge-extraction measurements, particularly in the organic solar cell literature. As examples, we apply our new formalism to a variety of transient current experiments commonly used to characterize the active layers of semiconductor diodes, including time-of-flight (ToF) [119, 77], transient photocurrent [33, 165, 168, 170, 102], and photoinduced charge extraction by linearly increasing voltage (photo-CELIV) measurements [78, 106, 121, 179]. In the context of the original CELIV framework, our new, generalized formalism reveals a common misinterpretation of CELIV integrals that results in an error in the estimation of the initial free carrier concentration by at least a factor of two [106, 79, 123]. The existence of such misunderstandings and their increasing prevalence in solar cell research underlines the importance of the general framework described in this work. Finally, in order to visualize our formalism and verify that it is built into common drift-diffusion solvers, we numerically simulate a photo-CELIV trace and compare the total current calculated to that predicted by our analytic equations. As expected, the two approaches yield precisely the same result, confirming that our formalism is a simple, physically correct, and general way to think about current transients in planar devices.

5.2 Derivation of a General Current-Density Equation for 1-D Planar Semiconductor Diodes

5.2.1 Contributions to the Total Measured Current

To analytically analyze current transients in semiconductor devices, we begin by considering a planar diode structure at uniform temperature that is well-described by simple 1-D electrodynamics. The relevant equations for the electric current are therefore:

$$\frac{dn}{dt} = G - R + G_e^D - R_e^D + G_e^A - R_e^A + \frac{1}{q}\frac{dJ_n}{dx} \tag{5.1}$$

$$\frac{dp}{dt} = G - R + G_h^D - R_h^D + G_h^A - R_h^A - \frac{1}{q}\frac{dJ_p}{dx} \tag{5.2}$$

$$J_{_D} = \epsilon\frac{dE}{dt} \tag{5.3}$$

$$J_{\text{tot}} = J_n + J_p + J_{_D} \tag{5.4}$$

where n, p are the mobile electron and hole concentrations, respectively, G is the generation rate of mobile-carrier pairs, R is the recombination rate of mobile-carrier pairs, $G_{e,h}^{D,A}$ are the generation rates of mobile carriers from localized donor- and acceptor-type trap sites, $R_{e,h}^{D,A}$ are the recombination rates of mobile charge into localized donor- and acceptor-type trap sites, E is the electric field, ϵ is the semiconductor permittivity, q is the absolute value of the electron charge, $J_{n,p}$ are the electric current due to mobile electrons and holes, $J_{_D}$ is Maxwell's displacement current, and J_{tot} is the experimentally measured total electric current at a given time and position in the device. Physically, Eqs. (5.1) and (5.2) account for the continuity of free carriers and simply add or subtract the contributions of both bulk and trap-mediated recombination/generation to the free carrier populations.

Our goal is to use the above equations as a starting point to obtain a more insightful and experimentally-relevant expression for J_{tot} (Eq. (5.4)) in terms of the average generation and recombination processes and the average carrier concentrations. In this regard, it is highly important to note that J_{tot} does not vary spatially within the device (see Appendix C for

derivation), which means that the (average) total current anywhere within the active layer is equal to the total current everywhere at a given time.

Our sign convention is chosen such that recombination current is positive and generation current is negative, as is commonly used when reporting experimental (photo)diode currents. Furthermore, it is important to distinguish between the generation and recombination of mobile carrier pairs (G,R), which are shared terms in the continuity equations, and the individual generation and recombination rates of mobile carriers through immobile trap sites ($G_{e,h}^{D,A}$,$R_{e,h}^{D,A}$), which are not shared because an oppositely-charged mobile carrier is not necessarily created or destroyed simultaneously. Traditionally, the $G_{e,h}^{D,A} - R_{e,h}^{D,A}$ terms in Eqs. (5.1) and (5.2) are treated as a net recombination rate within the Shockley-Read-Hall (SRH) formalism [154, 63], but such a treatment is not necessary for the derivation at hand.

5.2.2 Mobile-Carrier Currents

To develop a new expression for J_{tot}, we start by integrating Eqs. (5.1) and (5.2) across the device thickness to spatially average the continuity equations:

$$J_n(d) = qd\frac{d\bar{n}}{dt} - qd\langle G - R\rangle - qd(\langle G_e^D - R_e^D\rangle + \langle G_e^A - R_e^A\rangle) + J_n(0) \tag{5.5}$$

$$J_p(0) = qd\frac{d\bar{p}}{dt} - qd\langle G - R\rangle - qd(\langle G_h^D - R_h^D\rangle + \langle G_h^A - R_h^A\rangle) + J_p(d) \tag{5.6}$$

where $\bar{n}d = \int_0^d n(x)\,dx$ and $\bar{p}d = \int_0^d p(x)\,dx$ are the average carrier concentrations in the active layer, d is the semiconductor active-layer thickness, q is the elementary charge, and $\langle G - R\rangle$ and $\langle G_{e,h}^{D,A} - R_{e,h}^{D,A}\rangle$ are the spatially averaged differences in generation and recombination over the entire active-layer thickness. Figure 5.1 schematically illustrates the formalism described above on a semiconductor energy band diagram. Eqs. (5.5) and (5.6) have the advantage of removing the spatial derivative of the free-carrier current densities and replacing them with the averaged quantities and processes of interest. The fact that the current densities are evaluated at the contacts is acceptable because the quantity of interest, J_{tot}, is constant at all positions throughout the active layer.

5.2.3 The Displacement Current

In order to complete the expression for J_{tot} (Eq. (5.4)), we must also derive expressions for the displacement current J_D (Eq. (5.3)) at either of the contacts ($x = 0$ and/or d) that are decoupled from each other. We note that simply integrating Gauss's law, $dE/dx = \rho/\epsilon$, and combining with the displacement current (Eq. (5.3)) will not suffice because $J_D(0)$ and $J_D(d)$ would be coupled. To ultimately decouple $J_D(0)$ and $J_D(d)$, we must use the general 1-D solution of Gauss's law for a plane of charge [54] in order to relate the electric field at the contacts to the average carrier concentrations within the active layer:

$$E(0) = -\frac{qd}{2\epsilon}(\bar{p} - \bar{n} + \bar{N}_D^+ - \bar{N}_A^-) + \frac{\sigma_{\text{EL}}}{2\epsilon} \tag{5.7}$$

$$E(d) = \frac{qd}{2\epsilon}(\bar{p} - \bar{n} + \bar{N}_D^+ - \bar{N}_A^-) + \frac{\sigma_{\text{EL}}}{2\epsilon} \tag{5.8}$$

where $\bar{N}_{D,A}^{+,-}$ are the average number density of immobile ionized trap sites within the active layer, which we consider as localized electron states that can either be neutral when filled (N_D) or neutral when empty (N_A), and are only singly charged. We define $\sigma_{\text{EL}} = \sigma_0 - \sigma_d$ to represent the areal charge on the metal electrodes, with $\sigma_{0,d}$ being the areal charge densities on the left and right metal contacts, respectively (Figure 5.1). The charge densities $\sigma_{0,d}$ can be either positive, negative, or zero, and we use their difference, σ_{EL}, for the rest of the paper because it is directly proportional to the total electric field contribution from the charge on the metal electrodes. Additional considerations regarding the charge on the electrodes are presented in Section 5.2.6. below and in the Appendix C. We note, though, that the electric field at the contacts is dependent only on the average charge within the active layer and not on its specific distribution, which is a unique consequence of the simple physics of charged 1-D planes [54]. Equations (5.7) and (5.8) are also the origin of the factor of 1/2 that will carry on throughout this derivation—another consequence of the physics of charged 1-D planes [54].

With the primary electric field contributions in hand, we can now simply apply Eq. (5.3)

to Eqs. (5.7) and (5.8) to obtain the decoupled displacement current at each of the contacts:

$$J_{D}(0) = \frac{qd}{2}\left(\frac{d\bar{n}}{dt} - \frac{d\bar{p}}{dt}\right) + \frac{qd}{2}\left(\frac{d\bar{N}_{\mathrm{A}}^{-}}{dt} - \frac{d\bar{N}_{D}^{+}}{dt}\right) + \frac{1}{2}\frac{d\sigma_{\mathrm{EL}}}{dt} \tag{5.9}$$

$$J_{D}(d) = \frac{qd}{2}\left(\frac{d\bar{p}}{dt} - \frac{d\bar{n}}{dt}\right) + \frac{qd}{2}\left(\frac{d\bar{N}_{D}^{+}}{dt} - \frac{d\bar{N}_{\mathrm{A}}^{-}}{dt}\right) + \frac{1}{2}\frac{d\sigma_{\mathrm{EL}}}{dt} \tag{5.10}$$

As a check of validity, the difference in the displacement current at the two contacts according to Eqs. (5.9) and (5.10) is proportional to the time rate of change of the charge density within the semiconductor layer, which is expected from a simple integration of Gauss's law. Just like the electric fields, these simple expressions for the displacement current at the contacts depend only on the average internal charge density and not on the charge-density profile—a consequence of the simple physics of planar geometries.

We would now like to substitute Eqs. (5.9) and (5.10) along with Eqs. (5.5) and (5.6) into Eq. (5.4) in order to obtain the total measured current density (J_{tot}) at the contacts and therefore everywhere. However, in order to simplify the final result, we first derive relationships between $\bar{N}_{D,A}^{+,-}$ and the kinetic processes that connect them, $G_{e,h}^{D,A}$ and $R_{e,h}^{D,A}$. Fortunately, this is done straightforwardly by summing the generation and recombination events that create and annihilate ionized trap sites, leading to the following kinetic equations:

$$\frac{d\bar{N}_{D}^{+}}{dt} = \langle G_{e}^{D} - R_{e}^{D}\rangle + \langle R_{h}^{D} - G_{h}^{D}\rangle \tag{5.11}$$

$$\frac{d\bar{N}_{A}^{-}}{dt} = \langle R_{e}^{A} - G_{e}^{A}\rangle + \langle G_{h}^{A} - R_{h}^{A}\rangle. \tag{5.12}$$

As noted above, these equations only consider singly ionized states.

5.2.4 The Total Measured Current

We can now combine all of the relevant relations obtained above to produce a more insightful expression for the total measured electric current density in terms of the averaged quantities of interest. We do this by combining Eqs. (5.5) and (5.6) with Eqs. (5.9-5.12) at each contact

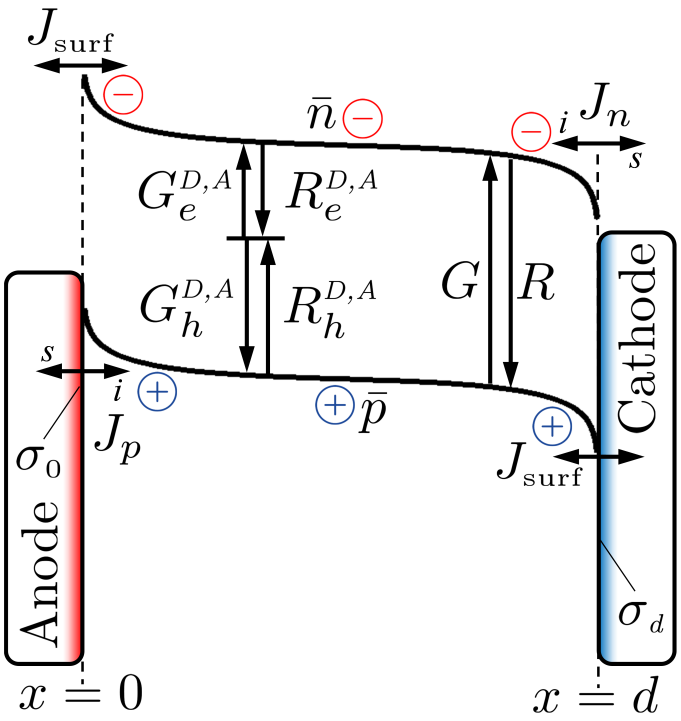

Figure 5.1: A schematic band diagram illustrating the device model used in this derivation in forward (positive) bias. The semiconductor (photoactive) layer is sandwiched between metal contacts at $x = 0$ and $x = d$. The i and s scripts on the J_n (electron current) and J_p (hole current) arrows stand for injection and sweep out, respectively. The average carrier densities are $\bar{n}$ for electrons and $\bar{p}$ for holes. The generation and recombination rates of electron-hole pairs, G and R, are distinct from the rates of freeing and trapping carriers from traps, $G_{e,h}^{D,A}$ and $R_{e,h}^{D,A}$. J_{surf} takes into account the 'surface' current that does not effectively make a transition though the semiconductor energy gap. Note that only the relative heights of the anode/cathode depictions are meant to be part of the implicit energy scale.

to obtain an expression for J_{tot} (Eq. (5.4)) as a function of time:

$$J_{\text{tot}} = \frac{qd}{2}\left(\frac{d\bar{p}}{dt} + \frac{d\bar{n}}{dt} + \sum\langle R_{e,h}^{D,A} - G_{e,h}^{D,A}\rangle\right) + qd\langle R - G\rangle + \frac{1}{2}\frac{d\sigma_{\text{EL}}}{dt} + J_{\text{surf}} \tag{5.13}$$

where the summation term in Eq. (5.13) covers all subscript combinations displayed in Eqs. (5.5) and (5.6), and the other terms are discussed in detail below.

Eq. (5.13) is the first of two primary theoretical results of this paper. Its simple form—only dependent upon average charge densities and kinetic processes—is a direct consequence of the straightforward physics of charged planes. Eq. (5.13) and the preceding analysis provide both a simple conceptual framework for generally thinking about current transients in planar devices as well as reveal non-trivial aspects of these measurements, such as the prefactor of one-half in front of the first term. This general but non-intuitive factor is independent of the carrier distributions and spatial generation/recombination profiles and arises from the combination of Gauss's law and the displacement current for planar 1-D electrodynamic systems (Eqs. (5.7)-(5.10)). The factor of one-half means that uniformly injecting or extracting only electrons or holes, for example, results in a measured current proportional to just half of the rate of change in average hole concentration. It also means that current measured by vacating traps, like that in thermally-stimulated currents, I-DLTS, or even charge-extraction experiments is only half due to mobile charge carriers if sweep-out causes negligible changes in the carrier concentrations [81, 25, 125, 145, 69, 167, 10]. Thus, if this factor of one-half that results from displacement current effects is not properly accounted for, the deduced amount of charge extracted in various experiments will be off by at least a factor of two. Although this may not be a significant correction for many applications, it at least serves as a lesson that the interpretation of current transients is not necessarily trivial.

Despite the fact that the factor of one-half in Eq. (5.13) is generally ignored, it is clearly necessary from a conceptual standpoint. Consider the case where mobile carriers are photogenerated within the semiconductor layer with negligible recombination, extraction current, leakage current, or changes in the electrode charge. In such a scenario, the spatially integrated generation rate equals the rate of change of the average concentrations of both

carriers, $\langle G \rangle = d\bar{n}/dt = d\bar{p}/dt$, and thus in Eq. (5.13) the measured current sums to zero. This makes intuitive sense because no current should be measured if mobile carriers are generated uniformly in a hypothetical semiconductor device with no built-in potential or recombination. Such a simple situation could not be understood without the factor of one-half in Eq. (5.13).

It is also worth noting that even if the change in electrode charge ($d\sigma_{\text{EL}}/dt$), generation, recombination, and leakage current (J_{surf}) are negligible, the average carrier concentrations can still change implicitly by charge carrier flow through the 'correct' contact (i.e., extraction by 'sweep out' and filling by injection for a diode; see Figure 5.1) [31, 33], which are critical aspects of any solar cell or LED. Indeed Eq. (5.13) could be optionally re-written as $J_{\text{tot}} = J_{i,s} + J_{\text{EL}} + J_{\text{sur}}$, where $J_{i,s}$ is composed of the first two terms of Eq. (5.13) and embodies the net injection or sweep out (extraction) of carriers into or out of the semiconductor material, and J_{EL}, the third term in Eq. (5.13), represents the current density due to changes in the electrode charge density (see Eq. (5.15), discussed below), and the last term, J_{surf}, takes into account the 'surface' current that does not effectively make a transition though the semiconductor energy gap.

5.2.5 The Surface Recombination Current, J_{surf}

As just alluded to, the J_{surf} term in Eq. (5.13) accounts for current that effectively traverses the active layer without making a transition though the semiconductor energy gap. Here J_{surf} is mathematically defined as $J_{\text{surf}} = J_n(0) + J_p(d)$. For a diode, J_{surf} is typically dubbed surface recombination and includes the net electron extraction/injection at the hole-selective contact (anode) and net hole extraction/injection at the electron-selective contact (cathode, see Fig. 5.1). In other words, positive J_{surf} corresponds to net carrier extraction at the wrong contact(s) while negative J_{surf} corresponds to net carrier injection at the wrong contact(s). The J_{surf} term is often referred to as 'shunt' or 'leakage' current in diodes, LEDs, and solar cells, and herein we use all of these terms interchangeably. In addition to Ohmic-like leakage [48], the implied surface recombination that underlies J_{surf} is expected in OPV diodes to have an exponential voltage dependence with low ideality factor and therefore will be important

at higher biases/charge densities [85, 180, 88]. In single-carrier devices, J_{surf} is often analyzed from the standpoint of space-charge limited current [15].

5.2.6 Areal Charge Densities on the Contacts

A highly important aspect of Eq. (5.13) is that the seemingly benign $d\sigma_{\text{EL}}/dt$ term can often significantly contribute to the total measured current. To better understand this term, here we discuss the physical attributes of the device that determine σ_{EL}.

The free-carrier density of the metal electrodes is typically sufficiently high such that the electric field is zero inside them at all times [55]. Under this reasonable (but not always true [142]) limit, the total areal charge summed over both electrodes must be equal and opposite to the total charge within the active layer, or $\sigma_0 + \sigma_d = -qd(\bar{p} - \bar{n} + \bar{N}_D^+ - \bar{N}_A^-)$. A related consequence is that the surface charge is directly proportional to the electric field immediately outside the surface, or $\sigma_0 = \epsilon E(0)$ and $\sigma_d = -\epsilon E(d)$ [56], where the sign of $\sigma_{0,d}$ depends on the sign of the charge. These relations will be used below in conjunction with drift-diffusion calculations to determine σ_{EL} at various times during a simulated solar cell photo-CELIV transient.

One can conceptually imagine the σ_{EL} term as a variable quantity that is used to supply enough electric field to meet the imposed voltage conditions. As derived in Appendix C, σ_{EL} is only a function of the space-charge distribution within the device and the electric potential drop across the active layer ($V = -\int_0^d E\,dx$) according to

$$\sigma_{\text{EL}} = \bar{\rho}d - \frac{2}{d}\int_0^d \int_0^x \rho(\acute{x})d\acute{x}\,dx - \frac{2\epsilon V}{d} \tag{5.14}$$

$$J_{\text{EL}} = \frac{d}{2}\frac{d\bar{\rho}}{dt} - \frac{1}{d}\int_0^d \int_0^x \frac{d\rho(\acute{x})}{dt}d\acute{x}\,dx - \frac{\epsilon}{d}\frac{dV}{dt} \tag{5.15}$$

where $\rho(x) = q[p(x) - n(x) + N_D^+(x) - N_A^-(x)]$, $\acute{x}$ is a dummy variable for spatial integration, $2J_{\text{EL}} = d\sigma_{\text{EL}}/dt$, and $\bar{\rho}d = \int_0^d \rho(x)\,dx$.

Eqs. (5.14) and (5.15) show that $d\sigma_{\text{EL}}/dt$ is non-zero only if the applied bias or the spa-

tial distribution of net charge are changing with time. We strongly emphasize that V in Eq. (5.14) and all other equations herein is just the electric potential difference across the active layer and not the total potential difference (V_{tot}). The total potential difference in a diode often includes an additional built-in (diffusion, composition, etc.) potential (V_{BI}) that is nominally constant with light intensity and applied bias [14]. Since V_{BI} is usually well-approximated as a constant, the electric potential and total potential are related by $V(t) = V_{\text{tot}}(t) - V_{\text{BI}}$, and the conclusions made herein are essentially unchanged.

Equations (5.14) and (5.15) also tell us something about the measured device capacitance. This is recognized by the fact that the voltage derivative of Eq. (5.14) is related to the electrode capacitance, though one must also account for the charge stored in the active layer ('chemical capacitance') when considering the total measured capacitance of a diode [181, 13, 118]. Interestingly, though, Eq. (5.15) reduces to the classical parallel-plate capacitor current, $C_g \cdot dV/dt$, where $C_g = \epsilon/d$ if the internal space-charge distribution is not changing in time, independent of the space-charge distribution. In other words, Eq. (5.15) implies that the effective device geometric capacitance is independent of any static space-charge profile, only deviating from its classical value of ϵ/d when the internal space-charge distribution is changing in time. Unfortunately, since the difference in electric potential between the contacts depends on the specific space-charge distribution, it is not possible to determine a more simple relationship between the effective geometric capacitance, the charge on the electrodes, and the potential difference across the device beyond what is presented in Eqs. (5.14) and (5.15). Additionally, as an aside, the σ_{EL} term can be eliminated to yield a generalized relation between the electric-field profile $E(x)$, the electric-potential difference across the device V, and the internal space-charge/dielectric profile $\rho(x)/\epsilon(x)$ (see Appendix C and Eq. (S12)).

5.2.7 Integrating the Total Measured Current

The factor of one-half in Eq. (5.13) is relevant to experiments on diodes because Eq. (5.13) is often experimentally integrated over an extraction-current transient in order to estimate the initial average steady-state carrier concentration in such devices [156, 111, 112, 35, 34,

36, 144]. When integrating Eq. (5.13) over a current transient and multiplying by $1/qd$, we find that the apparent initial carrier concentration ($\Delta\bar{n}_{\text{meas}}$) is

$$\Delta\bar{n}_{\text{meas}} = \frac{1}{2}(\Delta\bar{n} + \Delta\bar{p}) + \frac{\Delta\sigma_{\text{EL}}}{2qd} + \int_0^{t_{\text{tr}}} \left(\frac{J_{\text{sur}}}{qd} + \frac{1}{2}\sum \langle R_{e,h}^{D,A} - G_{e,h}^{D,A} \rangle + \langle R - G \rangle \right) dt \quad (5.16)$$

where the difference terms are negative for an extraction current transient. These terms are given by, for example, $\Delta\bar{n} = \bar{n}(t_{\text{tr}}) - \bar{n}(0)$, evaluated at the start ($t = 0$) and finish ($t = t_{\text{tr}}$) of the transient. The left hand side of Eq. (5.16) is given by $qd\Delta\bar{n}_{\text{meas}} = \int_0^{t_{\text{tr}}} J_{\text{tot}}(t)\, dt$ and is the apparent amount of charge extracted or injected from integration of the (experimental) current transient.

Eq. (5.16) is the other primary theoretical result of this paper because integrated extraction-current transients are widely used, particularly in the organic solar cell community, to measure average steady-state carrier concentrations [159, 157, 156, 64, 111, 112, 37]. To our knowledge, however, a formalism describing such integrals has not been previously presented. Equation (5.16) provides significant physical insight into the most common methods of experimentally determining the average carrier densities in diode-based devices, as it details all of the apparent sources of charge present in a 1-D (extraction) current transient [159, 155, 144]. Notably, the factor of one-half in the first term of Eq. (5.13) persists, which as we discuss further below has resulted in errors in the estimation of the average charge density when such experiments were performed on organic solar cell devices.

Examples of common methods that rely heavily on integrating current transients include the charge extraction by linearly increasing voltage (CELIV) [78], charge extraction (CE) [156, 130], and time-delayed collection field (TDCF) techniques [5]. Although these methods allow experimenters to estimate the total average carrier concentrations relative to a short-circuit or quasi-depleted state, they have the downside of having to correct for the change in charge on the electrodes ($\Delta\sigma_{\text{EL}}$) at the beginning and end of the transient. Equations (5.14) and (5.16) clarify this previously nebulous correction. In particular, Eq. (5.14) reveals that $\Delta\sigma_{\text{EL}}$ is only a function of the geometric capacitance (C_g), the change in applied bias (ΔV), and the change in the internal charge-density profile ($\Delta\rho(x)$) from the beginning

and end of the transient. In many polymer:fullerene BHJ OPVs, researchers have found that consideration of only the voltage conditions and the geometric capacitance (the last term in Eq. (5.14)) is sufficient to account for $\Delta\sigma_{\text{EL}}$ in their charge-extraction measurements [159, 156, 158, 34, 36, 86]. The success of this correction implies that the OPV devices in these experiments experienced negligible changes in the internal space-charge distribution between the beginning and ending of the extraction transient. Since most BHJ OPVs are thin, have low dielectric constants, and are weakly- or un-doped, this suggests that these devices are largely space-charge free over the operational voltage regime (i.e., have a linear band structure). This conclusion is not obvious, however, without the help of Eqs. (5.14) and (5.16).

Finally, it is common to approximate the initial amount of photogenerated charge in organic photovoltaic devices by integrating the a transient photocurrent (TPC) taken at a constant DC bias [35, 34, 36]. This approach typically relies on a quick laser flash to photogenerate mobile charge, which due to the built-in potential and/or externally-applied bias results in a current transient. This transient is then integrated over time to estimate the initial amount of photogenerated charge. Equation (5.13) shows that if the bias is held constant ($\Delta\sigma_{\text{EL}} = 0$) and generation, recombination, and leakage current can be ignored (or corrected for), then the integral of the photocurrent decay is actually equal to half the sum of the average initial photogenerated charge carrier densities. Since photogeneration typically gives $\Delta n = \Delta p$, the integral of a photocurrent transient without generation, recombination, or leakage current gives an apparent initial excess carrier concentration of $\Delta\bar{n}_{\text{meas}} = \Delta\bar{n} = \Delta\bar{p}$. We note that these considerations are independent of the generation profile or initial carrier concentration distributions.

5.3 Analytical Applications of the Model: Implications for Materials Characterization

5.3.1 The Time-of-Flight Experiment

A classic approach to measuring the charge-transport properties of materials is via a time-of-flight (ToF) or transient photoconductivity experiment [165, 33, 168, 119, 77, 29, 148]. Although ToF techniques are well documented, discussing the ToF conceptual model in terms of Eqs. (5.13) and (5.15) is insightful and illustrative of the different possible sources of current in such measurements/models. We note that we do not consider aspects of trap-limited dispersive transport here, but rather emphasize that the basic physics of such measurements must first be fully understood before new/unique physical effects can be identified. Moreover, this discussion demonstrates how readily a simple physical picture can be translated into a theoretically measured current transient using the equations presented above and in Appendix C.

In the ToF experiment, a planar device is used and the semiconducting material of interest is made thick so that a laser flash photogenerates an approximately planar carrier packet at one side of the device. During the measurement, a constant applied bias and/or built-in potential is used to drive the carrier plane across the sample. Theoretically, in terms of Eqs. (5.14) and (5.15), this situation corresponds to a space-charge profile of $\rho(x) = \sigma_{\text{gen}}\delta(x - x_\sigma(t))$, where δ is the Dirac delta function, σ_{gen} is the charge density of the drifting plane, and $x_\sigma(t)$ is the spatial position of the plane of charge. Since $dV/dt = 0$ and V is dependent on $x_\sigma(t)$, a continuous supply of charge must be given to the electrodes in order to keep the voltage constant as the carrier plain drifts across the sample. Thus, by inspection of Eq. (5.13), the only source of current in the ToF model arises from changes in electrode charge. The current transient is readily derived by substituting $\rho(x) = \sigma_{\text{gen}}\delta(x - x_\sigma(t))$ into Eq. (5.15):

$$J_{\text{tot}} = J_{\text{EL}} = \frac{\sigma_{\text{gen}}}{d}\frac{dx_\sigma(t)}{dt} = q\bar{p}\mu E_{\text{EL}} \tag{5.17}$$

where μ is the mobility of the carrier plane, E_{EL} is the electric field supplied by the electrode charge (see Appendix C Eq. (S10)), and $\bar{p} = \sigma_{\text{gen}}/qd$ is the spatially-averaged carrier concentration, assumed here to arise from a plane of positive charge originating at $x = 0$. Since the total current is rigorously constant everywhere (see Appendix C), the ToF transient also can be rewritten as just the average drift current flowing within the device (RHS of Eq. (5.17)). The solution of Eq. (5.17) can be readily obtained with the aid of Eq. (S10) in Appendix C upon substituting $\rho(x) = \sigma_{\text{gen}}\delta(x - x_\sigma(t))$, giving the following differential equation and subsequent expression for the ToF current transient:

$$\frac{dx_\sigma(t)}{dt} = \mu E_{\text{EL}} = \frac{x_\sigma(t)}{\tau} - \frac{d}{2\tau} - \frac{\mu V}{d} \tag{5.18}$$

$$J_{\text{ToF}} = -\left(\frac{qd\bar{p}}{\tau} + \frac{q\bar{p}\mu V}{d}\right) e^{\frac{t}{\tau}} \tag{5.19}$$

where here $\tau = \epsilon/q\bar{p}\mu$ is the dielectric relaxation time of the semiconductor with excess conductive charge $\bar{p}$, V is assumed to be negative, and the carrier plane starts at $x = 0$. Thus, for large values of τ and high magnitudes of V, the value of J_{ToF} is, as expected, approximately constant in time and equal to $q\bar{p}\mu V/d$ due to an approximately constant velocity of the drifting plane of charge.

In short, this demonstrates that Eqs. (5.13), (5.14), and (S10) in Appendix C readily capture all the essential features and fine details of the classic ToF experiment, illustrating how a simple physical picture (a plane of charge moving across a device) results in an actual measured current transient (Eq. (5.19)). This example thus illustrates how simple current transient models in planar optoelectronic devices readily fit within the general relations derived in this work.

5.3.2 Determination of the Average Carrier Concentration with CELIV

As a more detailed example of the utility of Eqs. (5.13), (5.14), and (5.16) when applied to charge-extraction techniques that vary the applied bias, in this Section we re-examine the assumptions underlying the CELIV framework for measuring charge densities in solar

cell devices. The original analytical model describing CELIV transients by Juska *et al* [78]. considered a unipolar device with flat-band contacts and no generation, recombination, or leakage current. This model also ignores diffusion current, considering only a slab of uniform-density charge drifting under the influence of an electric field (Figure 5.2a). Lorrmann *et al.* [106] and Sandberg *et al.* [143] later presented an excellent analysis of the mathematical implications of this CELIV model using the same original assumptions and equations as Juska *et al.* [78]:

$$J_{\text{tot}} = \frac{U_{\text{R}}\epsilon}{d} + nq\left(1 - \frac{l(t)}{d}\right)\frac{dl(t)}{dt} \tag{5.20}$$

$$\frac{dl(t)}{dt} = \frac{\mu U_{\text{R}} t}{d} - \frac{nq\mu}{2\epsilon d}l(t)^2 \tag{5.21}$$

where U_{R} is the voltage ramp rate, d the film thickness, n is the uniform unipolar free-carrier density, $l(t)$ is the time-dependent extraction depth (i.e., depletion width), μ is the unipolar carrier mobility, ϵ the semiconductor permittivity, and J_{tot} the total measured current density. The properties of $l(t)$ are: $l(0) = w$, $dl(0)/dt = 0$, $0 \leq l(t) \leq d$, and $l(t_{\text{tr}}) = d$ where t_{tr} is the time taken to extract all the mobile carriers within the active layer. Schottky junctions under the full-depletion assumption are well approximated by this model through a finite initial steady-state depletion width, w (Figure 5.2a) [143].

In examining how this model is used in the literature, we find that the integral of Eq. (5.20) is often misinterpreted because of the factor of one-half in the first terms of Eqs. (5.13) and (5.16) due to improper accounting of $\Delta\sigma_{\text{EL}}$. Although this factor of one-half was recently noticed by Sandberg *et al.* [143] for the CELIV model described above, the origin of this term was not understood. The issue arises from attributing the second term in Eq. (5.20) solely to mobile carriers [7]. Under this seductive but incorrect assumption, subtracting the time independent $U_{\text{R}}\epsilon/d$ term and integrating (shaded area in Figure 5.2b) yields the presumed total number of free-carriers extracted and thus the initial carrier density [123, 179].

If this were true, however, then integrating the second term of Eq. (5.20) from $t = 0$ to t_{tr} and multiplying by $1/qd$ should give the actual initial carrier concentration n. Instead,

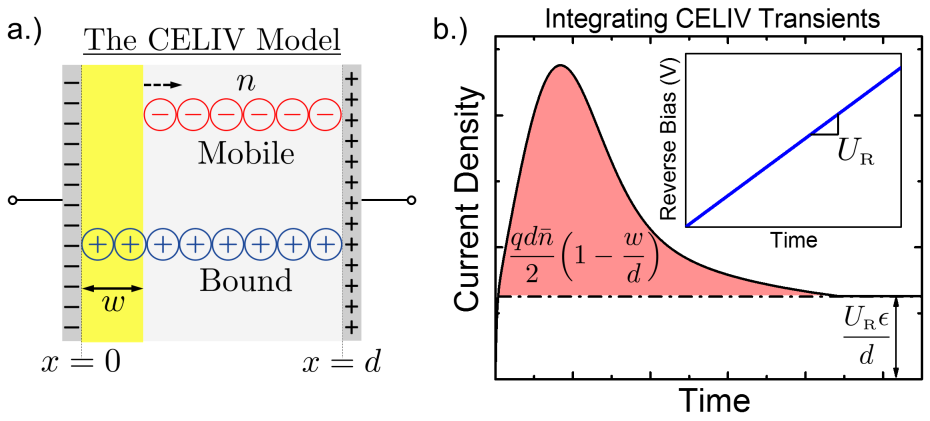

Figure 5.2: a.) Schematic representation of the CELIV model device under consideration. A uniform block of free charge with local density n and average density $n(1 - w/d)$ is swept out under a linearly changing reverse bias pulse (inset of b.)). Here w denotes the steady-state initial depletion width. b.) An Example CELIV current transient showing the typical portion of the curve that is integrated to yield the initial uniform free-carrier density (n). Non-intuitively, the shaded region is at most proportional to half of the initial average free-charge density and even further reduced if w is non-zero.

we find that:

$$\bar{n}_{\text{meas,CELIV}} = \frac{n}{d}\int_0^{t_{\text{tr}}} \left(1 - \frac{l(t)}{d}\right)\frac{dl(t)}{dt}dt \tag{5.22}$$

$$= \frac{n}{2}\left(1 - \frac{l(0)}{d}\right)^2 \tag{5.23}$$

$$= \frac{\bar{n}}{2}\left(1 - \frac{w}{d}\right) \tag{5.24}$$

where $dq\bar{n}_{\text{meas,CELIV}} = \int_0^{t_{\text{tr}}}(J(t) - U_{\text{R}}\epsilon/d)\,dt$ is the apparent initial carrier concentration in the Juska *et al.* [78] model obtained by integrating the CELIV transient with $U_{\text{R}}\epsilon/d$ subtracted away and $l(0) = w$ as the initial steady-state depletion width [143]. Thus, we see that integrating a CELIV transient in this model over the total evacuation time, t_{tr}, gives at most half of the actual mobile charges extracted, which is in exact agreement with Eq. (5.16) under the same assumptions.

In addition to this factor of 1/2 reduction, Eq. (5.24) also shows that there is another reduction of the apparent initial average free-charge density by an additional factor of $1-w/d$. Inspection of Eq. (5.16) readily reveals that this is due to electrode-charge effects. Indeed,

Eq. (5.16) indicates that if there is an initial steady-state depletion width, $w > 0$, then the initial charge on the electrodes ($\sigma_{\mathrm{EL}}(t = 0)$) will be finite due to the initial presence of space charge. Thus, the $\Delta\sigma_{\mathrm{EL}}$ correction in Eq. (5.24) will be altered from the case where $w = 0$ since both cases end in an identical fully-depleted state. This additional reduction due to $\Delta\sigma_{\mathrm{EL}}$ is generally nontrivial since in real devices the steady-state space-charge profile can take on shapes more complex than the simple rectangular version assumed by the CELIV model. Overall, though, these previously nebulous aspects of current transients are decoupled and made obvious by Eqs. (5.13), (5.14), and (5.16), thus highlighting the conceptual utility of our formalism. Overall, Eq. (5.16) readily corrects a common misinterpretation of CELIV transients and explains why, for example, Lorrmann *et al.* [106] concluded that a substantial fraction of the mobile charge within the active layer was not extracted during CELIV even after long extraction times (∼1 ms).

It is worth noting that none of the above analysis includes RC time constant effects [82], which inevitably makes interpretation of the current transients more complicated. However, we have found through numerical simulations that when RC effects are included at reasonable levels ($\tau_{\mathrm{RC}} \approx 300$ ns), the conclusions we have reached for low-mobility materials are not altered. Moreover, RC effects should mostly influence the temporal shape of the current transient, leaving the integral (Eq. (5.16)) largely unaffected.

5.4 Understanding the Formalism Via Time-Dependent Drift-Diffusion Modeling: CELIV Revisited

Lastly, to better understand each of the terms underlying the total current in Eq. (5.13) and the analysis in the previous Section, we performed time-dependent drift-diffusion numerical modeling to simulate a photo-CELIV measurement. In the following, we demonstrate that Eq. (5.13) is compatible with detailed numerical drift-diffusion simulations, verifying that we have obtained a physically correct expression for the total current.

The drift-diffusion approach involves solving the continuity equations (Eqs. (5.1) and (5.2)) along with the Poisson equation to determine the individual carrier concentrations

and the electric field during the simulation. To explicitly solve these equations, the approach assumes that the current densities follow the drift-diffusion form

$$J_n = qn\mu_n E + \mu_n kT\frac{dn}{dx} \tag{5.25}$$

$$J_p = qp\mu_p E - \mu_p kT\frac{dp}{dx} \tag{5.26}$$

where μ_n and μ_p refer to the mobility of electrons and holes, respectively, and kT is the thermal energy. We have previously performed steady-state drift-diffusion calculations to model OPV devices using homemade code [51], and we employ the same approach here only extended into the time domain (see Appendix C for a detailed description of our drift-diffusion computational approach). In this study, the time dependence is accounted for by solving the continuity equations and employing an implicit method to iterate forward in time. Recombination is assumed to take the simple reduced Langevin form ($R = q\gamma np(\mu_n + \mu_p)/\epsilon$; see Table (5.1) [80, 49, 136], and the generation profile is taken from a transfer-matrix calculation using experimentally available optical constants for the different layers [135, 23]. The device parameters for our simulations are presented in Table 5.1, and are loosely designed to be representative of those of polymer-based solar cell using P3HT and PCBM [41, 51]. We chose to simulate an organic solar cell photo-CELIV transient because photo-CELIV is a common method for studying low-mobility semiconductors and the technique involves many of the physical processes that our analytical model aims to capture: generation, recombination, and a time-varying applied voltage. The $\langle R_{e,h}^{D,A} - G_{e,h}^{D,A}\rangle$ term is the only term in Eq. (5.13) not accounted for in this simulation, and was therefore assumed to be zero.

We simulated the photo-CELIV experiment by first performing a steady-state calculation to verify that the dark J-V characteristics of the device were reasonable. Then, for the transient, our virtual device was initially held in the dark at an applied bias equal to the built-in potential, V_{BI} (Table 5.1). Next, these steady-state conditions were perturbed by a brief pulse of illumination to produce excess carriers. After this pulse, the photogeneration of carriers was set to zero and, after an additional short period of time (5 μs), a linear reverse bias voltage ramp was applied to sweep out any remaining photogenerated charge.

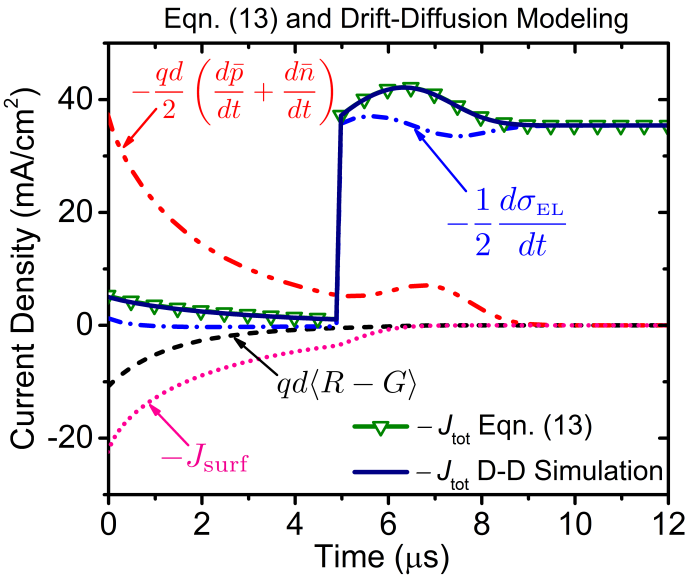

Figure 5.3: The various current contributions from Eq. (5.13) determined from numerical simulations and the negative of their sum, $-J_{\text{tot}}$ (upside down open triangles). Note that here the reverse bias extraction current is plotted as positive. The simulated CELIV ramp conditions are 0.1 V/μs starting at an initial forward bias of 0.6 V. The total current density from the simulation is also shown (solid blue line). The simulated total current density and the summed current density from Eq. (5.13) lie on top of each other, showing their precise quantitative agreement. We note that trapping was not included in the numerical model and thus was assumed to be zero.

To visualize Eq. (5.13), we explicitly calculated each term during the simulated photo-CELIV process and compared their sum to the total current calculated from the drift-diffusion simulation (Figure 5.3). We plot in Figure 5.3 the negative of the total current ($-J_{\text{tot}}$) calculated by each approach since $-J_{\text{tot}}$ is what is typically reported in the literature for CELIV transients [39, 121, 120, 126, 65, 151]. Because the drift-diffusion simulations use a different starting formalism than Eq. (5.13), the fact that the two results agree precisely verifies the legitimacy and generality of our derivation. Furthermore, as also highlighted in the ToF Section, this shows that Eq. (5.13) and Eqs. (5.25) and (5.26) can be combined to examine the materials-related aspects of these transients.

In addition to the negative of the total current, Figure 5.3 also shows the negative of each component of Eq. (5.13). The current due to the changing electrode charge runs in the opposite direction for this case because CELIV involves a reverse-bias voltage ramp. The carrier concentrations decrease in time due to recombination, sweep-out/diffusion, and sur-

Parameter	Symbol	Value
Electron,Hole Mobility	μ_n,μ_p	1×10^{-4} cm^2/V–s
Active Layer Thickness	d	100 nm
Relative Permittivity	ϵ_r	3.5
Injection Barriers	ϕ_n, ϕ_p	0.3 eV
Langevin Reduction Factor	γ	0.1
Built-in Voltage	V_{BI}	0.6 V
Effective Density of States	$N_{\text{C}}, N_{\text{V}}$	1×10^{20} cm^{-3}
Temperature	T	298 K
Band Gap	E_g	1.2 eV

Table 5.1: Parameters used in the drift-diffusion photo-CELIV simulation; the values chosen are designed to roughly simulate an organic photovoltaic device

face recombination current, and therefore the derivative of the average carrier concentrations are also negative. Since generation only takes place initially and is set to zero afterwards, only recombination contributes to the $qd\langle R - G\rangle$ term in Eq. (5.13), which registers as a positive current density in our sign convention.

Finally, it is worth noting that the J_{surf} term is rather large and positive in the initial part of the transient in Figure 5.3, corresponding to net carrier extraction at the 'wrong' contacts. The reason for such a large value of this current density is that the cell is initially held at a forward bias equal to the built-in potential until the start of the CELIV ramp. At this applied bias, the built-in electric field is entirely canceled, and thus a significant amount of excess carriers get collected at the 'wrong' contact by way of diffusion. Real, well-working, devices are designed to avoid this problem by having higher built-in potentials and/or blocking layers to prevent extraction of carriers by the 'wrong' contact.

All in all, Figure 5.3 verifies that our formalism provides another level of insight into current transient measurements that is fully consistent with detailed time-domain numerical drift-diffusion modeling. The benefit of our approach, though, is that it pairs the generality of a full numerical calculation with the physical insight of a analytical model. With these tools at hand, researchers can now understand any current transient measurement in terms of a simple set of discrete physical processes.

5.5 Conclusions

In summary, we have derived a generalized equation for describing current transients in planar optoelectronic devices at uniform temperature. Our results detail all the possible sources of current using only fundamental physical equations and spatially-averaged values of the quantities/processes of interest. Integrating our generalized current-density equation provides further insight on how to interpret the apparent charge extracted from transient current measurements, including how to account for changes in charge on the electrodes. One unexpected result from this analysis is a factor of one-half reduction in the apparent extracted charge due to non-intuitive displacement current effects. We have shown how this factor of one-half, along with an improper accounting of the electrode charge, has lead to misinterpretations of charge-extraction transients in the organic solar cell literature. We further demonstrated how readily a simple physical picture—like that of the classic CELIV and ToF models—can be translated into an expression for the total measured current density as a function of time using our set of simple generalized equations. Finally, we have shown that the derived relations are effectively built into time-domain drift-diffusion numerical solvers, thus verifying the correctness of our approach while demonstrating a new avenue for understanding current transients in 1-D optoelectronic devices.

APPENDIX A

Supplemental Material for: Drift-Diffusion Modeling of the Effects of Structural Disorder and Carrier Mobility on the Performance of Organic Photovoltaic Devices

A.1 Cahn-Hilliard Generated Morphologies

In order to obtain an alternative description of the semi-random distribution of low and high carrier mobilities, we utilize 1D slices through disordered morphologies generated by solving the Cahn-Hilliard equation on a 2D grid. The Cahn-Hilliard equation:

$$\frac{\partial C}{\partial t} = D\nabla^2(C^3 - C - \epsilon\nabla^2 C) \tag{A.1}$$

describes the spontaneous phase separation of a binary fluid mixture, where C is the spatial composition of the fluid mixture that ranges from one pure component to the other ($C(x, y) \in [-1, 1]$). In this equation, D is the diffusivity and ϵ is the interfacial interaction energy between the two components. Since our primary interest in Cahn-Hilliard morphologies is the semi-random distribution of phases at differing length scales, we assume D=1 and instead only vary the interaction energy. Since the interaction energy determines the average domain size of the resulting morphologies, this single parameter allows us to simulate bulk heterojunction morphologies of varying feature size. We employ David Eyre's linearly stabilized Cahn-Hilliard integration scheme[50, 17] to solve the Cahn-Hilliard equation on a 2D grid (See Fig. A.1). These morphologies result in compositional maps that vary from -1 to 1 over various length scales. We then utilize 1D cross sections through these morphologies to generate mobility profiles characterized by high and low mobility regions. When generating

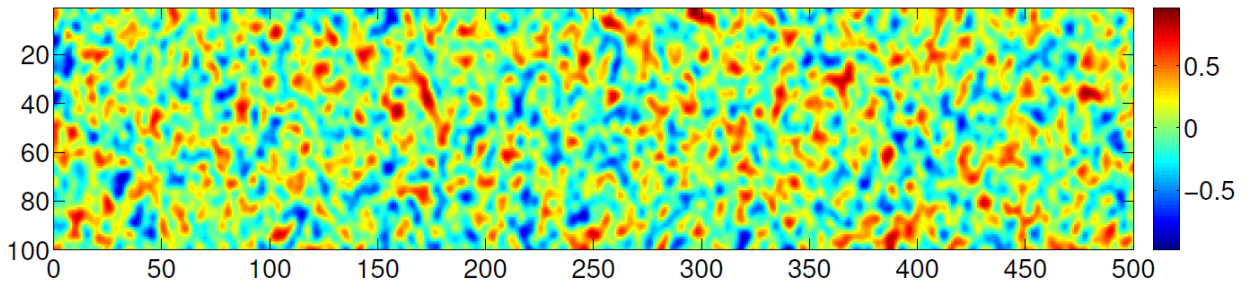

Figure A.1: An example of a morphology generated by solving the Cahn-Hilliard equation on a 100x500 nm grid.

mobility profiles from cross-sections of our C-H morphologies, we intentionally sample only every 20$^{\text{th}}$ cross-section to reduce any correlation between replica mobility profiles, since adjacent cross-sections are likely to be of similar composition. The effects of the mobility range parameter, σ_{CH}, on the figures of merit are plotted in the main text. In Fig. A.2, we show the effects of the average feature size, δ_{CH} on device performance. Similar trends are shown as with the randomly sampled ensembles, with J_{SC}, *FF*, and *PCE* all negatively impacted, but V_{OC} unaffected. For smaller average feature sizes, there appears to be a reversal in the trend of diminished performance of J_{SC}, *FF*, and *PCE* that is not present in randomly sampled ensembles. We attribute this to the fact that δ_{CH} is only an average feature size and, as such, an appreciable number of sampled mobility profiles may actually have domain sizes larger than this average feature size. This would result in a mobility profile with performance comparable to coarser devices, (i.e., larger δ_{CH}), and these mobility profiles are sufficient to reverse the trend of lower performance for smaller feature sizes. The distributions of one such Cahn-Hilliard sampled ensemble are shown in Fig. A.3. They illustrate skewed distributions which are similar to the randomly sampled distributions illustrated in the main text.

A.2 Mobility Profiles, Discretization, Mesh Size, and Accuracy

Care must be taken when discretizing the charge carrier continuity equations in the main text (Eqs. (3) and (4)) via the finite difference approximation. The simple assumption that the charge density varies linearly between mesh points can result in a solution with negative

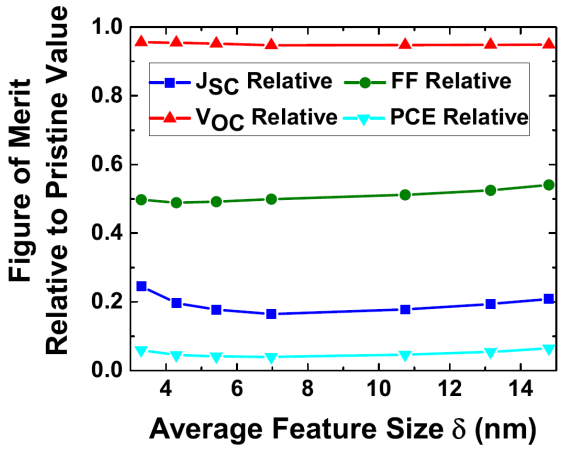

Figure A.2: Relevant figures of merit for the ensemble averaged J–V characteristics as a fraction of the pristine device's but as the average feature size, δ_{CH}, of the sampled Cahn-Hilliard morphologies is increased from approximately 3 to 15 nm.

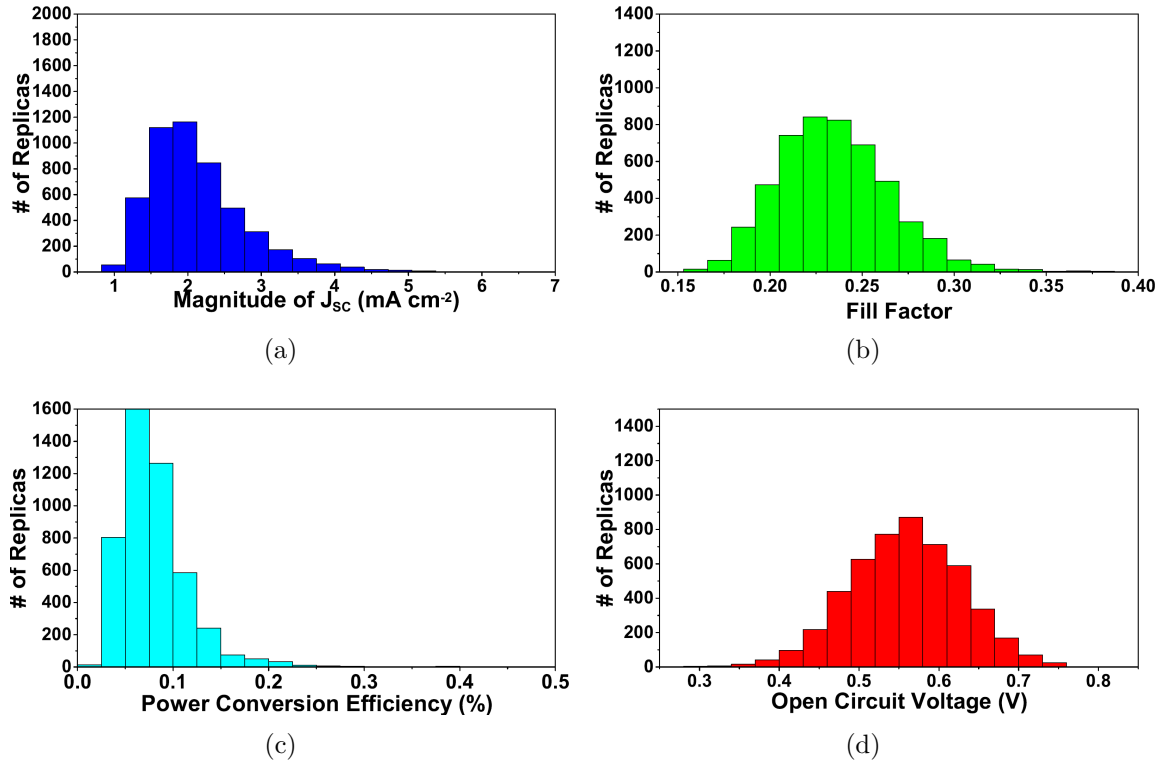

Figure A.3: Histograms showing the distribution of replicas from an ensemble of devices generated via Cahn-Hilliard sampling with $\mu_{CH} = -8.0$, $\sigma_{CH} = 2.0$, and $\delta_{CH} \approx 3.3$ nm

charge densities [162], which is unphysical. Therefore, it is typical to assume a nonlinear variation of charge density between mesh points via the Scharfetter-Gummel discretization scheme, which we employ [147]. An assumption of this discretization scheme is that the mobility is constant between mesh points. Typically, when a simulation calls for the mobility to vary between mesh points i and $i+1$, it is assumed that the mobility between mesh points is simply the algebraic mean of μ_i and μ_{i+1}, an assumption that we also employ. This can potentially lead to numerical errors when the mobility changes drastically, which is potentially the case with our randomly sampled mobility profiles. To test the severity of this approximation, we also simulate our randomly sampled mobility profiles with finer mesh point spacing, in order to hopefully reduce the numerical errors of drastic changes in mobility between mesh points. We tested mesh spacings of $\Delta x = 1$ nm to $\Delta x = 0.05$ nm for an ensemble characterized by $\mu_{\mathrm{RS}} = -8.0$, $\sigma_{\mathrm{RS}} = 0.7$, and $\delta_{\mathrm{RS}} = 3$ nm. We then determined any discrepancies between coarser mesh spacings and very fine mesh spacings. The results are depicted in Fig. A.4. We find that with our original mesh spacing of $\Delta = 1$ nm, the discrepancies for all figures of merit (J_{SC}, *FF*, V_{OC} and *PCE*) are less than 3 percent. Therefore, we believe that the drift-diffusion equations can still be properly solved via the Scharfetter-Gummel discretization scheme, even with our structurally disordered mobility profiles.

A.3 Ensemble Mobility Distributions

We utilize two methods to generate structurally disordered mobility profiles: one where a mobility value is randomly sampled from a normal distribution every δ nm, and another where cross sections of Cahn-Hilliard morphologies are sourced while varying the mobility of a 1D device replica around a mean μ_0 mobility by several orders of magnitude. The distributions of the sampled mobilities of the profiles generated by these two methods vary greatly and are illustrated in Fig A.5. The first method (Fig. A.5(a)) is clearly normally distributed since the original sampling distribution is normally distributed, with most mobility values clustered around the mean mobility value, μ_0, with only a few mobilities sampled near 10^{-10}

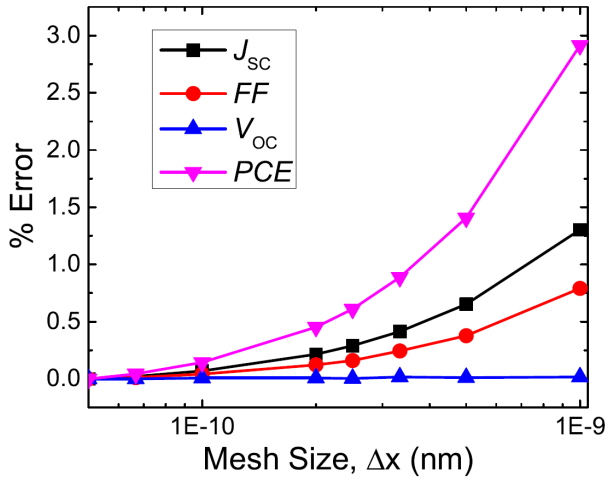

Figure A.4: The effects of finer mesh point spacing on the accuracy of the ensemble average device figures of merit are illustrated. It is assumed that the smallest mesh spacing ($\Delta x = 0.05$ nm) is the most accurate. The discrepancy between the performance of coarser meshes ($\Delta x > 0.05$ nm) is plotted as a function of mesh size. This ensemble was characterized by $\mu_{\mathrm{RS}} = -8.0$, $\sigma_{\mathrm{RS}} = 0.7$, and $\delta_{\mathrm{RS}} = 3$ nm.

and 10^{-6} m^2 V^{-1} s^{-1}. The second method results in a mobility distribution that is nearly opposite in character to the first, with the majority of mobilitiy values clustered at the extreme end of the distribution range (also 10^{-10} to 10^{-6} m^2 V^{-1} s^{-1}), with comparatively few mobilities sampled near the mean mobility, μ_0. However, as described in the main text, these distributions result in very similar ensemble averaged behavior, suggesting that the range of possible mobilities has a greater effect on device performance than the exact shape of the distribution that such mobilities are sampled from.

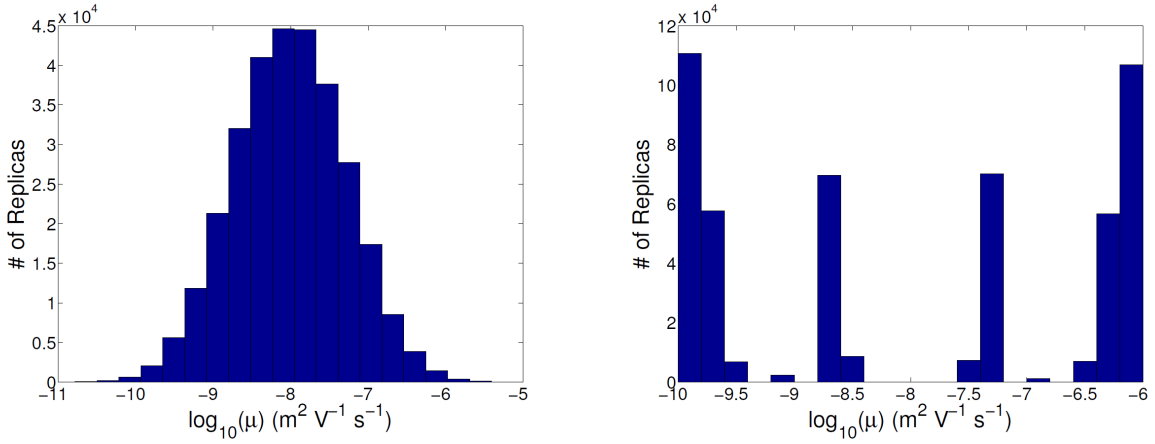

(a) (b)

Figure A.5: (a) Histogram depicting the distribution of mobilities from an ensemble of devices sampled from a mobility distribution characterized by $\mu_0 = -8.0$, $\sigma = 0.7$, and $\delta = 3$ nm. (b) Histogram depicting the distribution of mobilities from an ensemble of devices generated by taking 1D cross-sections of Cahn-Hilliard morphologies with average feature size $\delta \approx 3.3$ nm, with mobilities centered around $\mu_0 = -8.0$ and ranging by $\sigma = 2.0$ orders of magnitude about that mean.

APPENDIX B

Supplemental Material for: Do Organic Photovoltaics Really Need a Mixed Phase? Drift-Diffusion Studies of the Effect of Bulk Heterojunction Compositional Morpholog on Optimum Device Performance

B.1 Full J–V Characteristics of Simulated Devices

In this study, we are primarily interested in the effects of a mixed-phase region on OPV device performance. In order to measure an OPV's power conversion efficiency, one must measure its J–V characteristic under illumination. There are three points along this J–V characteristic which determine the device's power conversion efficiency: the short-circuit current (J_{SC}), the open-circuit voltage (V_{OC}), and the *FF*. These are the only points along the J–V curve that are necessary to determine the device's performance capabilities. Thus the full J–V characteristics of our simulated devices were omitted from the main text for the sake of brevity. In Fig. B.1, we present the full J–V characteristics of our five Cahn-Hilliard generated morphologies and the HAADF-STEM determined morphology.

B.2 Spatially Resolved Simulation Results (C, n, and $J_{n,y}$ at Additional Morphological Length Scales

The main text presents, for a single morphology, several spatially resolved device observables, such as the electron density and electron current density, determined from simulation, at varying degrees of mixing. The main text only presented these observables for one mor-

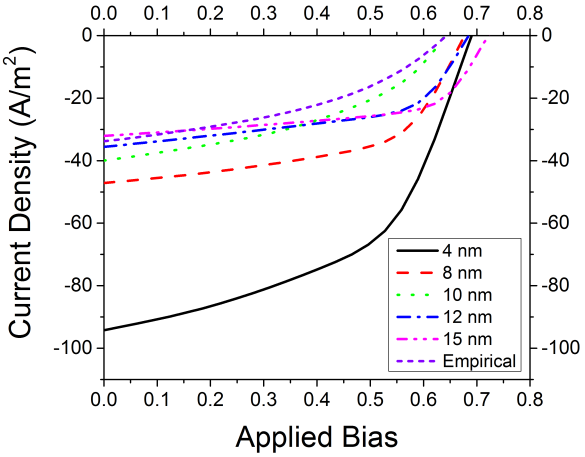

Figure B.1: Full J–V characteristics of the all of the initial, non-mixed morphologies studied in the main text. The first 5 curves refer to morphologies generated by Cahn-Hilliard modeling of binary fluid separation while the last curve is from an empirical morphology determined by high-angle annular dark-field scanning transmission electron microscopy (HAADF-STEM).

phological length scale (10 nm) for the sake of brevity. In Figs. B.2 and B.3 we present the compositional morphology, the electron density, and the y-component of the electron current density vector for the smallest and the largest morphological length scales examined (4 nm and 15 nm). These observables are presented for these morphologies in their non-mixed state as well as at $\sim 30\%$ and $\sim 70\%$ mixing.

B.3 Effects Alternative Mixing Method

As mentioned previously in the main text, there are technically two methods to introduced a mixed region into the device: either by smoothing the input device morphology first before mapping to the charge carrier mobilities, or by mapping the mobilities first before subsequently smoothing the mobility profiles. The two methods produce decidedly different carrier mobility profiles, which in turn results in different device performance. Consider a simulation in which the mobility of electrons in the fullerene phase is 1×10^{-7} m^2 V^{-1} s^{-1} and 1×10^{-12} m^2 V^{-1} s^{-1} in the polymer phase. The device's compositional morphology, C, should vary between 0 and 1 and the composition of the mixed-phase region should be ap-

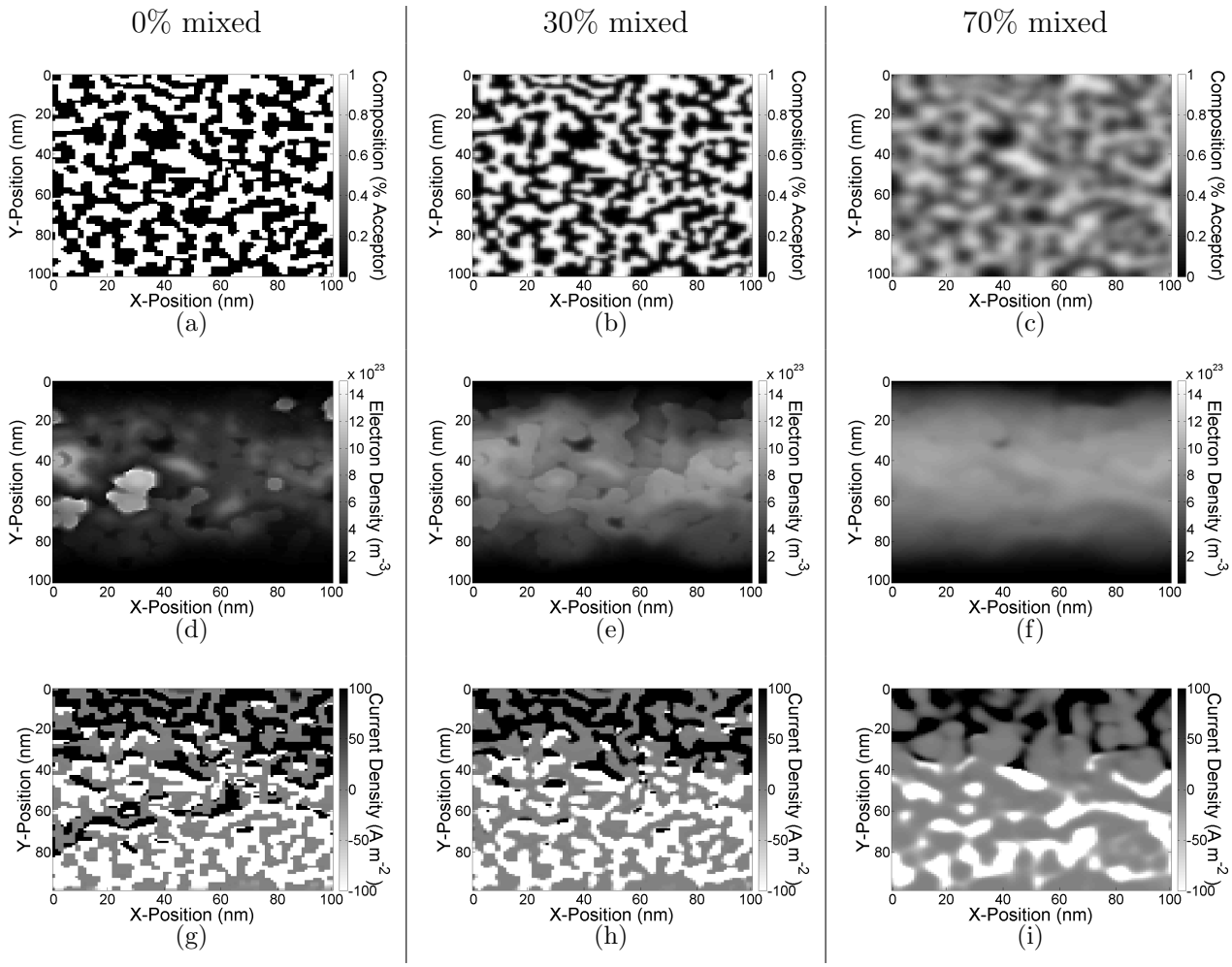

Figure B.2: Simulation results of OPV devices based on C-H morphology (average feature size of ~ 4 nm) with a controllably increasing amount of intermixed compositional regions from left (no intermixing) to right (most intermixing). All figures represent the device at short-circuit conditions under simulated AM1.5 illumination. Panels (a)-(c): overall compositional morphology; panels (d)-(f): spatially-dependent electron density; panels (g)-(i): electron current density profile. Each of these image plots shows a 100 nm $\times$ 100 nm subsection of the entire simulated device. The ITO/PEDOT:PSS anode and the calcium cathode are located at the top and bottom of each plot, respectively.

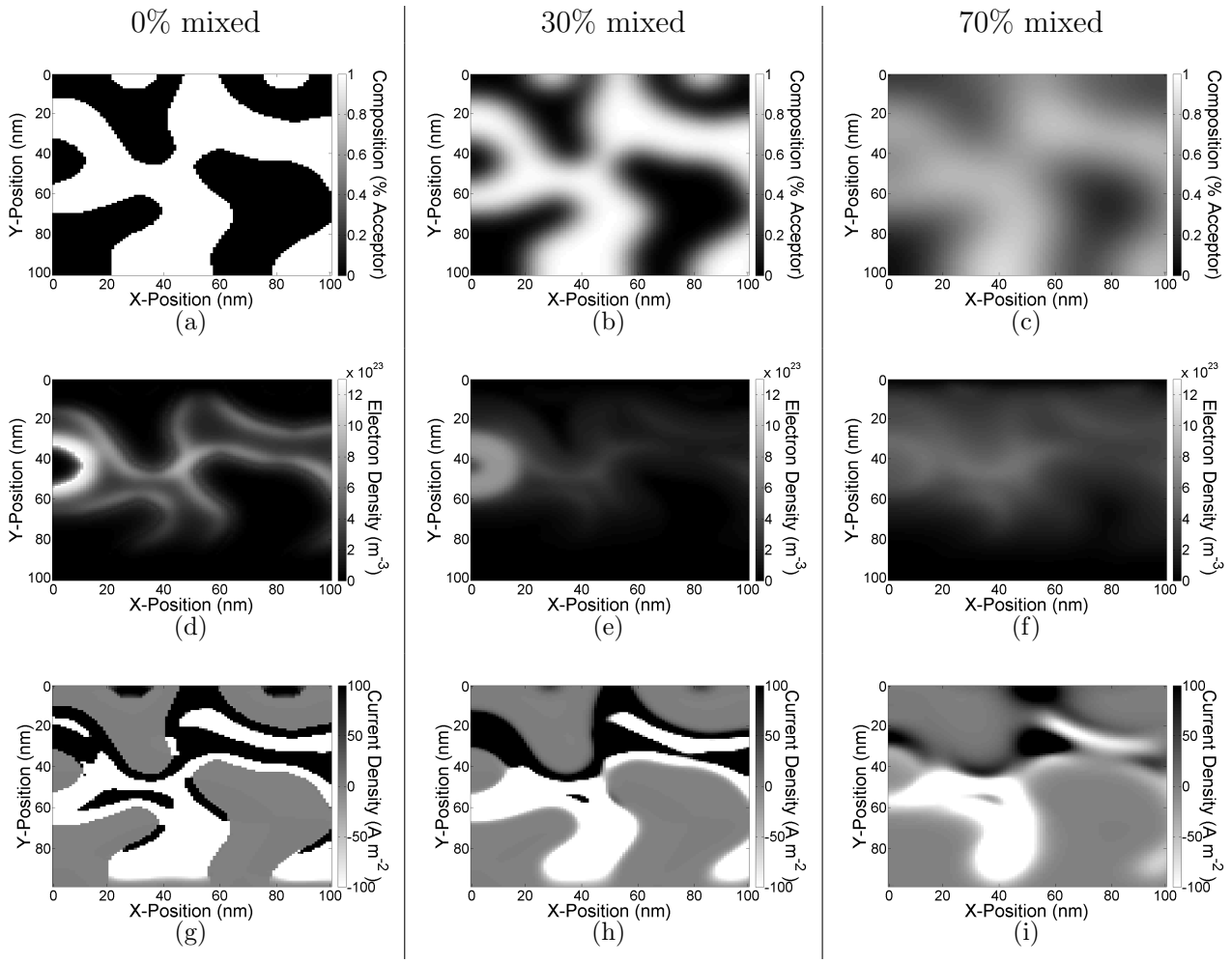

Figure B.3: Simulation results of OPV devices based on C-H morphology (average feature size of ~ 15 nm) with a controllably increasing amount of intermixed compositional regions from left (no intermixing) to right (most intermixing). All figures represent the device at short-circuit conditions under simulated AM1.5 illumination. Panels (a)-(c): overall compositional morphology; panels (d)-(f): spatially-dependent electron density; panels (g)-(i): electron current density profile. Each of these image plots shows a 100 nm $\times$ 100 nm subsection of the entire simulated device. The ITO/PEDOT:PSS anode and the calcium cathode are located at the top and bottom of each plot, respectively.

proximately 0.5, since the Gaussian smoothing operations averages the compositional values of the pure regions. Using the first method of mixing (Gaussian smoothing before mapping to mobility) will thus result in a mobility in the mixed region of $\sim 3.16 \times 10^{-10}$ m^2 V^{-1} s^{-1}. The second method (mapping to mobility followed by Gaussian smoothing) instead generates a mixed-phase region with a mobility that is approximately the average of the mobilities in the pure region. Therefore, this method results in a mixed region with a mobility of $\sim 0.5 \times 10^{-7}$ m^2 V^{-1} s^{-1}.

It is not immediately clear which method is more physically representative of the mixed-phase in actual OPV devices. We rationalize that the charge carrier mobility in the mixed-phase region should be significantly lower than the mobility in the pure, conducting phase, since the mixed-phase region is inherently amorphous and possess higher energetic disorder. The mixed-phase also contains non-conducting material, which should lower the mobility by several orders of magnitude. Therefore, we have chosen the first mixing method (smoothing the compositional morphology before mapping the mobilities) for our investigation of the effects of a mixed-phase on device performance. To further illustrate that these two approaches produces quantitatively different results, we also performed several simulations with the alternative method. The results of these calculations are presented in Fig. B.4. This figure plots the figures of merit (J_{SC}, V_{OC}, FF, and power conversion efficiency) for our 10-nm device as a the fraction of their values in a non-mixed configuration.

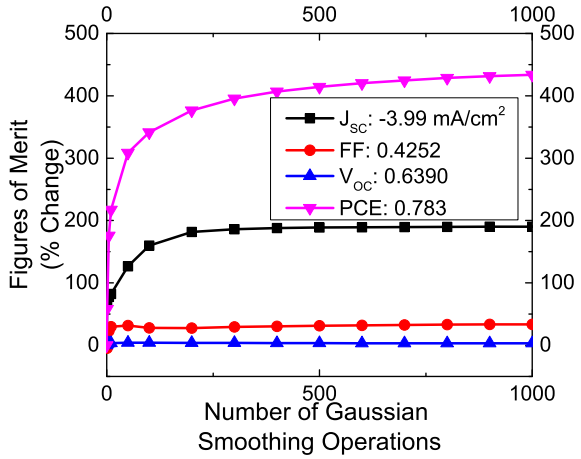

Figure B.4: This figure illustrates the effect of a mixed-phase on the device performance of our 10-nm Cahn-Hilliard morphology when using an alternate method of mixing (i.e. mapping morphology to mobility and then smoothing the mobility profiles).

APPENDIX C

Supplemental Material for: Theory of Current Transients in Planar Semiconductor Devices: Insights and Applications to Organic Solar Cells

C.1 Derivation of the Spatially Constant Total Current

In order to show that the total current is spatially constant, we must demonstrate that the spatial derivative of Eq. (4) in the main text is equal to zero:

$$\frac{dJ_{\text{tot}}}{dx} = \frac{dJ_n}{dx} + \frac{dJ_p}{dx} + \frac{dJ_{_D}}{dx} = 0. \tag{C.1}$$

Fortunately, a straightforward rearrangment of the continuity equations (Eqs. (1) and (2) in the main text) gives two of the terms we need:

$$\frac{dJ_n}{dx} = q\frac{dn}{dt} - q(G-R) - q(G_e^D - R_e^D + G_e^A - R_e^A)$$
$$\frac{dJ_p}{dx} = -q\frac{dp}{dt} + q(G-R) + q(G_h^D - R_h^D + G_h^A - R_h^A). \tag{C.2}$$

We can then take the time derivative of Gauss' law and use the non-averaged (local) versions of Eqs. (11) and (12) in the main text to obtain the following expression for the spatial derivative of the displacement current:

$$\frac{dJ_{_D}}{dx} = q\frac{dp}{dt} - q\frac{dn}{dt} + q(G_e^D - R_e^D + G_e^A - R_e^A) - q(G_h^D - R_h^D + G_h^A - R_h^A). \tag{C.3}$$

Clearly, the sum of the right-hand-sides of Eqs. (S2-4) is exactly zero, demonstrating that the total current is spatially constant at each instant in time, as discussed in the main text.

C.2 Relating the Charge on the Contacts to the Voltage

We can solve for the charge on the electrodes and thus σ_{EL} by recognizing that the electric field within the device can be written as:

$$E(x) = \frac{1}{2\epsilon}\int_0^x \rho(\acute{x})d\acute{x} - \frac{1}{2\epsilon}\int_x^d \rho(\acute{x})d\acute{x} + \frac{\sigma_{\text{EL}}}{2\epsilon}$$
$$= \frac{1}{\epsilon}\int_0^x \rho(\acute{x})d\acute{x} - \frac{\bar{\rho}d}{2\epsilon} + \frac{\sigma_{\text{EL}}}{2\epsilon}$$
$$\rho(x) = q[p(x) - n(x) + N_D^+(x) - N_A^-(x)], \quad \text{(C.4)}$$

where $E(x)$ is the electric field in the active layer, q is the electron charge, $\bar{\rho}d = \int_0^d \rho(x)\,dx$, and $\acute{x}$ is a dummy variable for spatial integration. Integrating Eq. (B2) from $x = 0$ to d gives the total electric potential drop ($V = -\int_0^d E\,dx$) across the active layer:

$$V = \frac{\bar{\rho}d^2}{2\epsilon} - \frac{\sigma_{\text{EL}}d}{2\epsilon} - \frac{1}{\epsilon}\int_0^d\int_0^x \rho(\acute{x})d\acute{x}\,dx. \quad \text{(C.5)}$$

Eq. (C.5) provides the relationship between the electric field supplied by the electrode charge, the electric potential, and the space-charge distribution within the active layer. If desired, one can use Eq. (B4) with $\sigma_0 + \sigma_d = -\bar{\rho}d$ and $\sigma_{\text{EL}} = \sigma_0 - \sigma_d$ to solve for the charge on each electrode, σ_0 and σ_d, in terms of ρ and V. Solving for σ_{EL} then gives the following useful relations:

$$\sigma_{\text{EL}} = \bar{\rho}d - \frac{2\epsilon V}{d} - \frac{2}{d}\int_0^d\int_0^x \rho(\acute{x})d\acute{x}\,dx \quad \text{(C.6)}$$

$$E_{\text{EL}} = \frac{\bar{\rho}d}{2\epsilon} - \frac{V}{d} - \frac{1}{\epsilon d}\int_0^d\int_0^x \rho(\acute{x})d\acute{x}\,dx \quad \text{(C.7)}$$

$$V_{\text{EL}} = \frac{\bar{\rho}d^2}{2\epsilon} - V - \frac{1}{\epsilon}\int_0^d\int_0^x \rho(\acute{x})d\acute{x}\,dx, \quad \text{(C.8)}$$

where V_{EL} is the electric potential drop due to the electrode charge, E_{EL} is the electric field supplied by the electrode charge, and $V = V_{\text{app}} - V_{\text{BI}}$ is the electric potential drop across the active layer. Also, here V_{app} is the applied bias and V_{BI} is the constant built-in potential due to, e.g., permanent asymmetric carrier concentrations at the contacts, compositional gradients, etc. Thus, from Eq. (C.6), $d\sigma_{\text{EL}}/dt$ is non-zero only if the space-charge density distribution $\rho(x)$ and/or the applied bias V_{app} are changing in time. If desired, σ_{EL} can be eliminated by combining Eqs. (C.5) and (C.4) to give the general equation

$$E(x) = \frac{1}{\epsilon}\left(\int_0^x \rho(\acute{x})d\acute{x} - \frac{1}{d}\int_0^d \int_0^x \rho(\acute{x})d\acute{x}\,dx\right) - \frac{V}{d}, \tag{C.9}$$

where again V is the electric potential drop across the active layer, which is related by the total applied bias by $V = V_{\text{app}} - V_{\text{BI}}$. If the dielectric environment is inhomogeneous, then $\epsilon \to \epsilon(\acute{x})$ and is absorbed into the integrals of Eq. (C.9).

C.3 Drift Diffusion Model

The drift-diffusion model is a continuum approach that can be derived from the Boltzmann transport equation. The model states that the charge carrier current densities, $J_{n,p}$, can be expressed as (also see Eqs. (25) and (26) in the main text):

$$J_n = -qn\mu_n\nabla\psi + \mu_n kT\nabla n \tag{C.10}$$

$$J_p = -qp\mu_p\nabla\psi - \mu_p kT\nabla p \tag{C.11}$$

where n and p refer to electrons and holes, ψ is the electrostatic potential, q is the fundamental charge, $\mu_{n,p}$ are the electron and hole mobilities, k is the Boltzmann constant, and T is the temperature. The current densities have two components: a drift term, which arises from carriers moving in response to an electric field, and a diffusion term, which arises from the presence of carrier density gradients. In order to fully model an electronic device, one

must solve the carrier continuity equations (also Eqs. (1) and (2) in the main text):

$$\frac{\partial n}{\partial t} = \frac{1}{q}\nabla \cdot J_n + G - R \tag{C.12}$$

$$\frac{\partial p}{\partial t} = -\frac{1}{q}\nabla \cdot J_p + G - R \tag{C.13}$$

where G is the carrier generation rate and R is the carrier recombination rate. The continuity equations take account for all loss and gain mechanisms relevant to the device being modeled. Note that these equations, which were used in the numerical solver, do not include trapping and de-trapping terms like the more general continuity equations presented in the text. In any case, though, to relate the carrier densities to the electrostatic potential distribution, one must couple the above equations to the Poisson equation:

$$\nabla^2\psi = \frac{q}{\epsilon}(n - p + N_{\text{A}}^- - N_{\text{D}}^+) \tag{C.14}$$

where $\epsilon = \epsilon_0\epsilon_r$ and ϵ_0 and ϵ_r are the vacuum and relative permittivities, respectively, and N_{A}^- and N_{D}^+ are the localized charge densities as defined in the text. The set of equations (C.12)-(C.14) must be solved in order to fully simulated a device [163].

C.4 Numerical methods and Solution Details

C.4.1 Boundary Conditions

The above Eqs. (C.12)-(C.14) represent a set of 3 second order partial differential equations with three independent variables (n, p and ψ). Thus we require six boundary conditions, two for each independent variable. For the charge carrier densities, we assume thermionic injection conditions at the electrode contacts, which are treated as Schottky contacts [150, 144]. Under these conditions, the carrier densities at the contacts is assumed to be constant and is set to, for example,

$$n(0) = N_{\text{C}} \cdot \exp\left(-\frac{\Phi_{\text{B,anode}}}{kT}\right) \tag{C.15}$$

where $\Phi_{\mathrm{B,anode}}$ is the height of the Schottky barrier at the anode contact and N_{C} is the effective density of states of the conduction band. An analogous expression is implemented at both contacts for both electrons and holes. As for the electrostatic potential, we assume that the total potential change through the device should be equal to the built-in potential of the device, which we set to 0.6 V.

C.4.2 Generation and Recombination

Two of the most important factors in device simulation—and of particular importance for OPV devices—are the generation and recombination terms in eqs (C.12) and (C.13). To ensure physically representative data for an OPV device, one must choose appropriate generation and recombination mechanisms. First, we assume that the spatial generation rate inside the device should follow the absorption profile of the active layer. Unfortunately, because of the arrangement of thin films within a typical OPV device, complex interference patterns arise that result in a complex absorption profile rather than a typical Beer's law type exponential decay. Thus, we use a transfer matrix formalism to calculate a generation ($G(x)$) profile that properly accounts for thin film interference patterns within the active layer [135]. We do not consider exciton dynamics and instead assume that an absorbed photon immediately generates a pair of free electrons and holes with a finite efficiency that is independent of, e.g., electric field. For recombination we assume Langevin-type bimolecular recombination statistics for which $R = qnp(\mu_n + \mu_p)/\epsilon$. We don't consider any recombination with traps as this extra detail introduces significant complexity, and we are more focused on how the total measured current can be broken down into a several intuitive terms (Eq. (13) in the text) and to test the validity of the formalism.

C.4.3 Solution Scheme

Using our own in-house code, we implement the Gummel method, by which Eqs. (C.12)-(C.14) are decoupled and solved in an iterative manner. Using a finite difference scheme, we discretize the partial differential equations and solve for n, p and ψ on 1-D meshes.

The discretization of the semiconductor equations results in a set of algebraic equation for every mesh point. Using our own homemade MATLAB® code, we solve this set of algebraic equations by utilizing the open source, linear algebra C++ library Eigen. Once we have solved for these three independent variables, we may extract whatever information we wish (current densities, recombination rates, etc.) In particular, we are able to explicitly calculate the terms of Eq. (13) in the main text.

C.4.4 Transient Simulations

In order to model current transients, we must forgo the usual steady-state approximation ($\partial n/\partial t = \partial p/\partial t = 0$). Starting from a converged, steady-state solution for n, p, and ψ, we iterate the continuity equations forward in time. In order to improve numerical stability, we use an implicit method rather than an explicit approach to iterate through time steps [163]. A detailed outline of the exact method we used can be found in Ref. [163].

In order to simulate a typical photo-CELIV experiment, we begin with a steady-state solution for the device, without illumination, near its V_{OC}. We then generate an excess of free carriers by "turning on" the generation profile for a short time (0.1 μs). After some time has passed (5 μs), during which some carriers recombine, we sweep out the remaining carriers by applying a voltage ramp at the contacts. Voltage ramp that is linear with time, in keeping with normal CELIV operation. The continuity equations are iterated forward in time using an implicit method and the carrier densities and potential distribution recorded at every time step. The carrier densities and potential distribution are then used to calculate the current densities (Eqs. C.10 and C.11) and the time-dependent displacement current:

$$J_{D} = \epsilon \frac{\partial E}{\partial t} = -\epsilon \frac{\partial}{\partial t} \frac{\partial \psi}{\partial x} \tag{C.16}$$

The total measured current in the device is then just (Eq. (4) in main text):

$$J_{\mathrm{tot}} = J_n + J_p + J_{D} \tag{C.17}$$

This total measured current is then compared to the our new analytic expression for the total current(Eq. (13)). Because the three independent variables (n, p, and ψ) are recorded at all time steps, it is trivial to calculate every term in Eq. (13) in the main text.

APPENDIX D

Methodology for Solving Semiconductor Equations

As was discussed in Chapter 1 of this dissertation, performing a drift-diffusion model simulation involves solving the basic semiconductor equations: the electron and hole carrier density continuity equations and the Poisson equation. The three partial differential equations rarely have closed form solutions, and so must be solved numerically. This researcher utilized the finite difference method to discretize the semiconductor equations on a 2-D mesh. With the finite difference method, derivatives of functions are approximated as:

$$\frac{\partial f}{\partial x} \approx \frac{f_{i+1} - f_i}{\Delta x_i} \tag{D.1}$$

$$\frac{\partial^2 f}{\partial x^2} \approx \frac{f_{i+1} - 2f_i - f_{i-1}}{(\Delta x_i)^2} \tag{D.2}$$

where f_i is equal to $f(x)$ at the ith mesh point and Δx_i is the mesh spacing at ith mesh point. The finite difference method turns partial differential equations into a set of algebraic equations. In the most current version of our simulator software, we utilize only constant mesh spacings, typically with a value of 1 nm. Once the semiconductor equations are discretized, they are solved sequentially and iteratively until a converged solution is attained. This particular approach to solving the semiconductor equations is known as the Gummel method.[58]

Several specific issues arise when applying the finite difference method to the semiconductor equations. One problem that comes into play for simulations like ours is the validity of one of the key assumptions of the finite differences approximation, which is that the value of $f(x)$ varies linearly between i and $i+1$. For some semiconductor devices and in particular for the devices examined in this dissertation (organic photovoltaics), this assumption may

not be accurate at the mesh spacings utilized (∼1 nm). The assumption that $f(x)$ varies linearly can potentially lead to negative charge densities.[162] Consider a 1-D device at zero applied bias and with zero current such that:

$$J_{n_x} = -qn\mu_n \frac{\partial V}{\partial x} + qD_n \frac{\partial n}{\partial x} = 0 \tag{D.3}$$

This is merely the drift-diffusion equation of electrical current. The diffusion constant, D_n, is equal to $\frac{kT}{q}\mu_n$, according to the Einstein relationship. If one assumes a discretization scheme with linear interpolation of device variables between i and i+1, this equation may be rewritten as:

$$n_{i+1/2} \times \mu_{n_{i+1/2}} \times \frac{V_{i+1} - V_i}{\Delta x} = D_{n_{i+1/2}} \times \frac{n_{i+1} - n_i}{\Delta x} \tag{D.4}$$

where $n_{i+1/2}$, $\mu_{n_{i+1/2}}$, and $D_{n_{i+1/2}}$ may be obtained by linearly interpolating between the values of the variables at i and $i+1$. Substituting in $\frac{n_{i+1}+n_i}{2}$ for $n_{i+1/2}$ and using the Einstein relationship, the above equation becomes:

$$V_{i+1} - V_i = \frac{2kT}{q} \frac{n_{i+1} - n_i}{n_{i+1} + n_i} \tag{D.5}$$

Since charge carrier densities must be positive to be physically meaningful, the above equation requires that:

$$V_{i+1} - V_i \leq \frac{2kT}{q} \tag{D.6}$$

This implies that if the difference between the electrostatic potential at adjacent grid point exceeds $\frac{2kT}{q}$, then a linear interpolation scheme will predict negative charge densities, which is unphysical.

The possibility of physically invalid solutions may be accounted for by assuming that the carrier densities vary exponentially between grid points. This approach was first implemented by Scharfetter and Gummel (see their original paper for a full derivation).[147] With such a representation, the charge current density at the mid-point between adjacent mesh points may be expressed as:

$$J_{n_{x_{i+1/2}}} = -\frac{qD_n}{\Delta x}\left\{n_{i+1}B\left[\frac{q}{kT}(V_{i+1}-V_i)\right] - n_iB\left[\frac{q}{kT}(V_i-V_{i+1})\right]\right\} \tag{D.7}$$

Where $B(x)$ is the Bernoulli equation and is defined as:

$$B(x) = \frac{x}{e^x - 1} \tag{D.8}$$

A similar expression exists for the hole current density, such that:

$$J_{p_{x_{i+1/2}}} = -\frac{qD_p}{\Delta x}\left\{p_{i+1}B\left[\frac{q}{kT}(V_i-V_{i+1})\right] - p_iB\left[\frac{q}{kT}(V_{i+1}-V_i)\right]\right\} \tag{D.9}$$

With these expressions for the current density, the continuity equations may be properly discretized.

In two-dimensions, at steady-state conditions ($\frac{\partial n}{\partial t} = \frac{\partial p}{\partial t} = 0$) the electron continuity equation may be expressed as:

$$\begin{aligned} n_{i,j-1}\cdot D_{n_{i,j-1/2}}\cdot B\left(\frac{V_{i,j-1}-V_{i,j}}{V_T}\right) + n_{i-1,j}\cdot D_{n_{i-1/2,j}}\cdot B\left(\frac{V_{i-1,j}-V_{i,j}}{V_T}\right) \\ - n_{i,j}\cdot\left[D_{n_{i,j-1/2}}B\left(\frac{V_{i,j}-V_{i,j-1}}{V_T}\right) + D_{n_{i-1/2,j}}B\left(\frac{V_{i,j}-V_{i-1,j}}{V_T}\right)\right. \\ \left. D_{n_{i,j+1/2}}B\left(\frac{V_{i,j}-V_{i,j+1}}{V_T}\right) + D_{n_{i+1/2,j}}B\left(\frac{V_{i,j}-V_{i+1,j}}{V_T}\right)\right] \\ n_{i,j+1}\cdot D_{n_{i,j+1/2}}\cdot B\left(\frac{V_{i,j+1}-V_{i,j}}{V_T}\right) + n_{i+1,j}\cdot D_{n_{i+1/2,j}}\cdot B\left(\frac{V_{i+1,j}-V_{i,j}}{V_T}\right) \\ = -\frac{1}{(\Delta x)^2}\cdot(G_{i,j}-R_{i,j}) \end{aligned} \tag{D.10}$$

Similarly for the hole continuity equation:

$$\begin{aligned} p_{i,j-1} \cdot D_{p_{i,j-1/2}} \cdot B\left(\frac{V_{i,j} - V_{i,j-1}}{V_T}\right) + p_{i-1,j} \cdot D_{p_{i-1/2,j}} \cdot B\left(\frac{V_{i,j} - V_{i-1,j}}{V_T}\right) \\ - p_{i,j} \cdot \left[D_{p_{i,j-1/2}} B\left(\frac{V_{i,j-1} - V_{i,j}}{V_T}\right) + D_{p_{i-1/2,j}} B\left(\frac{V_{i-1,j} - V_{i,j}}{V_T}\right) \right. \\ \left. D_{p_{i,j+1/2}} B\left(\frac{V_{i,j+1} - V_{i,j}}{V_T}\right) + D_{p_{i+1/2,j}} B\left(\frac{V_{i+1,j} - V_{i,j}}{V_T}\right) \right] \\ p_{i,j+1} \cdot D_{p_{i,j+1/2}} \cdot B\left(\frac{V_{i,j} - V_{i,j+1}}{V_T}\right) + p_{i+1,j} \cdot D_{p_{i+1/2,j}} \cdot B\left(\frac{V_{i,j} - V_{i+1,j}}{V_T}\right) \\ = -\frac{1}{(\Delta x)^2} \cdot (G_{i,j} - R_{i,j}) \end{aligned} \quad \text{(D.11)}$$

Discretizing the Poisson equation is considerably simpler than the continuity equation. The most basic discretized form of the Poisson equation is:

$$V_{i,j-1} + V_{i-1,j} - 4 \cdot V_{i,j} + V_{i,j+1} + V_{i+1,j} = \frac{q}{\epsilon_r \epsilon_0} \cdot (n_{i,j} - p_{i,j} + C) \quad \text{(D.12)}$$

With the semiconductor equations properly discretized, we have now turned the original partial differential equations into a set of algebraic equations where the solutions (n, p, and V) are specified on a 2-D finite difference mesh with constant mesh spacing. As mentioned above, we solve the three semiconductor equations sequentially and iteratively until a converged solution is obtain. The set of algebraic equations may be formulated as a matrix equation. Our software makes extensive use of the Eigen Linear Algebra Libray by Tuxfamily [57] to store the matrix coefficients and solve the set of algebraic equations. We also use the Eigen Library's extensive class library for representing matrices and vectors to store many of the simulation variables. See the Eigen Linear Algebra Library documentation for further information about accessing and manipulating data matrices.

APPENDIX E

Simulation Software Operation and the `DriftDiffusion` class

Our drift-diffusion program is written in the C++ programming language. The source code maybe found on the Benjamin J. Schwartz group Bitbucket repository :https://bitbucket.org/schwartzgroup/driftdiffusionmodeling. It consists of a main program file ("main.cpp"), a single class definition for simulating organic solar cells ("DriftDiffusion.cpp" and "DriftDiffusion.h"), and a collection of header files containing supplementary data for the simulation, such as the AM1.5 spectrum, the complex indices of refraction of several OPV materials, and various other constants ("AM15.h", "RefractiveData.h", and "Constants.h"). Performing a drift-diffusion simulation with our software involves the writing a brief program/script in the "main.cpp" file, followed compiling and running the generated executable file. Composing a simulation script involves the following steps:

1) Instantiating an object of the `DriftDiffusion` class in the `main()` function of the "main.cpp" file. The dimensions of the device object must be specified when instantiating.

2) Specifying device parameters such as carrier mobilities, recombination efficiencies, etc. with the various device parameter manipulation functions (See Sec. E.5).

3) Importing the compositional morphology of device, if performing a 2-D simulation (See Sec. E.2). Morphological data may be either generated from Cahn-Hilliard and Monte Carlo modeling of binary phase separation or by sourcing empirical morphology data.

4) Performing a simulation by calling one of the available simulation functions (See Sec. E.4).

5) Printing any other pertinent simulation data to file with the available set of print statements (See Sec. E.6).

The code itself has been extensively commented to describe the purpose and basic operation of the `DriftDiffusion` class. This appendix is only meant to provide a basic overview of the software's operating principles.

E.1 Device Instantiation and the `DriftDiffusion()` Constructor

An instance of the `DriftDiffusion` class contains all of the dependent variables (n, p, and V), as well the independent variables for the simulation. Instantiating a `DriftDiffusion` object in the `main()` program can be conceptualized as "creating" an organic solar cell. The dimensions of the device (depth and width) must specified in the `DriftDiffusion` object's constructor. For example, the following statement would create a model organic solar cell with an active layer 120 nm thick and 300 nm across:

```
DriftDiffusion mySolarCell(120,300);
```

If no input parameters are passed to the `DriftDiffusion` object's constructor, the dimensions of the of the device are assumed to be (100,1). This creates a 1-dimensional organic solar cell with an active layer 100 nm thick. Upon instantiating, the constructor appropriately re-sizes the spatially dependent variables and parameters, sets the default parameters and initial guesses for the dependent variables (n, p, and V), and calculates the generation profile for the active layer. The majority of the default simulation parameters are defined in the class header file, but may be altered after instantiation by using the "Device Manipulation" set of class functions.

E.2 Performing 2-D Simulations and Mapping Morphological Data with `ImportMorphology()`

As mentioned above, passing a second input parameter to the constructor creates a 2-D device with the dimensions specified by the constructor parameters. At this point, the device is still uniform and will produce the same simulation results as a 1-D device. To account for morphological effects, you must provide morphological data and import it into the simulation. The most straightforward way to do this is by using the `ImportMorphology(string filename, int numBlurs, double sigma)` function. This function has one mandatory parameter, which is the filename of the data file containing the morphological data. The morphological data must be formatted as a ".csv" file and should specify the compositional morphology of the device at all grid points. As such, all of the values in the input file should be between 0 and 1. The additional parameters, `numBlurs` and `sigma` are used to "mix" the morphology and introduce a mixed-phase between pure regions, as described in Chapter 4 of the main text. The mixing is achieved by performing successive Gaussian smoothing operations. The additional parameters, `numBlurs` and `sigma`, specify the number of Gaussian smoothing operations to be performed and the standard deviation of the Gaussian kernel used for the smoothing.

E.3 The `DDSolve()` function

The `DDSolve()` function, as its name implies, solves the D-D model equations and updates the dependent variables (n, p, and V) for the devices current parameter set. This function should be called anytime changes are made to the device's simulation parameters. As previously mentioned, the semiconductor equations are solved by a finite-difference discretization scheme which transforms the model's partial differential equations into a set of algebraic equations. This set of algebraic equations is solved by L-U factorization, as implemented in the Eigen Linear Algebra Libray. If no input parameters are passed to the function, a

steady-state solution ($\frac{\partial n}{\partial t} = \frac{\partial n}{\partial t} = 0$) to semiconductor equations is found. This type of solution is appropriate for simulating any non-transient OPV measurememt (J–V characteristics, ideality factor determination, etc.). Once a steady-state solution has been found, transient effects may be accounted for by utilizing a different form of `DDSolve()`. Given an initial solution at time t, by passing a timestep value, Δt, to `DDSolve(double dt)`, a new solution to the semiconductor equations is found at time $t + \Delta t$. It is recommended that you perform a steady-state solution (calling `DDSolve()` without a parameter) before calculating a time-dependent calculation. In practice, the time dependent solution is found by use an implicit method rather than an explicit method. With these two functions, a bevy of OPV experimental measurements and techniques may be simulated. The `DDSolve()` function is *not* called by the constructor when the device is instantiated; however, most of the provided simulation functions already call `DDSolve()` when needed.

E.4 Simulation Functions

As soon as the device has been instantiated, you may begin performing simulations of typical OPV measurements by simply calling one of the "Simulation Functions" (See Sec. E.4) in the `main()` program. A short description of some of the more common experimental measurements is given below. See the class header file for a full list of the currently available simulations.

E.4.1 `JVCharacteristic(double Va_start, double Va_end, int printInterval=0)`

This function simulates a simple J–V characteristic measurement for the device by measuring the current through the device at various applied voltages. The voltage is applied by altering the boundary conditions to the Poisson equation. The input parameters for the function determine the range of the voltages measured for the J–V characteristic. After the voltage ramp is complete, the device's figures of merit (J_{SC}, V_{OC}, and FF) and the overall power conversion efficiency of the device are calculated from the J–V characteristic. The

J–V characteristic and the figures of merit are then printed to file ("JVData.dat" and "FiguresOfMerit.dat"). The spatial distributions of the dependent variables (n, p, and V) and the current densities (electron, hole, and total currents) are also printed to file. When calling `JVCharacteristic()`, these data are only printed at the first applied voltage, by default. In order to print them at additional applied voltages, you must specify the print interval during the functional call. For example, the following function call would simulate and measure a J–V curve for our model device between 0 V and 0.8 V and print the dependent variables at every other applied voltage step:

```
mySolarCell.JVCharacteristic(0,0.8,2);
```

By default, this method measures the J–V characteristic under illumination, as we are most typically interest in the photovoltaic performance of our simulated devices. If you wish to measure the J–V curve in the dark, you may either set the generation rate to 0 by calling `SetGeneration(0)` or by setting the exciton dissociation efficiency parameter to 0 by calling `SetGeff(0)` before calling the `JVCharacteristic()` function.

E.4.2 `PhotoCELIV(double A, double pulseStrength, int tdelay)`

This function simulates a photo-CELIV (Photogenerated Charge Extraction by Linearly Increasing Voltage) experiment. Experimentally, this technique is used to directly measure the mobility of free charge carriers as well as to investigate charge carrier recombination kinetics. The technique involves holding a solar cell at or near V_{OC}, generating charge carriers with a light pulse, and then extracting these charges with a voltage ramp that increases the voltage linearly with time. The current is measured during this technique and may be subsequently analyzed to determine the charge carrier mobilities. The input parameters for this function determine the rate of the voltage ramp, the magnitude of the light pulse, and the time delay between the light pulse and the voltage ramp. The duration of the light pulse and the voltage ramp are defined within the body of the function. Changing them requires manual editing of the function definition and recompiling. The durations of the light pulse, the voltage ramp, and the time delay between light pulse and voltage ramp are specified in

units of μs. The simulation prints the total current density and the average charge carrier densities as a function of time to the file "CELIVData.dat" at every time step. The current transient must be analyzed later by the user to determine the carrier mobilities.

As mentioned previously, the photo-CELIV technique is normally performed by initially holding the device at or near its V_{OC}. Since different devices have different V_{OC}'s, the appropriate starting voltage is not known a priori. The user must therefore determine the approximate V_{OC} beforehand by using `JVCharacteristic()` and setting the device to the voltage before calling `PhotoCELIV()`. For example, the following set of function calls sets the device's applied voltage bias to 0.58 V and performs the photo-CELIV measurement with a voltage ramp of 0.1×10^6 V/s, a pulse intensity of 1 Sun, and a time delay of 10 μs.

```
mySolarCell.SetVoltage(0.58);
mySolarCell.PhotoCELIV(0.1e6,1,10);
```

E.4.3 `TransientPhotocurrent(double pulseStrength, int durationLightPulse, int durationTransient)`

This function simulates a transient photocurrent measurement. The technique involves measuring the current transient of the device in response to a light pulse. The input parameters determine strength of the light pulse (measured in Suns), the duration of the light pulse, and the duration of the transient after the light pulse. The current density and the carrier densities are measured at each time step and printed to file ("TPCData.dat") at the end of the simulation.

E.5 Methods for Device Parameter Manipulation

As mentioned previously, as soon as the model device is instantiated, simulations may be performed immediately since the device already possesses a set of default parameters. In order to examine the effects of different device configurations and simulation parameters on device physics, these parameters must be specified/altered before a simulation function

is called. Device parameters which may be altered include the value of the charge carrier mobilities, the device's built-in voltage, the magnitude of the Schottky barriers, the type of recombination mechanisms that occur, etc. For a full list of all available device parameters which may be altered via function calls, see the "DriftDiffusion.h" header file. Some of the most relevant device parameters (and corresponding functions to manipulate them) are listed below.

E.5.1 Applying a Voltage Bias with `SetVoltage(double Vapp)` and `RampVoltage(double dVa)`

By default, the organic solar cell object is instantiated with zero applied bias, such that the voltage drop across the device's active area is simply equal to the built-in voltage, V_{BI}. In order to change the applied bias, call either the `SetVoltage()` or `RampVoltage()` functions. The first function, as its name implies, sets the appplied bias to whatever value is passed as a parameter in the function call. The second function, `RampVoltage()`, increases or decreases the applied voltage by the specified amount. For example, the following set of function calls will set the applied bias to 0.58 V by first setting the voltage to 0.6 and then reducing the applied bias by 0.02 V:

```
mySolarCell.SetVoltage(0.6);
mySolarCell.RampVoltage(-0.02);
```

These functions are called frequently in the `JVCharacteristic()` and the `PhotoCELIV()` simulations and may be used to construct other simulations.

E.5.2 Changing the Charge Carrier Mobilities with `SetElectronMobility()` and `SetHoleMobility()`

Upon device instantiation, the default electron and hole mobilities are set to 1×10^{-8} $\mathrm{m^2\ V^{-1}\ s^{-1}}$. You may change the charge carrier mobilities independently by calling the `SetElectronMobility()` and `SetHoleMobility()` functions. You may set a constant mo-

bility throughout the device by supplying a single value as a parameter (i.e., `mySolarCell.SetElectronMobility(1e-6);`). If you wish to utilize as a non-uniform mobility profile, you may pass a `MatrixXd` as an input parameter. This `MatrixXd` variable should have the same dimensions as the active layer of the device so that the mobility may be assigned at each grid point. This is most helpful when performing 2-D simulations.

E.5.3 Specifying the Charge Carrier Mobilities of Acceptor and Donor materials with `SetMuNMaxMin()` and `SetMuPMaxMin()`

These functions are most important when performing 2-D simulations of BHJ architectures with distinct regions of donor and acceptor molecules. Typical OPV materials are charge carrier selective in terms of their mobility. These functions allow you to set the upper and lower bounds of the charge carrier mobilities for the different conducting materials when compositional morphology is a factor. For example, consider the following set of commands.

```
mySolarCell.SetMuNMaxMin(1e-7,1e-12);
mySolarCell.SetMuPMaxMin(1e-8,1e-10);
```

The first function calls sets the mobility of electrons in the acceptor and donor materials to 1×10^{-7} m^2 V^{-1} s^{-1} and 1×10^{-12} m^2 V^{-1} s^{-1}, respectively, while the second function call sets the mobility of holes in the donor and acceptor materials to 1×10^{-8} m^2 V^{-1} s^{-1} and 1×10^{-10} m^2 V^{-1} s^{-1}, respectively.

E.5.4 Changing the Generation Rate, G, with `SetGeneration()` and `SetGeff()`

Upon device instantiation, the default carrier generation profile is determined by using a transfer matrix formalism to solve Maxwell's equation to determine the absorption profile through the device. You may also specify the generation rate by using `SetGeneration()` in a similar fashion as `SetElectronMobility()`. You may either pass a single value as a input parameter, in which case a uniform generation profile with that value is implemented, or you may specify a non-uniform generation profile by passing a `MatrixXd` as input parameter to

specify the exact value of the generation rate at each grid point.

The generation rate is further determined by the exciton dissociation efficiency. The transfer matrix formalism only determines the absorption profile, which in turn specifies where excitons are generated. Organic photovoltaic devices typically exhibit exciton dissociation efficiency of >90%. Therefore, the exciton dissociation efficiency constant, G_{eff} is set to 1 by default, which implies that every photon absorbed in the device is split with unit efficiency. The efficiency of exciton dissociation may be altered by calling the `SetGeff()` function with a value between 0 and 1. Furthermore, this function may be used to easily "switch off" or "on" the illumination of the device by setting G_{eff} to either 0 or 1, respectively.

E.5.5 Specifying Recombination Mechanism and Recombination Parameters

The recombination mechanism to be used in the simulation may be specified by using the `SetRecombinationMechanism(string recomType)` function. There are two primary mechanisms for recombination that may be chosen and specified in the function call's parameter list: "Langevin" and "SRH". These correspond to band-to-band, bimolecular recombination of free charges and a trap-mediated recombination, also known as Shockley-Read-Hall recombination. There are several parameters which may be specified for each recombination mechanism. "Langevin"-type recombination's only parameter is a reduction factor, η, which determines the efficiency with which free carriers recombine and may be specified with the `SetRecombinationEfficiencyLangevin()` function. Shockley-Read-Hall recombination has several parameters such as the exponential slope of the trap states and the recombination cross sections for electrons and holes. These may be specified with the `SetBandEdge(double edge)` and `SetBetaNP(double BetaN, double BetaP)` functions, respectively.

E.6 Saving Simulation Data with Print Statements

Most of the simulation functions provided in the class definition already print out relevant simulation data upon execution of the main program. In general, simulation results and measurements are printed as tab-delimited files with the ".dat" extension, while spatially

dependent device parameters and variables are printed as comma-separated files with the ".csv" extension. These files may then be analyzed by the user with any available data analysis software. In addition to the automatic simulation data recording, you may also save other pertinent data using one of the supplied print statements. Some of the most commonly used print statements are listed below. Please see the class definition file for a full list of available print statements.

`PrintNPPSI()` : Prints the independent variables n, p, and V to file with the names "Electrons.csv", "Holes.csv", and "Potential.csv"

`PrintCurrents()` : Prints the electron, hole, and total current densities to multiple .csv files. The x and y components of the current density vectors are printed to separate files. For example the y-component of the electron current density is printed to "currentny.csv"

`PrintMobilities()` : Prints the spatially dependent carrier mobility distributions to "ElectronMobility.csv" and "HoleMobility.csv"

`PrintRecombination()` : Prints the device's recombination rate profile throughout the device to "RecombinationProfile.csv"

`PrintMorphology()` : Prints the device's compositional morphology. Although the device's initial morphology is normally specified by the user, if alterations are made to the morphology during the simulation (i.e., mixing of pure phases), this is a useful function for recording the morphology at different degrees of mixing

`FoMPrint()` : Prints the device's figures of merit (J_{SC}, V_{OC}, FF, and power conversion efficiency) to "FiguresOfMerit.dat"

E.7 An Example Simulation Setup

To summarize, performing a drift-diffusion simulation with our software involves instantiating a device in the `main()` program found in "main.cpp", specifying pertinent device

parameters, calling one of the simulation functions, and subsequently calling any extra print statements to save additional simulation data.

An example of a typical device simulation script is given below:

```
int main()
{
        DriftDiffusion OPV(100,300);

        OPV.SetRecombinationMechanism(''SRH'');
        OPV.SetBandEdge(0.020);
        OPV.SetBetaNP(1e-13,1e-13);

        OPV.SetMuNMinMax(7,12);
        OPV.SetMuPMinMax(8,12);

        OPV.ImportMorphology(''Device.csv'');

        OPV.JVCharacteristic(0,0.8);

        OPV.PrintGeneration();
        OPV.PrintRecombination();

        return 0;
}
```

This set of commands first generates a 100×300 nm organic solar cell. The next three lines specify the type of recombination mechanism to be used (SRH). Since this will be a 2-D simulation and we are investigating morphological effects, the next 2 lines specify the mobility of electrons and holes in the donor and acceptor materials. The next line finally

imports the compositional morphology to be simulated (stored in "Device.csv") before finally performing a J–V characteristic measurement of this device between applied biases of 0 and 0.8 V. After this simulation is completed, the last two lines print additional device data to file, specifically the spatially resolved generation and recombination rates.

References

[1] Levelized cost and levelized avoided cost of new generation resources in the annual energy outlook 2015. Technical report, U.S. Energy Information Administration, 2015.

[2] World energy outlook. Technical report, International Energy Agency, 2015.

[3] J. C. Aguirre, C. Arntsen, S. Hernandez, R. Huber, A. M. Nardes, M. Halim, D. Kilbride, Y. Rubin, S. H. Tolbert, N. Kopidakis, B. J. Schwartz, and D. Neuhauser. Understanding local and macroscopic electron mobilities in the fullerene network of conjugated polymer-based solar cells: Time-resolved microwave conductivity and theory. *Adv. Funct. Mater.*, 24(6):784–792, 2014.

[4] J. C. Aguirre, S. A. Hawks, A. S. Ferreira, P. Yee, S. Subramaniyan, S. A. Jenekhe, S. H. Tolbert, and B. J. Schwartz. Sequential processing for organic photovoltaics: Design rules for morphology control by tailored semi-orthogonal solvent blends. *Advanced Energy Materials*, 5(11):1402020, 2015. 1402020.

[5] S. Albrecht, W. Schindler, J. Kurpiers, J. Kniepert, J. C. Blakesley, I. Dumsch, S. Allard, K. Fostiropoulos, U. Scherf, and D. Neher. On the Field Dependence of Free Charge Carrier Generation and Recombination in Blends of PCPDTBT/PC70BM: Influence of Solvent Additives. *J. Phys. Chem. Lett.*, 3(5):640–645, 2012.

[6] T. D. Anthopoulos, D. M. de Leeuw, E. Cantatore, P. van 't Hof, J. Alma, and J. C. Hummelen. Solution processible organic transistors and circuits based on a C-70 methanofullerene. *J. Appl. Phys.*, 98(5), 2005.

[7] A. Armin, G. Juška, B. W. Philippa, P. L. Burn, P. Meredith, R. D. White, and A. Pivrikas. Doping-Induced Screening of the Built-in-Field in Organic Solar Cells: Effect on Charge Transport and Recombination. *Adv. Energy Mater.*, 3(3):321–327, Mar. 2013.

[8] C. Arntsen, R. Reslan, S. Hernandez, Y. Gao, and D. Neuhauser. Direct delocalization for calculating electron transfer in fullerenes. *Int. J. of Quant. Chem.*, 113(15):1885–1889, 2013.

[9] A. L. Ayzner, C. J. Tassone, S. H. Tolbert, and B. J. Schwartz. Reappraising the need for bulk heterojunctions in polymerfullerene photovoltaics: The role of carrier transport in all-solution-processed p3ht/pcbm bilayer solar cells. *J. Phys. Chem. C*, 113(46):20050–20060, 2009.

[10] S. Bange, M. Schubert, and D. Neher. Charge mobility determination by current extraction under linear increasing voltages: Case of nonequilibrium charges and field-dependent mobilities. *Phys. Rev. B*, 81(3):035209, 2010.

[11] J. A. Barker, C. M. Ramsdale, and N. C. Greenham. Modeling the current-voltage characteristics of bilayer polymer photovoltaic devices. *Phys. Rev. B*, 67:075205, 2003.

[12] J. A. Bartelt, Z. M. Beiley, E. T. Hoke, W. R. Mateker, J. D. Douglas, B. A. Collins, J. R. Tumbleston, K. R. Graham, A. Amassian, H. Ade, J. M. J. Frchet, M. F. Toney, and M. D. McGehee. The importance of fullerene percolation in the mixed regions of polymerfullerene bulk heterojunction solar cells. *Adv. Energy Mater.*, 3(3):364–374, 2013.

[13] J. Bisquert. Chemical capacitance of nanostructured semiconductors: its origin and significance for nanocomposite solar cells. *Phys. Chem. Chem. Phys.*, 5(24):5360–5364, 2003.

[14] J. Bisquert and G. Garcia-Belmonte. On Voltage, Photovoltage, and Photocurrent in Bulk Heterojunction Organic Solar Cells. *J. Phys. Chem. Lett.*, 2(15):1950–1964, 2011.

[15] J. C. Blakesley, F. A. Castro, W. Kylberg, G. F. Dibb, C. Arantes, R. Valaski, M. Cremona, J. S. Kim, and J.-S. Kim. Towards reliable charge-mobility benchmark measurements for organic semiconductors. *Org. Electron.*, 15(6):1263–1272, June 2014.

[16] J. C. Blakesley and D. Neher. Relationship between energetic disorder and open-circuit voltage in bulk heterojunction organic solar cells. *Phys. Rev. B*, 84:075210, 2011.

[17] L. Bolikowski and M. Gokieli. Simulating phase transition dynamics on non-trivial domains. In R. Wyrzykowski, J. Dongarra, K. Karczewski, and J. Waniewski, editors, *Parallel Processing and Applied Mathematics*, pages 510–519. Springer, Berlin Heidelberg, 2014. MATLAB Code: urlhttps://github.com/bolo1729/cahn-hilliard.

[18] C. J. Brabec, S. Gowrisanker, J. J. M. Halls, D. Laird, S. Jia, and S. P. Williams. Polymer-Fullerene Bulk-Heterojunction Solar Cells. *Adv. Mater.*, 22(34):3839–3856, 2010.

[19] C. J. Brabec, M. Heeney, I. McCulloch, and J. Nelson. Influence of blend microstructure on bulk heterojunction organic photovoltaic performance. *Chem. Soc. Rev.*, 40(3):1185–1199, 2011.

[20] A. Bruno, L. X. Reynolds, C. Dyer-Smith, J. Nelson, and S. A. Haque. Determining the exciton diffusion length in a polyfluorene from ultrafast fluorescence measurements of polymer/fullerene blend films. *J. Phys. Chem. C.*, 117(39):19832–19838, 2013.

[21] E. Buchaca-Domingo, A. J. Ferguson, F. C. Jamieson, T. McCarthy-Ward, S. Shoaee, J. R. Tumbleston, O. G. Reid, L. Yu, M.-B. Madec, M. Pfannmoller, F. Hermerschmidt, R. R. Schroder, S. E. Watkins, N. Kopidakis, G. Portale, A. Amassian, M. Heeney, H. Ade, G. Rumbles, J. R. Durrant, and N. Stingelin. Additive-assisted supramolecular manipulation of polymer:fullerene blend phase morphologies and its influence on photophysical processes. *Mater. Horiz.*, 1:270–279, 2014.

[22] T. M. Burke, S. Sweetnam, K. Vandewal, and M. D. McGehee. Beyond langevin recombination: How equilibrium between free carriers and charge transfer states determines the open-circuit voltage of organic solar cells. *Adv. Energy Mater.*, 5(11):1500123, 2015.

[23] G. F. Burkhard, E. T. Hoke, and M. D. McGehee. Accounting for interference, scattering, and electrode absorption to make accurate internal quantum efficiency measurements in organic and other thin solar cells. *Adv. Mater.*, 22(30):3293–3297, Aug. 2010.

[24] G. A. Buxton and N. Clarke. Predicting structure and property relations in polymeric photovoltaic devices. *Physical Review B*, 74(8):085207, 2006.

[25] J. A. Carr and S. Chaudhary. The identification, characterization and mitigation of defect states in organic photovoltaic devices: a review and outlook. *Energy Environ. Sci.*, 6(12):3414, 2013.

[26] A. Cheknane, H. S. Hilal, F. Djeffal, B. Benyoucef, and J.-P. Charles. An equivalent circuit approach to organic solar cell modelling. *Microelectronic. J.*, 39(10):1173–1180, 2008.

[27] J.-D. Chen, C. Cui, Y.-Q. Li, L. Zhou, Q.-D. Ou, C. Li, Y. Li, and J.-X. Tang. Single-junction polymer solar cells exceeding 10efficiency. *Adv. Mater.*, 27(6):1035–1041, 2015.

[28] W. Chen, M. P. Nikiforov, and S. B. Darling. Morphology characterization in organic and hybrid solar cells. *Energy Environ. Sci.*, 5(8):8045, 2012.

[29] S. A. Choulis, J. Nelson, Y. Kim, D. Poplavskyy, T. Kreouzis, J. R. Durrant, and D. D. C. Bradley. Investigation of transport properties in polymer/fullerene blends using time-of-flight photocurrent measurements. *Appl. Phys. Lett.*, 83(18):3812, 2003.

[30] N. Christ, S. W. Kettlitz, S. Züfle, S. Valouch, and U. Lemmer. Nanosecond response of organic solar cells and photodiodes: role of trap states. *Phys. Rev. B*, 83:195211, 2011.

[31] S. R. Cowan, W. L. Leong, N. Banerji, G. Dennler, and A. J. Heeger. Identifying a Threshold Impurity Level for Organic Solar Cells: Enhanced First-Order Recombination Via Well-Defined PC84BM Traps in Organic Bulk Heterojunction Solar Cells. *Adv. Funct. Mater.*, 21(16):3083–3092, Aug. 2011.

[32] S. R. Cowan, A. Roy, and A. J. Heeger. Recombination in polymer-fullerene bulk heterojunction solar cells. *Phys. Rev. B*, 82:245207, Dec 2010.

[33] S. R. Cowan, R. A. Street, C. Shinuk, and A. J. Heeger. Transient photoconductivity in polymer bulk heterojunction solar cells: Competition between sweep-out and recombination. *Phys. Rev. B*, 83:035205, 2011.

[34] D. Credgington and J. R. Durrant. Insights from Transient Optoelectronic Analyses on the Open-Circuit Voltage of Organic Solar Cells. *J. Phys. Chem. Lett.*, 3(11):1465–1478, June 2012.

[35] D. Credgington, R. Hamilton, P. Atienzar, J. Nelson, and J. R. Durrant. Non-Geminate Recombination as the Primary Determinant of Open-Circuit Voltage in Polythiophene:Fullerene Blend Solar Cells: an Analysis of the Influence of Device Processing Conditions. *Adv. Funct. Mater.*, 21(14):2744–2753, 2011.

[36] D. Credgington, F. C. Jamieson, B. Walker, T.-Q. Nguyen, and J. R. Durrant. Quantification of Geminate and Non-Geminate Recombination Losses within a Solution-Processed Small-Molecule Bulk Heterojunction Solar Cell. *Adv. Mater.*, 24(16):2135–2141, 2012.

[37] D. Credgington and Y. Kim. Analysis of recombination losses in a pentacene/C60 organic bilayer solar cell. *J. Phys. Chem. Lett.*, 2:2759–2763, 2011.

[38] B. T. de Villers, C. J. Tassone, S. H. Tolbert, and B. J. Schwartz. Improving the reproducibility of P3HT:PCBM solar cells by controlling the pcbm/cathode interface. *J. Phys. Chem. C*, 113(44):18978–18982, 2009.

[39] C. Deibel, A. Baumann, A. Wagenpfahl, and V. Dyakonov. Polaron recombination in pristine and annealed bulk heterojunction solar cells. *Synth. Met.*, 159(21-22):2345–2347, 2009.

[40] C. Deibel and V. Dyakonov. Polymer-fullerene bulk heterojunction solar cells. *Reports Prog. Phys.*, 73:096401, 2010.

[41] C. Deibel and A. Wagenpfahl. Comment on Interface state recombination in organic solar cells. *Phys. Rev. B*, 82(20):207301, Nov. 2010.

[42] C. Deibel, A. Wagenpfahl, and V. Dyakonov. Origin of reduced polaron recombination in organic semiconductor devices. *Phys. Rev. B*, 80:075203, 2009.

[43] F. Deledalle, P. Shakya Tuladhar, J. Nelson, J. R. Durrant, and T. Kirchartz. Understanding the Apparent Charge Density Dependence of Mobility and Lifetime in Organic Bulk Heterojunction Solar Cells. *J. Phys. Chem. C*, 118(17):8837–8842, May 2014.

[44] G. Dennler, M. C. Scharber, and C. J. Brabec. Polymer-Fullerene Bulk-Heterojunction Solar Cells. *Adv. Mater.*, 21(13):1323–1338, 2009.

[45] D. Di Nuzzo, S. van Reenen, R. a. J. Janssen, M. Kemerink, and S. Meskers. Evidence for space-charge-limited conduction in organic photovoltaic cells at open-circuit conditions. *Phys. Rev. B*, 87(8):085207, Feb. 2013.

[46] G. F. A. Dibb, F. C. Jamieson, A. Maurano, J. Nelson, and J. R. Durrant. Limits on the Fill Factor in Organic Photovoltaics: Distinguishing Nongeminate and Geminate Recombination Mechanisms. *J. Phys. Chem. Lett.*, 4(5):803–808, 2013.

[47] G. F. A. Dibb, T. Kirchartz, D. Credgington, J. R. Durrant, and J. Nelson. Analysis of the Relationship between Linearity of Corrected Photocurrent and the Order of Recombination in Organic Solar Cells. *J. Phys. Chem. Lett.*, 2(19):2407–2411, 2011.

[48] S. Dongaonkar, J. D. Servaites, G. M. Ford, S. Loser, J. Moore, R. M. Gelfand, H. Mohseni, H. W. Hillhouse, R. Agrawal, M. a. Ratner, T. J. Marks, M. S. Lundstrom, and M. A. Alam. Universality of non-Ohmic shunt leakage in thin-film solar cells. *J. Appl. Phys.*, 108(12):124509, 2010.

[49] M. P. Eng, P. R. F. Barnes, and J. R. Durrant. Concentration-Dependent Hole Mobility and Recombination Coefficient in Bulk Heterojunctions Determined from Transient Absorption Spectroscopy. *J. Phys. Chem. Lett.*, 1(20):3096–3100, 2010.

[50] D. J. Eyre. An unconditionally stable one-step scheme for gradient systems. *Unpublished manuscript*, 1998. Available online from: http://www.math.utah.edu/eyre/research/methods/stable.ps MATLAB Code: http://www.math.utah.edu/~eyre/computing/matlab-intro/ch.txt.

[51] B. Y. Finck and B. J. Schwartz. Understanding the origin of the s-curve in conjugated polymer/fullerene photovoltaics from drift-diffusion simulations. *Appl. Phys. Lett.*, 103:053306, 2013.

[52] B. Y. Finck and B. J. Schwartz. Drift-diffusion modeling of the effects of structural disorder and carrier mobility on the performance of organic photovoltaic devices. *Phys. Rev. Appl.*, 4:034006, 2015.

[53] M. Glatthaar, M. Riede, N. Keegan, K. Sylvester-Hvid, B. Zimmermann, M. Niggemann, A. Hinsch, and A. Gombert. Efficiency limiting factors of organic bulk heterojunction solar cells identified by electrical impedance spectroscopy. *Sol. Energ. Mat. Sol. Cells*, 91(5):390–393, 2007.

[54] D. J. Griffiths. *Introduction to Electrodynamics*. Pearson, 3 edition, 1999.

[55] D. J. Griffiths. *Introduction to Electrodynamics*. Pearson, 3 edition, 1999.

[56] D. J. Griffiths. *Introduction to Electrodynamics*. Pearson, 3 edition, 1999.

[57] G. Guennebaud, B. Jacob, et al. Eigen v3. http://eigen.tuxfamily.org, 2010.

[58] H. K. Gummel. Self-consistent iterative scheme for 1-dimensional steady state transistor calculations. *IEEE Trans. Electron Dev.*, 11(10):455, 1964.

[59] S. Günes, H. Neugebauer, and N. S. Sariciftci. Conjugated polymer-based organic solar cells. *Chem. Rev.*, 107(4):1324–1338, 2007.

[60] J. Guo, H. Ohkita, H. Benten, and S. Ito. Charge generation and recombination dynamics in poly(3-hexylthiophene)/fullerene blend films with different regioregularities and morphologies. *J. Am. Chem. Soc.*, 132(17):6154–6164, 2010.

[61] D. Gupta, M. Bag, and K. S. Narayan. Correlating reduced fill factor in polymer solar cells to contact effects. *Appl. Phys. Lett.*, 92(9):093301, 2008.

[62] R. Häeusermann, E. Knapp, M. Moos, N. A. Reinke, and B. Ruhstaller. Coupled optoelectronic simulation of organic bulk-heterojunction solar cells: Parameter extraction and sensitivity analysis. *J. Appl. Phys.*, 106(10):104507, 2009.

[63] R. N. Hall. Electron-hole recombination in germanium. *Phys. Rev.*, 87:387, 1952.

[64] R. Hamilton, C. G. Shuttle, B. O'Regan, T. C. Hammant, J. Nelson, and J. R. Durrant. Recombination in Annealed and Nonannealed Polythiophene/Fullerene Solar Cells: Transient Photovoltage Studies versus Numerical Modeling. *J. Phys. Chem. Lett.*, 1(9):1432–1436, 2010.

[65] R. Hanfland, M. A. Fischer, W. Brutting, U. Wurfel, and R. C. I. MacKenzie. The physical meaning of charge extraction by linearly increasing voltage transients from organic solar cells. *Appl. Phys. Lett.*, 103(6):063904, 2013.

[66] S. A. Hawks, J. C. Aguirre, L. T. Schelhas, R. J. Thompson, R. C. Huber, A. S. Ferreira, G. Zhang, A. A. Herzing, S. H. Tolbert, and B. J. Schwartz. Comparing matched polymer:fullerene solar cells made by solution-sequential processing and traditional blend casting: Nanoscale structure and device performance. *J. Phys. Chem. C*, 118(31):17413–17425, 2014.

[67] S. A. Hawks, F. Deledalle, J. Yao, D. G. Rebois, G. Li, J. Nelson, Y. Yang, T. Kirchartz, and J. R. Durrant. Relating Recombination, Density of States, and Device Performance in an Efficient Polymer:Fullerene Organic Solar Cell Blend. *Adv. Energy Mater.*, 3(9):1201–1209, Sept. 2013.

[68] S. A. Hawks, B. Y. Finck, and B. J. Schwartz. Theory of current transients in planar semiconductor devices: Insights and applications to organic solar cells. *Phys. Rev. Appl.*, 3(4):044014, 2015.

[69] S. A. Hawks, G. Li, Y. Yang, and R. A. Street. Band tail recombination in polymer:fullerene organic solar cells. *J. Appl. Phys.*, 116:074503, 2014.

[70] Z. He, B. Xiao, F. Liu, H. Wu, Y. Yang, S. Xiao, C. Wang, T. P. Russell, and Y. Cao. Single-junction polymer solar cells with high efficiency and photovoltage. *Nature Photon.*, 9(3):174–179, 2015.

[71] C. V. Hoven, X.-D. Dang, R. C. Coffin, J. Peet, T.-Q. Nguyen, and G. C. Bazan. Improved performance of polymer bulk heterojunction solar cells through the reduction of phase separation via solvent additives. *Adv. Mater.*, 22(8), 2010.

[72] B. Huang, J. A. Amonoo, A. Li, X. C. Chen, and P. F. Green. Role of domain size and phase purity on charge carrier density, mobility, and recombination in poly(3-hexylthiophene):phenyl-c61-butyric acid methyl ester devices. *J. Phys. Chem. C*, 118(8):3968–3975, 2014.

[73] Y. Huang, E. J. Kramer, A. J. Heeger, and G. C. Bazan. Bulk heterojunction solar cells: Morphology and performance relationships. *Chem. Rev.*, 114(14):7006–7043, 2014.

[74] I. Hwang and N. C. Greenham. Modeling photocurrent transients in organic solar cells. *Nanotechnology*, 19(42):424012, 2008.

[75] I. Hwang, C. R. McNeill, and N. C. Greenham. Drift-diffusion modeling of photocurrent transients in bulk heterojunction solar cells. *J. Appl. Phys.*, 106(9):094506, 2009.

[76] Janine, Fischer, J. Widmer, H. Kleeman, W. Tress, C. Koerner, M. Riede, K. Vandewal, and K. Leo. A charge carrier transport model for donor-acceptor blend layers. *J. Appl. Phys.*, 117:045501, 2015.

[77] G. Juška, K. Arlauskas, R. Österbacka, and H. Stubb. Time-of-flight measurements in thin films of regioregular poly(3-hexyl thiophene). *Synth. Met.*, 109:173–176, 2000.

[78] G. Juška, K. Arlauskas, M. Viliunas, and J. Kocka. Extraction current transients: new method of study of charge transport in microcrystalline silicon. *Phys. Rev. Lett.*, 84(21):4946–9, May 2000.

[79] G. Juška, N. Nekrašas, K. Genevičius, J. Stuchlik, and J. Kočka. Relaxation of photoexited charge carrier concentration and mobility in μc-Si:H. *Thin Solid Films*, 451-452:290–293, Mar. 2004.

[80] G. Juška, N. Nekrašas, V. Valentinavičius, P. Meredith, and A. Pivrikas. Extraction of photogenerated charge carriers by linearly increasing voltage in the case of Langevin recombination. *Phys. Rev. B*, 84(15):155202, Oct. 2011.

[81] K. Kawano, J. Sakai, M. Yahiro, and C. Adachi. Effect of solvent on fabrication of active layers in organic solar cells based on poly(3-hexylthiophene) and fullerene derivatives. *Sol. Energy Mater. Sol. Cells*, 93(4):514–518, Apr. 2009.

[82] S. W. Kettlitz, J. Mescher, N. S. Christ, M. Nintz, S. Valouch, A. Colsmann, and U. Lemmer. Eliminating RC-Effects in Transient Photocurrent Measurements on Organic Photodiodes. *IEEE Photon. Tech. Lett.*, 25(7):682–685, 2013.

[83] Y. Kim, S. A. Choulis, J. Nelson, D. D. C. Bradley, S. Cook, and J. R. Durrant. Device annealing effect in organic solar cells with blends of regioregular poly(3-hexylthiophene) and soluble fullerene. *Appl. Phys. Lett.*, 86(6):063502, 2005.

[84] T. Kirchartz, T. Agostinelli, M. Campoy-Quiles, W. Gong, and J. Nelson. Understanding the Thickness-Dependent Performance of Organic Bulk Heterojunction Solar Cells: The Influence of Mobility, Lifetime, and Space Charge. *J. Phys. Chem. Lett.*, 3(23):3470–3475, 2012.

[85] T. Kirchartz, F. Deledalle, P. S. Tuladhar, J. R. Durrant, and J. Nelson. On the differences between dark and light ideality factor in polymer:Fullerene solar cells. *J. Phys. Chem. Lett.*, 4:2371–2376, 2013.

[86] T. Kirchartz and J. Nelson. Meaning of reaction orders in polymer:fullerene solar cells. *Phys. Rev. B*, 86(16):165201, 2012.

[87] T. Kirchartz, B. E. Pieters, J. Kirkpatrick, U. Rau, and J. Nelson. Recombination via tail states in polythiophene:fullerene solar cells. *Phys. Rev. B*, 83:115209, 2011.

[88] T. Kirchartz, B. E. Pieters, K. Taretto, and U. Rau. Mobility dependent efficiencies of organic bulk heterojunction solar cells: Surface recombination and charge transfer state distribution. *Phys. Rev. B*, 80(3):6, July 2009.

[89] R. J. Kline, M. D. McGehee, E. N. Kadnikova, J. Liu, and J. M. J. Frechet. Controlling the field-effect mobility of regioregular polythiophene by changing the molecular weight. *Adv. Mater.*, 15(18):1519, 2003.

[90] E. Knapp, R. Häeusermann, H. U. Schwarzenbach, and B. Ruhstaller. Numerical simulation of charge transport in disordered organic semiconductor devices. *J. Appl. Phys.*, 108(5):054504, 2010.

[91] J. Kniepert, I. Lange, N. J. van der Kaap, L. J. A. Koster, and D. Neher. A conclusive view on charge generation, recombination, and extraction in as-prepared and annealed P3HT:PCBM blends: Combined experimental and simulation work. *Adv. Energy Mater.*, 4(7):1301401, 2014.

[92] H. K. Kodali and B. Ganapathysubramanian. A computational framework to investigate charge transport in heterogeneous organic photovoltaic devices. *Computer Methods in Applied Mechanics and Engineering*, 247:113–129, 2012.

[93] L. J. A. Koster, V. D. Mihailetchi, and P. W. M. Blom. Bimolecular recombination in polymer/fullerene bulk heterojunction solar cells. *Appl. Phys. Lett.*, 88(5):052104, 2006.

[94] L. J. A. Koster, E. C. P. Smits, V. D. Mihailetchi, and P. W. M. Blom. Device model for the operation of polymer/fullerene bulk heterojunction solar cells. *Phys. Rev. B*, 72(8):085205, 2005.

[95] F. C. Krebs, N. Espinosa, M. Hösel, R. R. Søndergaard, and M. Jørgensen. 25th anniversary article: Rise to power opv-based solar parks. *Adv. Mater.*, 26(1):29–39, 2014.

[96] G. Lakhwani, A. Rao, and R. H. Friend. Bimolecular recombination in organic photovoltaics. *Annu. Rev. Phys. Chem.*, 65(1):557–581, 2014.

[97] Y.-K. Lan and C.-I. Huang. A theoretical study of the charge transfer behavior of the highly regioregular poly-3-hexylthiophene in the ordered state. *J. Phys. Chem. B*, 112(47):14857–14862, 2008.

[98] F. Laquai, D. Andrienko, R. Mauer, and P. W. M. Blom. Charge carrier transport and photogeneration in p3ht:pcbm photovoltaic blends. *Macromol. Rapid Commun.*, 36(11):1001–1025, 2015.

[99] M. M. Lee, J. Teuscher, T. Miyasaka, T. N. Murakami, and H. J. Snaith. Efficient hybrid solar cells based on meso-superstructured organometal halide perovskites. *Science*, 338:643–647, Nov. 2012.

[100] D. Leman, M. A. Kelly, S. Ness, S. Engmann, A. Herzing, C. Snyder, H. W. Ro, R. J. Kline, D. M. DeLongchamp, and L. J. Richter. In situ characterization of polymer-fullerene bilayer stability. *Macromolecules*, 48(2):383–392, 2015.

[101] G. Li, Y. Yao, H. Yang, V. Shrotriya, G. Yang, and Y. Yang. "solvent annealing effect in polymer solar cells based on poly(3-hexylthiophene) and methanofullerenes. *Adv. Func. Mater.*, 17(10):1636–1644, 2007.

[102] Z. Li, G. Lakhwani, N. C. Greenham, and C. R. McNeill. Voltage-dependent photocurrent transients of PTB7:PC70BM solar cells: Experiment and numerical simulation. *J. Appl. Phys.*, 114:034502, 2013.

[103] M. Liedtke, A. Sperlich, H. Kraus, A. Baumann, C. Deibel, M. J. Wirix, J. Loos, C. M. Cardona, and V. Dyakonov. Triplet exciton generation in bulk-heterojunction solar cells based on endohedral fullerenes. *Journal of the American Chemical Society*, 133(23):9088–9094, 2011.

[104] M. Liu, M. B. Johnston, and H. J. Snaith. Efficient planar heterojunction perovskite solar cells by vapour deposition. *Nature*, 501(7467):395–8, Sept. 2013.

[105] S. Lizin, S. Van Passel, E. De Schepper, W. Maes, L. Lutsen, J. Manca, and D. Vanderzande. Life cycle analyses of organic photovoltaics: a review. *Energy Environ. Sci.*, 6(11):3136–3149, 2013.

[106] J. Lorrmann, B. H. Badada, O. Inganas, V. Dyakonov, and C. Deibel. Charge carrier extraction by linearly increasing voltage: Analytic framework and ambipolar transients. *J. Appl. Phys.*, 108(11):113705, 2010.

[107] S. J. Lou, J. M. Szarko, T. Xu, L. Yu, T. J. Marks, and L. X. Chen. Effects of additives on the morphology of solution phase aggregates formed by active layer components of high-efficiency organic solar cells. *J. Am. Chem. Soc.*, 133(51):20661–20663, 2011.

[108] B. P. Lyons, N. Clark, and C. Groves. The relative importance of domain size, domain purity and domain interfaces to the performance of bulk-heterojunction organic photovoltaics. *Energy Environ. Sci.*, 5:7657, 2012.

[109] R. C. I. MacKenzie, C. G. Shuttle, M. L. Chabinyc, and J. Nelson. Extracting microscopic device parameters from transient photocurrent measurements of P3HT:PCBM solar cells. *Adv. Energy Mater.*, 2(6):662–669, 2012.

[110] M. Mas-Torrent, D. den Boer, M. Durkut, P. Hadley, and A. P. H. J. Schenning. Field effect transistors based on poly(3-hexylthiophene) at different length scales. *Nanotechnology*, 15(4):S265–S269, 2004.

[111] A. Maurano, R. Hamilton, C. G. Shuttle, A. M. Ballantyne, J. Nelson, B. O'Regan, W. M. Zhang, I. McCulloch, H. Azimi, M. Morana, C. J. Brabec, and J. R. Durrant. Recombination Dynamics as a Key Determinant of Open Circuit Voltage in Organic Bulk Heterojunction Solar Cells: A Comparison of Four Different Donor Polymers. *Adv. Mater.*, 22(44):4987–4992, 2010.

[112] A. Maurano, C. G. Shuttle, R. Hamilton, A. M. Ballantyne, J. Nelson, W. Zhang, M. Heeney, and J. R. Durrant. Transient Optoelectronic Analysis of Charge Carrier Losses in a Selenophene/Fullerene Blend Solar Cell. *J. Phys. Chem. C*, 115(13):5947–5957, 2011.

[113] A. Mei, X. Li, L. Liu, Z. Ku, T. Liu, Y. Rong, M. Xu, M. Hu, J. Chen, Y. Yang, M. Gratzel, and H. Han. A hole-conductor-free, fully printable mesoscopic perovskite solar cell with high stability. *Science*, 345:295–298, July 2014.

[114] C. Melzer, E. J. Koop, V. D. Mihailetchi, and P. W. Blom. Hole transport in poly (phenylene vinylene)/methanofullerene bulk-heterojunction solar cells. *Adv. Func. Mater.*, 14(9):865–870, 2004.

[115] O. V. Mikhnenko, H. Azimi, M. Scharber, M. Morana, P. W. M. Blom, and M. A. Loi. Exciton diffusion length in narrow bandgap polymers. *Energy Environ. Sci.*, 5(5):6960–6965, 2012.

[116] F. Monestier, J.-J. Simon, P. Torchio, L. Escoubas, F. Flory, S. Bailly, R. de Bettignies, S. Guillerez, and C. Defranoux. Modeling the short-circuit current density of polymer solar cells based on p3ht:pcbm blend. *Sol. Energ. Mat. Sol. Cells*, 91(5):405–410, 2007.

[117] J. S. Moon, J. K. Lee, S. Cho, J. Byun, and A. J. Heeger. "Columnlike" structure of the cross-sectional morphology of bulk heterojunction materials. *Nano Lett.*, 9(1):230–234, 2009.

[118] I. Mora-Seró, J. Bisquert, F. Fabregat-Santiago, G. Garcia-Belmonte, G. Zoppi, K. Durose, Y. Proskuryakov, I. Oja, A. Belaidi, T. Dittrich, R. Tena-Zaera, A. Katty, C. Lévy-Clément, V. Barrioz, and S. J. C. Irvine. Implications of the negative capacitance observed at forward bias in nanocomposite and polycrystalline solar cells. *Nano Lett.*, 6(4):640–50, Apr. 2006.

[119] A. J. Morfa, A. M. Nardes, S. E. Shaheen, N. Kopidakis, and J. van de Lagemaat. Time-of-Flight Studies of Electron-Collection Kinetics in Polymer:Fullerene Bulk-Heterojunction Solar Cells. *Adv. Funct. Mater.*, 21(13):2580–2586, July 2011.

[120] A. Mozer, G. Dennler, N. Sariciftci, M. Westerling, A. Pivrikas, R. Österbacka, and G. Juška. Time-dependent mobility and recombination of the photoinduced charge carriers in conjugated polymer/fullerene bulk heterojunction solar cells. *Phys. Rev. B*, 72(3):035217, July 2005.

[121] A. J. Mozer, N. S. Sariciftci, L. Lutsen, D. Vanderzande, R. Osterbacka, M. Westerling, and G. Juska. Charge transport and recombination in bulk heterojunction solar cells studied by the photoinduced charge extraction in linearly increasing voltage technique. *Appl. Phys. Lett.*, 86(11):112104, 2005.

[122] Y. M. Nam, J. Huh, and W. H. Jo. Optimization of thickness and morphology of active layer for high performance of bulk-heterojunction organic solar cells. *Sol. Energ. Mat. Sol. Cells*, 94(6):1118 – 1124, 2010.

[123] N. Nekrašas, K. Genevičius, M. Vilinas, and G. Juška. Features of current transients of photogenerated charge carriers, extracted by linearly increased voltage. *Chem. Phys.*, 404:56–59, Aug. 2012.

[124] J. Nelson. Polymer: fullerene bulk heterojunction solar cells. *Mater. Today*, 14(10):462–470, Oct. 2011.

[125] S. Neugebauer, J. Rauh, C. Deibel, and V. Dyakonov. Investigation of electronic trap states in organic photovoltaic materials by current-based deep level transient spectroscopy. *Appl. Phys. Lett.*, 100(26):263304, 2012.

[126] M. T. Neukom, N. A. Reinke, K. A. Brossi, and B. Ruhstaller. Transient Photocurrent Response of Organic Bulk Heterojunction Solar Cells. *Proc. SPIE - Int. Soc. Opt. Eng.*, 7722:77220V, Apr. 2010.

[127] M. T. Neukom, S. Züfle, and B. Ruhstaller. Reliable extraction of organic solar cell parameters by combining steady-state and transient techniques. *Org. Electron.*, 13(12):2910 – 2916, 2012.

[128] T.-Q. Nguyen, J. Wu, V. Doan, B. J. Schwartz, and S. H. Tolbert. Control of energy transfer in oriented conjugated polymer-mesoporous silica composites. *Science*, 288(5466):652–656, 2000.

[129] S. D. Oosterhout, M. M. Wienk, S. S. van Bavel, R. Thiedmann, L. J. A. Koster, J. Gilot, J. Loos, V. Schmidt, and R. a. J. Janssen. The effect of three-dimensional morphology on the efficiency of hybrid polymer solar cells. *Nat. Mater.*, 8(10):818–824, 2009.

[130] B. C. O'Regan, J. R. Durrant, P. M. Sommeling, and N. J. Bakker. Influence of the TiCl4 Treatment on Nanocrystalline TiO2 Films in Dye-Sensitized Solar Cells. 2. Charge Density, Band Edge Shifts, and Quantification of Recombination Losses at Short Circuit. *J. Phys. Chem. C*, 111(37):14001–14010, 2007.

[131] B. C. O'Regan and F. Lenzmann. Charge Transport and Recombination in a Nanoscale Interpenetrating Network of n-Type and p-Type Semiconductors: Transient Photocurrent and Photovoltage Studies of TiO2/Dye/CuSCN Photovoltaic Cells. *J. Phys. Chem. B*, 108(14):4342–4350, 2004.

[132] B. C. O'Regan, S. Scully, A. C. Mayer, E. Palomares, and J. Durrant. The Effect of Al2O3 Barrier Layers in TiO2/Dye/CuSCN Photovoltaic Cells Explored by Recombination and DOS Characterization Using Transient Photovoltage Measurements. *J. Phys. Chem. B*, 109(10):4616–4623, 2005.

[133] S. H. Park, A. Roy, S. Beaupre, S. Cho, N. Coates, J. S. Moon, D. Moses, M. Leclerc, K. Lee, and A. J. Heeger. Bulk heterojunction solar cells with internal quantum efficiency approaching 100%. *Nature Photon.*, 3(5):297–302, 2009.

[134] A. Petersen, T. Kirchartz, and T. A. Wagner. Charge extraction and photocurrent in organic bulk heterojunction solar cells. *Phys. Rev. B*, 85:045208, 2012.

[135] L. A. A. Pettersson, L. S. Roman, and O. Inganäs. Modeling photocurrent action spectra of photovoltaic devices based on organic thin films. *J. Appl. Phys.*, 86(1):487–496, 1999.

[136] A. Pivrikas, N. S. Sariciftci, G. Juška, and R. Österbacka. A review of charge transport and recombination in polymer/fullerene organic solar cells. *Prog. Photovolt: Res. Appl.*, 15(8):677–696, 2007.

[137] C. M. Proctor, M. Kuik, and T.-Q. Nguyen. Charge carrier recombination in organic solar cells. *Prog. Polym. Sci.*, 38(12):1941 – 1960, 2013.

[138] C. M. Proctor and T.-Q. Nguyen. Effect of leakage current and shunt resistance on the light intensity dependence of organic solar cells. *Applied Physics Letters*, 106(8):083301, 2015.

[139] R. Qiao, A. P. Roberts, A. S. Mount, S. J. Klaine, and P. C. Ke. Translocation of C-60 and its derivatives across a lipid bilayer. *Nano Lett.*, 7(3):614–619, 2007.

[140] B. Ray and M. A. Alam. Random vs regularized opv: Limits of performance gain of organic bulk heterojunction solar cells by morphology engineering. *Sol. Energ. Mat. Sol. Cells*, 99:204 – 212, 2012.

[141] B. Ray, P. R. Nair, and M. A. Alam. Annealing dependent performance of organic bulk-heterojunction solar cells: A theoretical perspective. *Sol. Energ. Mat. Sol. Cells*, 95(12):3287–3294, 2011.

[142] W. Regan, S. Byrnes, W. Gannett, O. Ergen, O. Vazquez-Mena, F. Wang, and A. Zettl. Screening-Engineered Field-Effect Solar Cells. *Nano Lett.*, 12:4300–4304, 2012.

[143] O. J. Sandberg, M. Nyman, and R. Österbacka. Direct determination of doping concentration and built-in voltage from extraction current transients. *Org. Electron.*, 15:3413–3420, Sept. 2014.

[144] O. J. Sandberg, M. Nyman, and R. Österbacka. Effect of Contacts in Organic Bulk Heterojunction Solar Cells. *Phys. Rev. Appl.*, 1(2):024003, Mar. 2014.

[145] J. Schafferhans, C. Deibel, and V. Dyakonov. Electronic Trap States in Methanofullerenes. *Adv. Energy Mater.*, 1(4):655–660, July 2011.

[146] M. C. Scharber, D. Mühlbacher, M. Koppe, P. Denk, C. Waldauf, A. J. Heeger, and C. J. Brabec. Design rules for donors in bulk-heterojunction solar cellstowards 10% energy-conversion efficiency. *Adv. Mater.*, 18(6):789–794, 2006.

[147] D. L. Scharfetter and H. K. Gummel. Large-signal analysis of a silicon read diode oscillator. *IEEE Trans. Electron Dev.*, 16:64–77, 1969.

[148] H. Scher and E. W. E. Montroll. Anomalous transit-time dispersion in amorphous solids. *Phys. Rev. B*, 12(6):2455–2477, Sept. 1975.

[149] B. Schmidt-Hansberg, M. F. Klein, K. Peters, F. Buss, J. Pfeifer, S. Walheim, A. Colsmann, U. Lemmer, P. Scharfer, and W. Schabel. In situ monitoring the drying kinetics of knife coated polymer-fullerene films for organic solar cells. *J. of Appl. Phys.*, 106(12):124501, 2009.

[150] J. Scott and G. G. Malliaras. Charge injection and recombination at the metalorganic interface. *Chem. Phys. Lett.*, 299(2):115 – 119, 1999.

[151] A. Seemann, T. Sauermann, C. Lungenschmied, O. Armbruster, S. Bauer, H.-J. Egelhaaf, and J. Hauch. Reversible and irreversible degradation of organic solar cell performance by oxygen. *Sol. Energy*, 85(6):1238–1249, June 2011.

[152] S. Selberherr. *Analysis and Simulation of Semiconductor Devices*. Springer, 1984.

[153] J. D. Servaites, M. A. Ratner, and T. J. Marks. Organic solar cells: A new look at traditional models. *Energy Environ. Sci.*, 4(11):4410–4422, 2011.

[154] W. Shockley and W. Read Jr. Statistics of the recombinations of holes and electrons. *Phys. Rev.*, 87(46):835–842, 1952.

[155] C. G. Shuttle, R. Hamilton, J. Nelson, B. C. O'Regan, and J. R. Durrant. Measurement of Charge-Density Dependence of Carrier Mobility in an Organic Semiconductor Blend. *Adv. Funct. Mater.*, 20(5):698–702, 2010.

[156] C. G. Shuttle, R. Hamilton, B. C. O'Regan, J. Nelson, and J. R. Durrant. Charge-density-based analysis of the current-voltage response of polythiophene/fullerene photovoltaic devices. *Proc. Natl. Acad. Sci. U. S. A.*, 107(38):16448–16452, Sept. 2010.

[157] C. G. Shuttle, B. O'Regan, A. M. Ballantyne, J. Nelson, D. D. C. Bradley, J. de Mello, and J. R. Durrant. Experimental determination of the rate law for charge carrier decay in a polythiophene: Fullerene solar cell. *Appl. Phys. Lett.*, 92(9):3, 2008.

[158] C. G. Shuttle, B. O'Regan, A. M. Ballantyne, J. Nelson, D. D. C. Bradley, and J. R. Durrant. Bimolecular recombination losses in polythiophene: Fullerene solar cells. *Phys. Rev. B*, 78(11):4, 2008.

[159] C. G. Shuttle., B. O'Regan, A. M. Ballantyne, J. Nelson, D. D. C. Bradley, and J. R. Durrant. Bimolecular recombination losses in polythiophene:fullerene solar cells. *Phys. Rev. B*, 78(11):113201, 2008.

[160] H. Sirringhaus, P. J. Brown, R. H. Friend, M. M. Nielsen, K. Bechgaard, B. M. W. Langeveld-Voss, A. J. H. Spiering, R. A. J. Janssen, E. W. Meijer, P. Herwig, and D. M. de Leeuw. Two-dimensional charge transport in self-organized, high-mobility conjugated polymers. *Nature*, 401(6754):685–688, 1999.

[161] H. Snaith. Perovskites: the emergence of a new era for low-cost, high-efficiency solar cells. *J. Phys. Chem. Lett.*, 4:3623–3630, 2013.

[162] C. M. Snowden. *Semiconductor Device Modeling*. Peter Peregrinus Ltd., 1988.

[163] C. M. Snowden. *Semiconductor Device Modeling*. Springer, 1989.

[164] R. Søndergaard, M. Hösel, D. Angmo, T. T. Larsen-Olsen, and F. C. Krebs. Roll-to-roll fabrication of polymer solar cells. *Mater. Today*, 15(1):36–49, 2012.

[165] R. A. Street. Measurements of depletion layers in hydrogenated amorphous silicon. *Phys. Rev. B*, 27(8):4924–4932, Apr. 1983.

[166] R. A. Street, S. Cowan, and A. J. Heeger. Experimental test for geminate recombination applied to organic solar cells. *Phys. Rev. B*, 82(12):121301(R), Sept. 2009.

[167] R. A. Street, S. A. Hawks, P. P. Khlyabich, G. Li, B. J. Schwartz, B. C. Thompson, and Y. Yang. Electronic Structure and Transition Energies in PolymerFullerene Bulk Heterojunctions. *J. Phys. Chem. C*, 118(38):21873–21883, Sept. 2014.

[168] R. A. Street, K. W. Song, J. E. Northrup, and S. Cowan. Photoconductivity measurements of the electronic structure of organic solar cells. *Phys. Rev. B*, 83(16):165207, 2011.

[169] S. M. Sze and K. K. Ng. *Physics of semiconductor devices*. Wiley-Interscience, Hoboken, N.J., 3rd edition, 2007.

[170] B. J. Tremolet de Villers, R. C. I. MacKenzie, J. J. Jasieniak, N. D. Treat, and M. L. Chabinyc. Linking Vertical Bulk-Heterojunction Composition and Transient Photocurrent Dynamics in Organic Solar Cells with Solution-Processed MoOx Contact Layers. *Adv. Energy Mater.*, 4(5):1301290, Apr. 2014.

[171] W. Tress and O. Inägans. Simple experimental test to distinguish extraction and injection barriers at the electrodes of (organic) solar cells with s-shaped currentvoltage characteristics. *Sol. Energ. Mat. Sol. Cells*, 117(0):599 – 603, 2013.

[172] W. Tress, K. Leo, and M. Riede. Influence of hole-transport layers and donor materials on open-circuit voltage and shape of I-V curves of organic solar cells. *Adv. Funct. Mater.*, 21(11):2140–2149, 2011.

[173] W. Tress, K. Leo, and M. Riede. Optimum mobility, contact properties, and open-circuit voltage of organic solar cells: A drift-diffusion simulation study. *Phys. Rev. B*, 85:155201, 2012.

[174] W. Tress, A. Petrich, M. Hummert, M. Hein, K. Leo, and M. Riede. Imbalanced mobilities causing s-shaped iv curves in planar heterojunction organic solar cells. *Appl. Phys. Lett.*, 98(6):063301, 2011.

[175] W. C. Tsoi, S. J. Spencer, L. Yang, A. M. Ballantyne, P. G. Nicholson, A. Turnbull, A. G. Shard, C. E. Murphy, D. D. C. Bradley, J. Nelson, and J.-S. Kim. Effect of crystallization on the electronic energy levels and thin film morphology of p3ht:pcbm blends. *Macromolecules*, 44(8):2944–2952, 2011.

[176] J. A. Turner. A realizable renewable energy future. *Science*, 285(5428):687–689, 1999.

[177] S. S. van Bavel, E. Sourty, G. de With, and J. Loos. Three-dimensional nanoscale organization of bulk heterojunction polymer solar cells. *Nano Lett.*, 9(2):507–513, 2009.

[178] S. L. M. van Mensfoort, S. I. E. Vulto, R. A. J. Janssen, and R. Coehoorn. Hole transport in polyfluorene-based sandwich-type devices: Quantitative analysis of the role of energetic disorder. *Phys. Rev. B*, 78:085208, 2008.

[179] B. T. D. Villers, C. J. Tassone, S. H. Tolbert, and B. J. Schwartz. Improving the Reproducibility of P3HT:PCBM Solar Cells by Controlling the PCBM/Cathode Interface. *J. Phys. Chem. C*, 113(44):18978–18982, Nov. 2009.

[180] A. Wagenpfahl, D. Rauh, M. Binder, C. Deibel, and V. Dyakonov. S-shaped current-voltage characteristics of organic solar devices. *Phys. Rev. B*, 82:115306, 2010.

[181] T. Walter, R. Herberholz, C. Müller, and H. W. Schock. Determination of defect distributions from admittance measurements and application to Cu (In ,Ga)Se2 based heterojunctions. *J. Appl. Phys.*, 80(8):4411–4420, 1996.

[182] Z. Wang, M. G. Helander, M. T. Greiner, J. Qiu, and Z.-H. Lu. Carrier mobility of organic semiconductors based on current-voltage characteristics. *J. Appl. Phys.*, 107(3):034506, 2010.

[183] P. K. Watkins, A. B. Walker, and G. L. Verschoor. Dynamical monte carlo modelling of organic solar cells: The dependence of internal quantum efficiency on morphology. *Nano Lett.*, 5(9):1814–1818, 2005.

[184] P. Westacott, J. R. Tumbleston, S. Shoaee, S. Fearn, J. H. Bannock, J. B. Gilchrist, S. Heutz, J. deMello, M. Heeney, H. Ade, J. Durrant, D. S. McPhail, and N. Stingelin. On the role of intermixed phases in organic photovoltaic blends. *Energy Environ. Sci.*, 6:2756–2764, 2013.

[185] O. Wodo and B. Ganapathysubramanian. Modeling morphology evolution during solvent-based fabrication of organic solar cells. *Comput. Mater. Sci.*, 55:113–126, 2012.

[186] O. Wodo, J. D. Roehling, A. J. Moule, and B. Ganapathysubramanian. Quantifying organic solar cell morphology: a computational study of three-dimensional maps. *Energy Environ. Sci.*, 6:3060–3070, 2013.

[187] W.-R. Wu, U.-S. Jeng, C.-J. Su, K.-H. Wei, M.-S. Su, M.-Y. Chiu, C.-Y. Chen, W.-B. Su, C.-H. Su, and A.-C. Su. Competition between fullerene aggregation and poly(3-hexylthiophene) crystallization upon annealing of bulk heterojunction solar cells. *ACS Nano*, 5(8):6233–6243, 2011.

[188] W.-R. Wu, U.-S. Jeng, C.-J. Su, K.-H. Wei, M.-S. Su, M.-Y. Chiu, C.-Y. Chen, W.-B. Su, C.-H. Su, and A.-C. Su. Competition between fullerene aggregation and poly(3-hexylthiophene) crystallization upon annealing of bulk heterojunction solar cells. *ACS Nano*, 5(8):6233–6243, 2011.

[189] J. You, L. Dou, K. Yoshimura, T. Kato, K. Ohya, T. Moriarty, K. Emery, C.-C. Chen, J. Gao, G. Li, and Y. Yang. A polymer tandem solar cell with 10.6% power conversion efficiency. *Nat. Commun.*, 4:1446, 2013.

[190] G. Yu, J. Gao, J. C. Hummelen, F. Wudl, and A. J. Heeger. Polymer photovoltiac cells: Enhanced efficiencies via a network of internal donor-acceptor heterojunctions. *Science*, 270(5243):1789, 1995.

[191] G. Yu, C. Zhang, and A. J. Heeger. Dual-function semiconducting polymer devices: Light-emitting and photodetecting diodes. *Appl. Phys. Lett.*, 64(12):1540–1542, 1994.

[192] A. R. b. M. Yusoff, D. Kim, H. P. Kim, F. K. Shneider, W. J. da Silva, and J. Jang. A high efficiency solution processed polymer inverted triple-junction solar cell exhibiting a power conversion efficiency of 11.83%". *Energy Environ. Sci.*, 8:303–316, 2015.

[193] U. Zhokhavets, T. Erb, H. Hoppe, G. Gobsch, and N. S. Sariciftci. Effect of annealing of poly(3-hexylthiophene)/fullerene bulk heterojunction composites on structural and optical properties. *Thin Solid Films*, 496(2):679 – 682, 2006.

[194] H. Zhou, Y. Zhang, C.-K. Mai, S. D. Collins, G. C. Bazan, T.-Q. Nguyen, and A. J. Heeger. Polymer homo-tandem solar cells with best efficiency of 11.3%. *Adv. Mater.*, 27(10):1767–1773, 2015.